Lawrence Berkeley Laboratory
UNIVERSITY OF CALIFORNIA

Materials & Molecular
Research Division

THE CORROSION OF SILICATE MATERIALS BY HYDROGEN GAS AND HYDROFLUORIC ACID SOLUTION

Stephen T. Tso
(Ph. D. thesis)

October 1979

Prepared for the U.S. Department of Energy under Contract W-7405-ENG-48

DISCLAIMER

THE CORROSION OF SILICATE MATERIALS
BY HYDROGEN GAS AND HYDROFLUORIC ACID SOLUTION

Contents

THE CORROSION OF SILICATE MATERIALS BY HYDROGEN GAS AND HYDROFLUORIC ACID SOLUTION

Stephen T. Tso

Materials and Molecular Research Division, Lawrence Berkeley Laboratory
and Department of Materials Science and Mineral Engineering,
University of California, Berkeley, California 94720

ABSTRACT

The reactions of silicate materials with hydrogen gas were studied. The mechanism for the reaction of pure silica glass with hydrogen gas was investigated. Alumino-silicate glasses and calcium alumino silicate glasses were used to reveal the compositional effect on corrosion resistance. Different methods were employed to increase the corrosion resistance. Mullite was found to have potential as a material for coal gassification applications.

The reactions between silicate glasses and hydrofluoric acid solution were also investigated. The difference in reaction rates for different glasses were explained on the basis of phase separation and crystallization. These two reactions (with hydrogen gas and hydrofluoric acid solution) are in strong contrast in several aspects. The latter is diffusion controlled while the former is kinetically controlled. Therefore, no empirical relative corrosion resistance between them was found.

INTRODUCTION

Natural gas has always been an important source of energy for the United States. Thousands of homes and factories are equipped with gas-heating furnaces. The domestic natural gas production rate is already failing to match the demand by an enormous amount. Estimates indicate that domestic production of natural gas will amount to only about one-half of the demand by 1985. Therefore, it is urgent that the process of coal gasification, for producing synthetic natural gas on a large scale from the abundant supplies of coal in the U.S., be developed and utilized as quickly as possible.

Coal gasification equipment must be lined with refractory materials to lower the temperature of the outer metal shell in order to reduce heat loss and prevent metal failure. However, the volatilization of silica and silicates in reducing atmospheres rich in hydrogen, methane, carbon oxides and water vapor presents a special problem to refractories used in the lining and insulation. Because silicates are the most inexpensive refractory material, it is desirable that their corrosion resistance be improved so that they may be used in a reducing atmosphere. Understanding the reaction occurring in the coal gasifier and then finding a method of improving the corrosion resistance of silicates are therefore important research goals. In an attempt to understand mechanisms of refractory failure, the reactions between silica, silicates and hydrogen gas have been studied. This is only a small segment of a more complex problem. It is found that the loss of silicate material in the presence of hydrogen gas is due to the following reaction:

$$H_{2(g)} + SiO_2 \rightarrow H_2O_{(g)} + SiO_{(g)} \qquad (1)$$

A computer aided survey of published papers showed that very little scientific study had been done in this field. Most studies have been engineering-oriented. The reaction mechanism has not been revealed. Neither has there been any systematic effort to increase the corrosion resistance of the material. Realizing that ordinary refractory material was too complex - pores, impurities, etc. - for a quantitative study, pure silica glass and silicate glasses were used as a starting material for this study. Mullite with controlled composition has also been studied as a potential candidate material for the coal gasifier application. The corrosion reactions of pure silica glass and silicate glasses by hydrofluoric acid solution were also investigated in order to reveal the possible empirical reactivity correlation between these two reactions (with hydrogen gas and with hydrofluoric acid solution).

Thermodynamics and kinetics of the reaction (1) are discussed in the following sections. The possible slowest steps were explored. The pressure and temperature dependence, which are important in explaining the empirical data and determining the mechanism for the reaction, are also discussed for each case. The heat transfer mechanism and its possible effect on the reaction is also covered. Phase separation and reaction in multicomponent systems are briefly discussed.

I. Thermodynamics of Silicon-Hydrogen-Oxygen System

The thermodynamic system considered contains three components, namely, silicon, oxygen and hydrogen, and two phases — solid and gas. The number of degrees of freedom f of this system can be calculated by the phase rule[1]

$$f = 2 + n - P = 2 + 3 - 2 = 3$$

where n is the number of system components and P is the number of phases. Therefore, the silicon-hydrogen-oxygen system has three degrees of freedom and three independent experimental variables. Usually, temperature is chosen as one independent variable as its effect on the reaction rate and product composition is of interest. Pressure is taken as the second independent variable. The final independent variable can be taken as the ratio of the total flux of hydrogen atoms J_H to the total flux of oxygen atoms J_o in the gas phase. This ratio may be converted to the ratio of J_{H_2}/J_{H_2O} because in the temperature range 1200°C~1400°C, nearly all oxygen atoms will combine with hydrogen atoms and form water vapor. This is evident by considering the ratio O_2/H_2O at 1600°K for

$$H_2 + \frac{1}{2} O_2 \rightarrow H_2O.$$

At 1600°K, ΔG for this reaction is -37.93Kcal.[2]

$$\Delta G = -RT \ln \frac{[H_2O]}{[H_2][O_2]^{1/2}}$$

$$[O_2]^{1/2} = [H_2O] \times 6.58 \times 10^{-6} \quad ([H_2] \cong 1)$$

$$[O_2] = [H_2O]^2 \times 4.33 \times 10^{-11}$$

$$\text{if } P_{H_2O} < 10^{-4} \text{ atm, then } P_{O_2} < 10^{-19} \text{ atm.}$$

The principal reaction between silica and hydrogen gas at these H_2 and H_2O pressures is

$$SiO_{2(s)} + H_{2(g)} = SiO_{(g)} + H_2O_{(g)} \qquad (1)$$

When the reaction is in dynamic equilibrium the reaction rate in the forward and reverse direction must be equal. The equilibrium constant is

$$K = \frac{P_{SiO} \cdot P_{H_2O}}{P_{H_2}} .$$

The value of K under standard conditions is less than unity. Therefore, the standard free energy is positive, and the reaction is not favored. One way to force the reaction to proceed to the right is to provide excess hydrogen gas and reduce the concentration of silicon monoxide and water vapor. In the kinetic studies steps were taken so that the equilibrium was not achieved. The equilibrium constant is related with the free energy of the total reaction as

$$K = \exp(^{-\Delta G}/RT).$$

Where ΔG is the change in Gibbs free energy, R is the universal gas constant and T is the absolute temperature. For a reaction at constant pressure and temperature, the associated energy change can be written in terms of ΔH, the heat of formation of the reaction product, and ΔS, the change in entropy as $\Delta G = \Delta H - T\Delta S$.

Values of ΔH and ΔS for species of the silicon dioxide, hydrogen and water system can be obtained from the JANAF Table. The reduction of silicon dioxide by reaction 1 has a positive heat, i.e. it is an endothermic reaction which involves an absorption of energy.

The equilibrium concentration of gas versus temperature for $P_{H_2} \cong$ 1 atm = P_{total} can be calculated as shown in the thermodynamic values listed below.

	(Kcal)	$SiO_{2(s)} + H_{2(g)} \rightarrow SiO_{(g)} + H_2O_{(g)}$		
	ΔG for crystobalite	quartz	K_{crist}	K_{quartz}
1300°K	69.2	69.03	2.48×10^{-12}	2.32×10^{-12}
1400°K	64.98	64.78	7.7×10^{-11}	7.17×10^{-11}
1500°K	60.4	60.16	1.71×10^{-9}	1.58×10^{-9}
1600°K	55.86	55.58	2.56×10^{-8}	2.34×10^{-8}
1700°K	51.34	51.04	2.74×10^{-7}	2.51×10^{-7}

It can be seen that as 2 moles of gas are produced for every 1 mole of reacting gas, the equilibrium constant increases with increasing temperature.

II. Kinetics of Redox Reaction

When chemical systems are in equilibrium, thermodynamics of the reaction should be considered. However, in some cases, for example at low temperatures, the reaction rate is limited by the surface reaction rate and equilibrium may not be established. On the contrary, at high temperatures, the reaction rate usually is limited by the gas-phase mass transfer in which case local equilibrium does exist. The slow step may change as a function of temperature. There are also other factors that affect the slowest step. For example, if the mass-transfer is the slowest step at some temperature, the mass transfer process can be very much accelerated by forced convection. If this rate exceeds that of the surface reaction, the surface reaction step becomes the rate determining step. The pressure and temperature dependence for different slowest steps

will be discussed in the following sections.

1) Mass Transfer Controlled Reaction Rate[3]

When the reaction rate is controlled by mass-transfer process, the rate can be described as:

$$J_A = K_C \Delta C_A$$

Where J_A is the molar mass transfer of species A measured relative to fixed spatial coordinates in moles/cm^2·hr, K_C is the convective mass-transfer coefficient in moles of A·cm/hr. The physical significance of this constant will be explored in the next section. ΔC_A is the concentration difference between the boundary surface concentration and the average concentration of the fluid stream of the diffusing species A in moles/cm^3.

In order to explore the physical significance of convective mass-transfer coefficient K_C, the boundary layer concept[4] is discussed below. The boundary layer concept was proposed by Ludwig Prandtl in 1904 and has been widely accepted until now. According to Prandtl's hypothesis, the effects of fluid friction at high Reynolds number are limited to a thin layer near the boundary of a body. Therefore, a conceptual boundary layer exists. Furthermore, there is no significant pressure change across the boundary layer. This picture greatly simplified the real system and made analytical treatment possible.

The general Equations which are valid for any type of fluid are

$$\rho \frac{DV_x}{Dt} = \rho g_x + \frac{\partial \sigma_{xx}}{\partial x} + \frac{\partial \tau_{yx}}{\partial y} + \frac{\partial \tau_{zx}}{\partial z}$$

$$\rho \frac{DV_y}{Dt} = \rho g_y + \frac{\partial \tau_{xy}}{\partial x} + \frac{\partial \sigma_{yy}}{\partial y} + \frac{\partial \tau_{zy}}{\partial z}$$

$$\rho \frac{DV_z}{Dt} = \rho g_z + \frac{\partial \tau_{xz}}{\partial x} + \frac{\partial \tau_{yz}}{\partial y} + \frac{\partial \sigma_{zz}}{\partial z}$$

$$\text{where } \frac{D}{Dt} = \frac{\partial}{\partial t} + V_x \frac{\partial}{\partial x} + V_y \frac{\partial}{\partial y} + V_z \frac{\partial}{\partial z}$$

For incompressible, laminar flow with constant viscosity, the above equations could be reduced into Navier-Stokes equation. These equations may then be expressed in a more compact form in the single vector equation:

$$\rho \frac{DV}{Dt} = \rho g - \nabla P + M\nabla^2 V$$

Blasius developed an exact solution for the hydrodynamic boundary layer for laminar flow parallel to a flat surface. The solution gives

$$\frac{K_c L}{D_{AB}} = 0.664 \ Re_L^{1/2}$$

where L is the length of the plate, D_{AB} is the mass diffusivity of species A in B, Re_L is the Reynolds number: $Re_L = \frac{\rho VL}{\mu}$ and is the ratio of inertial forces to viscous forces. (ρ = density of the fluid, V = velocity of the fluid, μ = viscosity of the fluid).

For the gas phase mass transfer, similar results can be obtained. The mass transfer coefficient is affected by the diffusivity D_G of the gas, the geometry of the object and the gas flow rate. An approximate derivation is given below.

The frictional force per unit area between two adjacent layers is

$$F = \mu \frac{\partial u}{\partial y}$$

u is the velocity of the stream, and $u = \frac{\partial x}{\partial t}$ for laminar flow.

The frictional force on an elemental area 1 x d x is Fdx = ma, which results in a deceleration of the fluid

$$m = P\ \delta(x)dx \qquad a = \frac{\partial u}{\partial t} = \frac{\partial u}{\partial x}\frac{\partial x}{\partial t} = u\frac{\partial u}{\partial x}$$

$$\frac{\partial u}{\partial y} = \frac{P}{\mu}\ \delta(x)\ u\ \frac{\partial u}{\partial x}$$

The boundary condition is that the velocity of the fluid next to the plate is zero. Approximate relations can be obtained by approximating the partial derivations by the quotients of differences: $\frac{\partial u}{\partial x} \rightarrow \frac{U}{x}$, $\frac{\partial u}{\partial y} \rightarrow \frac{U}{\delta(x)}$ and $u \rightarrow U$.

This gives $\delta(x) \simeq \left(\frac{\mu x}{PU}\right)^{1/2}$

$$\delta = \frac{1}{L}\int_o^L \delta(x)dx = \frac{2}{3}\frac{L}{\sqrt{Re_L}}$$

The gas phase mass-transfer coefficient K_C is given in terms of the average boundary layer thickness $\bar{\delta}$ and the diffusivity D_G by

$$K_C = \frac{D_G}{\delta} = \frac{3}{2}\ \frac{D_G}{L}\sqrt{Re_L}$$

This equation differs from that obtained by a more exact calculation by a factor of only 2. The gas-phase mass transfer coefficient is only a weak function of temperature ($D_{AB} \propto T^{3/2}$ for gaseous diffusion[3]). It increases with increasing Reynolds number. A Reynolds number greater than about 2000 indicates the flow in the tube is turbulent. For hydrogen gas at 1500°F, for a sample with L = 1cm, this will correspond to a velocity of about 180m/sec. Since ρ is decreasing with increasing

---

*Data from Welty, Wicks and Wilson, "Fundamentals of Momentum, Heat and Mass Transfer," p. 657. T=1500°F for hydrogen $\mu = 1.44 \times 10^{-5}$ lbm/ft sec
$\rho = 0.00141$ lbm/ft^3

temperature while μ is increasing with increasing temperature, at a higher temperature an even higher flow rate (velocity) is needed to cause a turbulent flow. This flow rate is too high to be practical in an ordinary furnace tube. A laminar flow is therefore expected in the furnace setup used in this experiment.

2) Reaction Controlled Mechanisms

When the mass transfer rate is much higher than the reaction rate at the surface, the surface reaction becomes the rate-determining step. The total gas-solid reaction can be divided into five stages, namely, 1) transport of the reactant to the surface, 2) chemisorption of reactant gas, 3) reaction, 4) desorption of product gas and 5) transport of product away from the surface. The mechanism of stage 1 and 5 under forced convection has been discussed in the previous section. In this section, the cases of stages 2, 3 or 4 being the rate determining step will be considered.

(a) If step (2) — chemisorption of the reactant gas (H_2 in this case) becomes the slowest step, all the steps before and after chemisorption will be much faster. Then the partial pressure of H_2 near the silica surface will be at equilibrium with the flow gas, i.e. equal to 1 atm because mass transfer is by far the faster step. The surface is assumed to consist of a certain number of sites which are all available for chemisorption (because the reaction and desorption are also much faster). From the Langmuir model[5] the rate will be proportional to the product of pressure and the number of free sites which is a constant property of the solid. Therefore, the rate equation can be written as: $R = K_1 P$ where R = rate of the reaction, P = pressure of the gas being chemisorbed and K_1

= a constant, and K_1 can be expressed as a function of temperature:

$$K_1 = [NC\sigma^\circ \exp(-Ea^*/RT)] \Big/ (2\pi MRT)^{1/2} = A \exp(-Ea^*/RT)$$

The above equation indicates that the adsorption rate was taken simply to be the rate at which molecules from the gas phase would strike a site area σ° times the condensation constant C, which is the fraction of the molecule that will stick. Besides, the adsorption is activated (otherwise it will not become the slowest step), the fraction of molecules hitting and sticking that can proceed to a chemisorbed state is given by $\exp(-Ea^*/RT)$ where Ea^* is the activation energy for the chemisorption reaction. In the above representation, it is implicitly assumed that all the surface sites are homogeneous which is expected to be the case for the glassy phase.

(b) If step (3) — surface reaction is the rate-determining step, then the rate equation can be written as $R = K_2'' [H_2] \cdot [SiO_2] = K_2' [H_2] = K_2 \cdot P_{H_2}$ for the reaction (1) $H_2 + SiO_2 \rightarrow SiO + H_2O$ for molecularly chemisorbed hydrogen.

Where $[H_2]$ is the chemisorbed hydrogen concentration, the total rate is proportional to the partial pressure of hydrogen gas.

However, if the hydrogen molecules dissociate into adsorbed atoms, and the reaction mechanism is $A + H_{ads} \rightarrow A.H$ (1) and $A \cdot H + H_{ads} \rightarrow HAH$ (2) and either step (1) or (2) is the slowest step, the reaction rate will be proportional to the root mean square of the partial pressure of hydrogen

$$R = K_2 [H_2]^{1/2}.$$

It can be seen that the chemical reaction mechanism is difficult to pin down. Different mechanisms may give the same dependence. A mechanism can only be proved wrong but never proved correct. Again K_2 can be expressed as a function of temperature

$$K_2(T) = A \exp(-E_a/RT)$$

where E_a is the activation energy for the reaction.

(c) If the desorption of products is the rate-limiting step, similar relationships can be derived. The products of the reaction are silicon monoxide and water vapor. From the mass balance consideration, if there is no residue then both product species are desorbed at the same rate. As they are products of the reaction and have negligible initial concentrations, their concentrations must be equal, i.e. $[SiO_{ads}] = [H_2O_{ads}] = C$.

The rate equation can be written as

$$R = K_3 C$$

and $K_3 = A' \exp(-Ed^*/RT)$

where A' is a constant, Ed^* is the activation energy of desorption and $Ed^* = Ea^* + \theta$ where Ea^* is the adsorption activation energy for the same chemical species and θ is the energy of adsorption. When the desorption is the rate limiting step, the surface reaction rate is faster and equilibrium can be achieved.

From equation (1) $K = \dfrac{C_{H_2}}{C_{H_2O} \cdot C_{SiO}}$

$$C = C_{H_2O} = C_{SiO} = \frac{1}{K} C_{H_2}^{1/2} = K' P_{H_2}^{1/2}$$

$$R = K_3' P_{H_2}^{1/2}$$

Therefore, the rate will be proportional to the square root of hydrogen gas partial pressure, while similar temperature dependence will still hold. Besides the mechanisms discussed above, the heat transfer mechanism may also affect kinetics of the reaction in some cases, it will be discussed in the following section.

III. Heat Transfer Mechanisms in the Sample

The heat transfer through silica glass can be by either phonons or photons. These two mechanisms are discussed briefly below.

(1) Phonons: The energy in a lattice vibration or elastic wave is quantized. The quantum of energy in an elastic wave is called a phonon. The transfer of energy in a dielectric solid can be viewed as the propagation of anharmonic lattice waves through a continuum or as the interaction between quanta of vibrational thermal energy. The thermal conductivity coefficient K of a solid is defined by the equation

$$Q = K\frac{dT}{dx}$$

where Q is the flux of thermal energy, and $\frac{dT}{dx}$ is the temperature gradient.

The temperature gradient term, similar to the concentration gradient term in the diffusion process indicates that the process of thermal energy transfer is random. The random nature of the conductivity process brings a mean free path into the expression for the thermal flux. By analogy with the molecular mean free path and the kinetic theory of gases,[6] the thermal conductivity can be expressed as $K = \frac{1}{3} C\nu\ell$.

Where C is the heat capacity per unit volume, ν is the average particle velocity and ℓ is the mean free path of a particle between collisions. This result was applied by Debye to describe thermal conductivity in dielectric solids, with C as the heat capacity of the phonons, ν the

phonon velocity, and ℓ the phonon mean free path. The phonon mean free path ℓ is determined principally by two processes, geometrical scattering and scattering by other phonons. The lattice structure of glass does not have the periodicity and symmetry of a crystal lattice. The mean free path of phonon, ℓ, in this case is short. It is independent of temperature and of the order of the dimension of the structural unit (the silica tetrahedra) at high temperatures. The phonon velocity is constant. As a result, the conductivity is proportional to the specific heat at most temperatures. Since the specific heat is nearly constant at temperatures above the Debye temperature, the thermal conductivity becomes nearly constant at temperatures above a value near room temperature.[7]

(2) Photons: In addition to heat energy transfer by vibrational modes, heat may be transferred through the solid by transmission or absorption and reradiation of electromagnetic energy. In transparent materials, unlike the more familiar opaque materials, the emission and absorption of radiation are bulk, rather than surface, phenomena. Interaction of the simultaneous emission and absorption of radiation throughout the volume leads to a mechanism of radiative heat transfer in the interior of transparent materials. This requires not only the familiar radiation through these referred layers but also internal radiant exchanges between nearby layers. By analogy with thermal conduction an equivalent "radiative conductivity" has been defined. This is different to that of opaque materials, in which heat flows by thermal conduction only. For gray body material the radiative conductivity can be expressed as a function of temperature.[8]

$$k_{rad} = \frac{16n^2\sigma T^3}{3\gamma}$$

where n is the refractive index of the material, γ is its absorption coefficient defined by the equation $I_x = I_o e^{-\gamma x}$, and σ is the Stefan-Boltzmann constant. The T^3 dependence makes this conductivity a very sensitive function of temperature, and at high temperatures it becomes far more important than the true thermal conductivity of glasses.

At high temperatures, the combination of high 'radiative conductivity' and low thermal conductivity for transparent materials results in a different temperature profile. The bulk of the sample is at a higher temperature and decreases to a lower temperature at the surface. The temperature gradient near the surface becomes steeper due to the cooling effect from the presence of a constant flowing gas that is at an even lower temperature. This temperature profile will affect the reaction rate at the surface and bring about a special surface morphology for transparent glasses. Because of the very high heat capacity of the hydrogen gas, the cooling effect due to flowing gas becomes more significant at a higher flow rate of hydrogen gas. The drilling effect is also expected to become more pronounced at a higher flow rate of hydrogen gas.

IV. Multicomponent System and Reaction Mechanism

In the silica glass and hydrogen gas reaction, the solid phase is considered as a homogeneous single phase. In the previous sections, the thermodynamics and kinetics considerations were based on the homogeneous solid phase. However, in the multicomponent glass system, the solid is no longer a single homogeneous phase. Crystallization and phase separation occurred upon reheating. Each solid sample contained more than one single phase. Spinodal decomposition and nucleation with subsequent crystal growth are two mechanisms for the observed phase separation. In the

alumino-silicate system, a metastable liquid immiscibility between 7 and 55 mole% of Al_2O_3 is found.[9] The phase separation on the cooling stage in the glass formation process is due to this liquid immiscibility. This phase separation helps the nucleation of finely divided mullite on reheating these glasses above 1000°C. Crystallization of the siliceous matrix of mullite glass-ceramics to cristobalite normally occurs internally in radial sperulitic orientation when heated above 1200°C. A small addition of modifying oxides such as the alkalis and alkaline earths allow tetrahedral coordination of most of the Al^{3+} and therefore reduce the tendency toward phase separation. This, in turn, tends to reduce or inhibit crystallization of mullite and cristobalite. However, heating to a higher temperature will still cause crystallization. It is important to recognize that phase separation can occur in the multicomponent system. Besides, as the reaction with hydrogen gas goes on, a residue is left behind. At temperatures below 1500°C, the reaction rate between alumina and hydrogen gas is negligible. When silica is etched out, the alumina is left behind and forms a new surface layer. It is hoped that by sintering the residue into a dense layer, a better corrosion resistance can be obtained. A better errosion resistance is also expected. Therefore, a corrosion and errosion resistant material may be formed through forming a surface layer first by reaction with hydrogen gas and then sintering of this surface layer into a dense layer.

EXPERIMENTAL

I. Apparatus

1) Hydrogen Gas Corrosion

A hydrogen furnace was built for corrosion testing of samples. A schematic of the hydrogen furnace system is shown in Fig. 1. A carrier gas (usually argon or helium) is available. The flow rate is controlled by a regulator and a set of valves, and monitored by a flow meter. A palladium-silver hydrogen diffusion purifier was installed. The capacity of this unit is about 100 c.c. (S.T.P.)/min which is much less than the rate that was found to be required in this study. It was thus bypassed. An ice water cold trap was found to be necessary to condense the reaction products (mostly H_2O) in order to prevent clogging of the flow valve and check valve. An alumina tube is used because of its corrosion resistance to hydrogen gas, but it is vulnerable to thermal shock. Design features and proper control of heating and cooling rates had to be introduced to minimize thermal shock problems. Figure 2 is a cross-sectional sketch of the furnace itself. Inside the alumina tube, two improvements were made: (i) Baffles were introduced as a heat exchanger to heat up the incoming hydrogen gas. They also reduced the heat loss from the ends of the furnace tube and thus provided a suitable uniform hot zone at a lower power consumption rate. (ii) A sample holder was designed to effectively reduce the total cross-section of the tube so as to get a high linear gas flow velocity past the specimens with a much lower volume flow rate to reduce the gas consumption rate as well as the power consumption rate. In order to study the kinetics of the reaction, the linear flow rate of the gas past the surface of the

specimens should be high enough so that the surface reaction becomes the rate limiting step for pore-free samples. Otherwise, the mass transfer of the reactants and products through the stagnant surface gas layer may become the rate limiting step.

It is shown in Fig. 2 that a 36 inch long alumina tube (O.D. = 3.25" I.D. = 2.93") is placed inside a 20 inch long alumina core (O.D. = 4", I.D. = 3.5") which has 6 grooves per inch. It was wound with a 0.040 inch diameter, 60% Pt/40% Rh wire. Four inches on both the left and right ends were not wound. Power leads extend out of each end of the insulation shell. The winding is covered with EA-139 alumdum cement. The wound furnace core was wrapped with five sheets of 20" x 24" x 0.2" zirca felt. It was then wrapped with a piece of wax paper. With one transite end plate in a horizontal position, the furnace core was mounted in a vertical position. Four 2" x 6" x 20" sections of Vee-Block, and three tie rods were set upright in the annular space. Vee castable (putty-like consistency) was then added to fill up the annular space. The other transite end plate was set in place, and the whole assemblage bolted together. After several days of room temperature drying, the initial firing was accomplished by slowly raising the temperature to 900°C over a period of several days. The use of castable eliminates channels through which heat can be lost (compared to fitted brick). The wax paper around the zirca felt keeps it from coming in contact with the wet castable slurry. The wax paper is burnt in the initial firing.

A Pt-Pt/10Rh thermocouple was used to measure the temperature. Since the thermocouple reacts with hydrogen gas, it was placed inside a 0.4"-diameter alumina tube. Figure 3 shows that the hot zone was relatively uniform

over a distance of 10 cm. In each run, the specimens and the thermocouple were placed in this hot zone.

A "Davis Combustible Gas Detector System — series 3800" sensor is hung from the ceiling over the furnace to detect any leakage of hydrogen gas. The control box is kept close to the furnace. The alarm is set to be activated when the hydrogen gas concentration around the sensor reaches 20 to 22% of the lower explosion level (L.E.L.). The safety system is regularly checked and examined by safety engineers from L.B.L. and campus. A portable hydrogen detector is used to track down any leaks in the furnace system. All the gas products, including the unreacted hydrogen gas, were dissipated outdoors.

2) Hydrofluoric Acid Solution Corrosion

A constant temperature water bath shaker was used to study the reaction between silicate glasses and hydrofluoric acid solution. A solid state time proportioning heat control allowed precise temperature control within the range of -10°C to 100°C. A cooling core is necessary from ambient temperature to -10°C. The oscillation speed was varied from 20 to 200 osc/min. Polyethylene bottles were used as containers for the hydrofluoric acid solution. Samples were hung in a net of platinum wire from the top of the bottles.

II. Material Preparation

Nine silicate glasses were used. Their compositions are listed in Fig. 4. The silica glass was obtained from Amersil Co. as a 9mm-diameter rod which was first cut into 2mm thick discs. The as-cut glass discs were treated with hydrofluoric acid solution to remove microcracks caused by abrasion of the diamond saw. The impurity content of the Amersil silica glass was analyzed by American Spectrographic Laboratories spectrographically: SiO_2 - major constituent, Al_2O_3 - 0.045, FeO - 0.015, MgO - 0.0007, CaO - 0.0005, and CuO - 0.0005 wt%.

The other silicate glasses were prepared by Corning Glass Works. The as-received glass chunks were first core drilled into 9mm diameter cylinders and then cut into 2mm thick discs. Hydrofluoric acid solution was used to remove the surface layer and provide a uniform surface morphology. After this treatment, the glasses were stored in a dessicator until ready to use.

The mullite sample with 73 wt% Al_2O_3 was prepared in this laboratory. It was cold pressed into a 0.90cm diameter disc and sintered in air at 1600°C. The as-sintered mullite discs were used without any treatment. Its microstructure is shown in Fig. 5. It is theoretically dense because of the presence of the glassy phase at the grain boundaries.

Hydrogen gas with a reported purity of 99.999% and a dew point of -120°F was provided by Lawrence Berkeley Laboratory (LBL). The listed impurities are water vapor, 0.25 p.p.m. and oxygen, 1.5 p.p.m. The argon and helium gas were also provided by LBL and were 99.999% and 99.998% pure, respectively

The hydrofluoric acid solution was obtained commercially. The as-received hydrofluoric acid solution is 52 wt% HF, or 30M (moles of HF/liter). It was diluted with distilled water to make solutions of specified concentrations.

III. Experimental Procedure

The gravimetric method was used to measure the reaction rate. Samples were weighed before and after the reaction. The weight loss divided by reaction time and surface area gives the reaction rate. The procedure in running a hydrogen reaction test consisted of inserting the specimen into the furnace at an accurately specified position, pumping to vacuum, adding inert gas — Argon or Helium, raising the temperature to the specified temperature, holding for 30 minutes to insure a thermal equilibrium, introducing flowing hydrogen gas at atmospheric pressure for the desired time and at the desired rate of flow, introducing inert gas, and cooling.

The volume flow rate of hydrogen gas and/or inert carrier gas were measured by flow meters. The linear flow speed past the sample is calculated by dividing the volume flow rate by the total cross section of holes on the sample holder. The hydrogen flow meter is made by Fisher and Porter Co. and the calibration curve is plotted in Fig. 6.

The surfaces of the reacted samples were examined by an optical microscope and a scanning electron microscope. When a scanning electron microscope is used, the sample has to be coated with a layer of gold by sputtering. Usually a tilt angle of 30° was used.

The presence of crystalline phases was determined by x-ray diffraction. Chemical compositions and the concentration profiles were

determined with the electron microprobe. Before electron microprobe analyses, the samples were polished to a quarter micron grade and coated with a carbon film by vapor deposition.

When the reacted sample had a porous structure, the carbon did not stick to the surface due to the evaporation of oil that was absorbed during polishing. Also, the porous structure was subject to distortion during the polishing process. A vacuum mounting method was developed to overcome this difficulty. The sample was placed in a chamber which was pumped down below a pressure of 1 torr, and epoxy was then introduced as a mounting material. The epoxy flowed into the evacuated channels of the porous specimen. Distortion of the specimen was thus prevented during polishing. The pressure of the chamber requires careful control since epoxy decomposes at very low pressures. The curing time of the epoxy is controlled in order to adjust its hardness. Usually, it takes two to eight hours.

All the microprobe measurements were made with an accelerating voltage of 15 KV and a specimen current of 0.03μA. The concentration profile was obtained by traversing the electron beam of ~1μm diameter perpendicular to the reaction front.

If large fluctuations were present because of either phase separation or porosity, line scanning of 50 ~100μm parallel to the reaction front was applied to every point to obtain an average composition and a smooth curve. An integrated count per ten seconds was monitored by logic circuit counters and simultaneously punched on IBM cards. The data were corrected by computer with magic IV program for absorption, fluorescence, atomic number, dead time, drift and background. The corrected data were

printed and plotted when requested.

RESULTS AND DISCUSSION

I. Reaction Between Silica Glass and Hydrogen Gas

1) Devitrification of Silica Glass:

It was observed that silica glass devitrified in the hydrogen atmosphere in the temperature range 1200°C to 1400°C. The product of this devitrification reaction was identified as cristobalite by x-ray diffraction. The extent of devitrification was found to be a function of reaction temperature and time. The formation of the cristobalite starts at the surface of the glass sample and propagates toward the center. Upon cooling, high or β cristobalite undergoes a displacive transformation to low or α cristobalite in the temperature range of 270 and 200°C. As a result of the large difference in the expansion coefficients of these high and low forms, cristobalite cracks upon transformation. Because a gravimetric method was used to monitor the reaction rate, cracking of the sample was undesirable since the loss of a small portion of the sample due to cracking could result in a large experimental error. Therefore, eliminating the devitrification phenomenon was critical to the kinetic study. A series of qualitative observations revealed that the devitrification phenomenon decreased in extent with continuous use of the furnace tube. It was suspected that devitrification was caused by some vapor contaminants. Heating a piece of silica glass in air to the same temperature did not result in devitrification of the glass.

By analyzing the condensate in the cold trap of the hydrogen furnace (Fig. 1), sodium and a small amount of potassium were identified as the major components by the Energy Dispersive X-ray Analysis (EDAX). Without a cold trap, sodium accumulated in the valves; upon hydration the valves

became clogged. The cold trap was thus necessary for normal operation of the hydrogen furnace system.

The source of sodium and potassium was the alumina tube which was ~95% pure. No alumina tube of higher purity was commercially available. Sodium oxide and potassium oxide are always present in commercial alumina products. From the literature,[10] it is known that sodium silicate glass has a much stronger tendency to devitrify than fused silica. This can be seen from the critical cooling rate for glass formation: SiO_2, 10^{-4} ~10^{-3} $^{\circ}K/_{sec}$; $Na_2O \cdot SiO_2$, 1 ~50 $^{\circ}K/_{sec}$.

In the presence of hydrogen gas, the sodium oxide and potassium oxide in the alumina tube are reduced to sodium and potassium vapor and are carried along by the flowing gas. Deposition on the silica glass occurs as a result of high concentration of water vapor near the silica surface due to the reaction of silica and hydrogen. Such deposition results in the initiation of the devitrification of the silica glass on the surface. Therefore, if the sodium oxide could be removed from the tube, the devitrification of the silica glass should be halted. To achieve this objective, each new alumina tube was heated in flowing hydrogen at 1500°C for about 24 hours. Such treatment eliminated the devitrification of silica glass in the hydrogen furnace.was eliminated.

2) Weight Loss in Hydrogen: Reaction or Decomposition

In the presence of hydrogen gas, silica glass shows a weight loss at high temperatures. This loss may be due to a reaction with hydrogen gas as

$$SiO_{2(s)} + H_{2(g)} \rightarrow SiO_{(g)} + H_2O_{(g)} \qquad (1)$$

or to decomposition in a very low oxygen partial pressure, as

$$SiO_{2(s)} \rightarrow SiO_{(g)} + \frac{1}{2} O_{2(g)} \quad (2)$$

The equilibrium partial pressure in the presence of hydrogen gas with a partial pressure ~1 atm is calculated as (see Introduction)

$$P_{O_2} = P_{H_2O}^{\ 2} \times 4.33 \times 10^{-11} \quad (3)$$

In order to estimate the partial pressure of water vapor, the reaction of Eq. (1) has to be considered. At 1600°K

$$\Delta G = -56.24 - 37.93 + 150.03 = 55.86 \text{ Kcal}$$

$$\Delta G = -RT \ \ell nK_{eq} = -RT \ \ell n \frac{[SiO][H_2O]}{[H_2]}$$

$$55.86 \times 10^3 = -1.987 \times 1600 \ \ell n \frac{[SiO][H_2O]}{[H_2]}$$

Since $[H_2] = \sim 1$,

$$[H_2O][SiO] = 2.3 \times 10^{-8}$$

If $[H_2O] = \sim[SiO]$, then

$$[H_2O] = \sim[SiO] = 1.5 \times 10^{-4} \quad (4)$$

This is the maximum equilibrium value predicted by thermodynamic calculations. Substituting Eq. (4) into Eq. (3)

$$[O_2] \leqq 10^{-19} \quad (5)$$

It should be noted that without reaction (1), the partial pressure of water vapor is reported to be lower than 10^{-6} atm in the hydrogen

bottle provided by LBL. The oxygen partial pressure is even lower. Now, let us consider the thermodynamic data for the decomposition reaction of Eq. (2). At 1600°K

$$\Delta G = 93.8 \text{ Kcal} = -RT \ln [SiO][O_2]^{\frac{1}{2}}$$

$$[SiO][O_2]^{\frac{1}{2}} = 1.54 \times 10^{-13} \tag{6}$$

Substituting Eq. (5) into Eq. (6)

$$[SiO] = \sim 5 \times 10^{-3} \tag{7}$$

The empirical weight loss rate of SiO_2 at 1600°K is $\sim 2.5 \times 10^{-3}$ g/hr·sm^2 ($\sim 4.2 \times 10^{-5}$ mole/hr·cm^2). From the equation $J = 44.33 \frac{P_{SiO}}{\sqrt{MT}}$ we obtain

$$\frac{4.2 \times 10^{-5}}{3600(\text{sec})} = 44.33 \frac{P_{SiO}}{\sqrt{44 \times 1600}}$$

$$P_{SiO} = \sim 10^{-7} \text{ atm} \tag{8}$$

From Eqs. (4), (7) and (8), it can be seen that both reactions (1) and (2) are thermodynamically favorable. Which one is responsible for the weight loss is determined by the kinetics of these reactions. The following experiment was performed. A low partial pressure of oxygen in the absence of hydrogen was provided to ascertain whether or not a weight loss occurred. A piece of silica glass was heated in a tantalum furnace in vacuum (10^{-6} $\sim 10^{-7}$ torr) in the presence of titanium wool at 1300°C for one day. No weight loss was observed. As both tantalum and titanium are oxygen getters, a very low partial pressure of oxygen must have been present. The lack of weight loss excluded the possible mechanism of

decomposition as represented by Eq. (2). However, previous studies[11] showed decomposition and volatilization of silica are significant in vacuum at higher temperatures (~1600°C). In the temperature range of this study, weight loss is then due to the hydrogen according to Eq. 1.

3) Temperature Consideration

Reaction rates are in general strongly dependent upon the temperature. Therefore, rate measurements should be made at a measured constant temperature. In these kinetic studies, a high flow rate of hydrogen gas was maintained to avoid the gas phase transport mechanism becoming the rate limiting step. Because the hydrogen gas has a high heat capacity, the flowing hydrogen gas will carry a considerable amount of heat away. This behavior imposes a limitation on the maximum temperature that the furnace can reach. Moreover, the flowing gas is at a lower temperature than the glass sample. Even though a set of baffles is introduced to provide a uniform hot zone and to heat up the incoming hydrogen gas, it is still expected that the hydrogen gas flowing at such a high volume rate will not become thermally equilibrated with the furnace and hence will be at a lower temperature than the glass samples. The thermocouple was kept as close to the sample as possible and the temperature was monitored continuously so that the sample temperature is as closely monitored as possible.

As pure silica glass remained transparent during the reaction, it is expected that a temperature variation existed inside the glass sample. The other glasses became opaque with initiation of the reaction. In these cases, the temperature of the samples should be similar to the temperature of the furnace.

4) The Effect of Gas Flow Rate on Total Reaction Rate

It was found that the total reaction rate was dependent on the hydrogen gas flow rate as seen in Fig. 7. At a very low flow rate, the total reaction rate was negligible. As the flow rate increased, the total reaction rate also increased. In this range, generally known as the transport influenced range, the higher flow rate tends to decrease the thickness of the stagnant surface layer. Therefore, the transport rate through this stagnant layer is increased and so is the total reaction rate. As the flow rate increases past a certain value, the total reaction rate becomes fairly constant and is independent of the flow rate. This behavior is due to the transition of the slowest step of the reaction from transport controlled to kinetics controlled. Further increase of the flow rate introduced a larger fluctuation and made experimental results less reproducible. This effect is probably due to the cooling effect of the flowing hydrogen gas at a very high volume flow rate. The hydrogen gas has a high heat conductivity. A high volume flow rate can seriously change the temperature profile inside the furnace. Higher flow rates tend to shift the hot zone toward the downstream side of the furnace. Besides, at a certain flow rate, the furnace may not provide enough power and the temperature will be lower than specified. Therefore, a low volume flow rate of hydrogen gas with a high linear flow speed past the sample made the sample holder a necessary part of the furnace assembly.

5) Surface Morphology after Reaction with Hydrogen Gas

The reacted silica glass has an unusual surface morphology. Figure 8 shows the change in the surface morphology with increasing reaction

time at 1300°C. A set of as-cut silica glass samples was used. The as-cut glass sample had microcracks on the surface and was therefore not transparent. Figure 8A shows the surface after only a slight reaction. As the reaction proceeded, the surface layer which was full of microcracks completely disappeared as seen in Fig. 8B. At this stage, the glass became transparent again. Small holes started to form and, once formed, tended to grow (Figs. 8C, D, E, F). This kind of drilling effect was found to be unique to the silica glass; it was not shown on silicate glasses, which became opaque after reaction. This morphology is due to the temperature gradient in the transparent glass sample. At the tip of the hole, the temperature is higher than at the surface. Accordingly, the reaction rate at the tip of the hole will also be higher. The difference in the reaction rates means that the hole becomes deeper and deeper. The product concentration is also higher at the tip of the hole than at the surface. This conclusion is supported by Fig. 9 which shows the formation of cristobalite on the ridges. Apparently, silicon monoxide and water vapor on leaving the pits become oversaturated when they come into contact with the cooler hydrogen gas.

The reaction is complex. The rate determined from weight loss and apparent surface area data is not the true reaction rate. The actual surface area is larger than the surface area calculated from the overall geometric shape. The actual rate is thus lower than the indicated calculated rate. On the other hand, the redeposition of cristobalite reduces the observed weight loss and makes the true reaction rate higher than the calculated rate. The temperature gradient makes it even more complex. A simple explanation of the apparent activation energy and the

rate values is not feasible. Bearing this in mind, the kinetic study results are given and discussed in the next section.

It is interesting to compare this surface morphology with that for fused silica reacted with hydrofluoric acid solution in which case the mass transfer is the slowest step.

6) Reaction Rate and Apparent Activation Energy

The weight loss divided by the surface area of the sample calculated from its geometric shape was plotted against the total reaction time in Fig. 10. By least-squares fitting, the slope of the curve was obtained as the reaction rate at a specified temperature. The apparent activation energy can be obtained by plotting the reaction rate versus the reciprocal of temperature as shown in Fig. 11. As discussed in the previous section, there is no simple explanation of the apparent activation energy. Moreover, as the surface roughening effect was more significant at higher temperatures with larger weight losses, the activation energy should be lower than the value obtained. After adjustments for the indicated difficulties, the true activation energy would be obtained. It indicates the energy barrier of the slowest step. Further investigations were carried out in an attempt to determine the reaction mechanism.

7) Effect of Dilution of Hydrogen Gas on the Reaction

The dependence of the reaction rate on the partial pressure of hydrogen gas was studied. The hydrogen gas was diluted by either argon or helium gas. The reaction rates showed striking differences. The reaction rate variation with partial pressure of hydrogen is shown in

Fig. 12. When the hydrogen gas was diluted by helium, the reaction rate decreased slightly. The apparent linear dependence of the data is not true taking into account the limiting points. Consideration of the helium curve (Fig. 12) shows a likely root mean square dependence on the partial pressure of hydrogen. On the contrary, a small amount of argon gas greatly reduced the reaction rate and further dilution had only a slight effect. As both helium and argon are inert gases, no chemical reaction is expected. Schwerdtfeger[12] explained this difference as an indication of a diffusion controlled mechanism. But the difference in the diffusivity of the product gas through different gas mixtures can not account for such a large difference. A possible explanation is that the argon gas was significantly enriched inside the furnace tube.

Figure 13 shows the cross-section of the furnace tube assembly. The alumina tube area is four hundred times that of the stainless steel tube area. At steady state, the incoming flux must be equal to the outgoing flux. (Since the reaction rate is so low, the little change in the gas composition caused by the reaction can be neglected when the flow rate is high.) Inside the tube, the speeds of the gas molecules are different due to the difference in their mass. The hydrogen gas with a much lower mass will travel at a much higher speed because $\frac{3}{2}KT = \frac{1}{2}mV^2$. Therefore, at point B, the escape probabilities can be different for the gases. The hydrogen gas with a higher speed will have a larger escape probability. The argon gas molecules will then accumulate until the concentration difference is large enough to compensate for the difference in their speed. Since the total pressure remains constant, the enrichment of the argon gas results in a decrease in the partial pressure of the hydrogen gas inside the

alumina tube. A quantitative analysis is too complex to be feasible. A crude estimate gives a mole ratio N_{Ar}/N_{H_2} of about 5 if it is assumed that the escape probability is proportional to the product of molecular number and collision frequency at the cross-section which is in turn proportional to the speed of the gas molecules.

Lack of dependence of the reaction rate on the flow rate of the reacting gas beyond a critical flow rate and the observed drilling effect suggest that the mass transfer process is not the slowest step. A significant contrast exists between the reaction with hydrogen gas and hydrofluoric acid solution in which case the mass transport is the the slowest step. This will be discussed in Part E under Results and Discussion. The total reaction rate varied roughly as the square root of partial pressure of hydrogen gas when diluted by helium gas. Such a pressure dependence excludes the possibility that adsorption is the slowest step. Therefore, either surface reaction or desorption is the slowest step for this reaction. It is difficult to distinguish between them. The desorption process is more likely to be the slowest step since previous studies[13] indicate that water vapor has a very strong affinity for silica. The strong interaction between them could make desorption the slowest step.

II. Reaction Between Alumino-silicate Glasses and Hydrogen Gas

1) Phase Separation and Crystallization

The phase diagram for this system is shown in Fig. 14. Phase separation can occur due to the metastable immiscibility gap in the system which can be a precursor to crystallization. Previous studies[9] indicate that crystallization occurs in alumino-silicate glasses upon heating above 1000°C. However, the crystalline phase remains very small so that the sample is still translucent to transparent. The extent of crystallization was monitored by the x-ray diffraction peak heights and density. Figure 15 shows the x-ray diffraction results for L glass (30 wt% Al_2O_3). The top curve was obtained after a heat treatment at 1200°C for 10 hours and showed only mullite crystallization. Cristobalite crystallization occurred on a subsequent heating at 1300°C for a further 10 hours as shown by the lower curve. A comparison of these two curves shows that at 1200°C crystallization of cristobalite is a slower process than is mullitization and that the mullite crystallization is not complete after 10 hours. The other alumino-silicate glass K (20 wt% Al_2O_3) behaves similarly. It is apparent that alumino-silicate glasses used in the hydrogen gas corrosion test contain three phases, namely mullite, cristobalite, and the remaining glass matrix and are therefore no longer single phase, homogeneous materials.

2) Surface Morphology of Reacted Alumino-silicate Glasses

As the reaction rate of alumina with hydrogen gas is much slower than that of silica, alumina is left behind as silica is etched away. The residue forms a new opaque surface layer identified as α-alumina. A set of 'rosettes' formed on this alumina layer at 1350°C and 1400°C after reaction with hydrogen as shown in Fig. 16. At 1500°C the rosette pattern

disappears. The formation of the rosette pattern is related to the cristobalite phase. It is reported[9] that crystallization to cristobalite normally occurs with spherulitic orientation in alumino-silicate glasses when these materials are heated above 1200°C. As cristobalite has a higher reaction rate, a depression in the shape of a rosette is formed. At 1500°C, the surface diffusion rate is high compared to the reaction rate and thus the resulting surface morphology is much smoother. This kind of surface morphology is unique to alumino-silicate glasses. In the silicate glasses with lime addition, in which the cristobalite did not form, such a morphology was not found. The molybdenum spheres shown on the picture at 1500°C (Fig. 16) apparently are impurities introduced in the glass preparation process. Cracks were also found on the alumina layer in Fig. 16. As alumina has a higher expansion coefficient than the core, a tensile stress results in the alumina layer upon cooling causing cracks to occur.

3) Reaction with Hydrogen Gas

L glass (30 wt% Al_2O_3) was used for the kinetic study. The reaction rate plotted against the reciprocal of temperature is shown in Fig. 17. It was found that the total reaction rate (compared to that of silica glass) is suppressed by the addition of alumina. The decrease in total reaction rate was found to be much greater than that expected from a weight ratio consideration (Fig. 18). The alumina added stabilizes the silica toward the reaction with hydrogen gas.

It is interesting to note that in the petroleum industry, alumino-silicates are generally used as catalysts for cracking. These alumino-silicate catalysts can be either amorphous or crystalline (mostly

zeolites). They are not simple mixtures of alumina and silica. This is evident from the fact that a combination of silica and alumina is much more effective than alumina or silica alone. Typical silica-alumina cracking catalysts contain silica in excess, the amount of alumina being 10~25 wt%, which is close to the composition used in this study. In such materials, the structure may be viewed as tetrahedrally coordinated silicon and aluminum atoms linked through the sharing of oxygen atoms at the corners of SiO_4 and AlO_4 tetrahedra. For aluminum containing tetrahedra bonded at all four corners to silicon atoms there is an excess negative charge. A compensating positive charge must be present to provide electroneutrality for the trivalent aluminum atom. A proton coordinated to the structure satisfies this requirement, and is strongly acidic. Figure 19(a) shows the structure of a silica alumina catalyst dried at low temperature (100°C), exhibiting Bronsted acid sites. Heating to elevated temperatures leads to a new structure as in Fig. 19(b). The aluminum atom in this state is unsaturated and can serve as an acceptor for a pair of electrons. Hence, it functions as a Lewis acid site. This structure provides an explanation for the strong affinity of water vapor or the hydroxyl radical to the alumino-silicate material. In the reaction with hydrogen gas, the increased interactions with the hydroxyl radical and water vapor tend to make the desorption an even slower step. This is consistent with the observation that the addition of alumina slows the reaction.

4) Concentration Profile of Reacted Alumino-silicate Glass

The concentration profile of the reacted L glass (30 wt% Al_2O_3), was obtained by electron probe microanalysis. The profile (Fig. 20) shows

that there are two layers. In the figure the distance from 0 to 23 marks a portion of unreacted core, 44 to 260 the intermediate transition layer and 270 to 330 the surface alumina layer. The distances 23 to 44 and 260 to 270, where large fluctuations occur due to normalization of the data correspond to the cracks between different layers.

Both the transition layer and alumina layer are porous, as evidenced by the fact that during the polishing process the color of the diamond grit was absorbed into the surface of these layers. In the coating process the carbon did not adhere due to the evaporation of the absorbed polishing oil. The carbon adhered to the surface of a vacuum mounted sample. The density calculated from data obtained by electron probe microanalysis on a vacuum mounted sample (Fig. 21) confirmed the existence of porosity in these layers. However, these pores or channels are extremely small. No pore structure could be observed by scanning electron microscopy. Moreover, the alumina reading in the transition layer without normalization (Fig. 22) (c.f. the readings are normalized in Fig. 20) showed little fluctuation. This indicates that the pore size is much smaller than the electron beam size so that an average value is always obtained. The electron beam size is of the order of a micron implying that the pore or channel sizes are of the order of 10^2 Å or less.

A comparison of Figs. 20 and 22 shows the difference between raw data and data normalized to 100%. The slope of the alumina concentration in Fig. 20 is caused by the silica concentration gradient. It is not observed in Fig. 22 and is therefore not real. In Fig. 22, the slight increase in the alumina intensity in the transition layer over that in the unreacted core indicates a contraction of the residue. The

fluctuations in the alumina layer suggest non-uniform sintering of alumina to some extent. At the edge of the unreacted core, the silica concentration drops abruptly from a higher level to a lower level, suggesting that there are at least two kinds of silica with different stabilities inside the sample and thus with different reaction rates. The normalized weight percents of 72 wt% Al_2O_3 and 28 wt% SiO_2 at the inner edge of the transition layer corresponds to the mullite composition. The thickness of the inner or transition layer increases with total reaction time which is due to the lower reaction rate of mullite. At the outer edge of the transition layer the silica concentration drops to zero abruptly and the structure changes into α-alumina. This behavior is similar to that of a mullite sample and will be discussed later.

III. Reaction Between $CaO-Al_2O_3-SiO_2$ Glasses and Hydrogen Gas

1) Phase Separation and Crystallization

The phase diagram of the $CaO-Al_2O_3-SiO_2$ ternary system is shown in Fig. 23. It is important to note that there is a low temperature eutectic composition with a melting point of 1170°C. A liquid phase can be formed in this ternary system above 1200°C. There is also a stable miscibility gap between SiO_2 and CaO as shown in Fig. 24 which probably can be extended metastably to lower temperatures. Phase separation thus occurs more readily in this system than in the $Al_2O_3-SiO_2$ system. It was observed that the glasses with lime became opaque upon heating below 1000°C. The crystallization of $CaO-Al_2O_3-SiO_2$ glasses also occurs at a lower temperature. Figure 25 shows that strong x-ray diffraction peaks were observed in R glass after 10 hours of heating at 1200°C and a subsequent heating of 10 hours at 1300°C did not introduce significant

changes to the diffraction pattern although a small increase in bulk density was observed. It is apparent that crystallization in the CaO-Al_2O_3-SiO_2 sample was greatly reduced after 10 hours of heating at 1200°C. Mullite peaks were found as well as a very sharp, reproducible x-ray diffraction pattern whose peaks, although close to some of the known CaO-SiO_2 and CaO-Al_2O_3-SiO_2 phases, could not be identified. No cristobalite peaks were found, suggesting the inhibition of cristobalite formation by the addition of CaO to the Al_2O_3-SiO_2 binary compound. The addition of a small amount of lime to the alumino-silicate glass had a significant effect on the phase separation and crystallization, especially at temperatures below 1200°C.

2) Surface Morphology of Reacted Alumino-silicate Glasses

As calcia is a glass modifier, the viscosity of the CaO-Al_2O_3-SiO_2 glass is lower than that of the alumino-silicate glass. The Q glass (5 wt% CaO, 19 wt% Al_2O_3) showed deformation due to viscous flow at 1200°C. The reacted Q-glass at 1250°C gave a different surface morphology as shown in Fig. 26. By using Energy Dispersive x-ray analysis (EDAX), the surface was found to be composed only of alumina. The rod like alumina residue apparently came from the decomposed mullite which had previously grown out of the liquid phase. The pores surrounding the alumina residue resulted from the loss of the silica matrix. Figure 27 shows the reacted surface of S glass (5 wt% CaO, 38 wt% Al_2O_3). At 1500°C (1A, B, C of Fig. 27) the alumina residue agglomerate size is still smaller than that of Q glass at 1250°C (Fig. 25), indicating that the original mullite crystal size of the latter is larger. The shape of the residue is also different. The S glass has a much higher viscosity

than the Q glass. No deformation is apparent up to 1450°C. All of these differences are attributed to the amount of liquid phase formed. The additional alumina retards the formation of liquid phase.

In a few cases, bloating occurs in some of these low alumina and high lime glasses and thus deforms the sample. It is probably due to the expansion of trapped gasses (seeds) upon heating as the viscosity of the sample decreases.

3) Reaction with Hydrogen Gas

As most glasses with lime started to deform at temperatures below 1300°C, only S glass (5 wt% CaO, 38 wt% Al_2O_3) was used for the kinetic study. It was found that the S glass has a slightly lower reaction rate than the L glass in the temperature range 1200°C to 1350°C (Fig. 17), but a slightly higher rate above 1350°C. In general, the addition of lime does not have a significant effect on the reaction rate.

4) Concentration Profile of Reacted $CaO-Al_2O_3-SiO_2$ Glass

The cross-section of the reacted S glass is shown in Fig. 28. At the bottom of the photograph is the unreacted core (#6), above the core is the transition layer followed by an alumina layer (#1) at the top. Preliminary examination by EDAX shows concentration variations across the reaction zone (Fig. 29). In order to get a better quantitative description of the composition change, electron probe microanalysis was used. The profile obtained by a normal spot probe is shown in Fig. 30 and the profile without composition normalization, in Fig. 31. The curves for the alumino-silicate system (L Glass) are much smoother (Figs. 20 & 22). The fluctuations for the S glass apparently are due to the phase separation which is of a size comparable to that of the electron beam. Therefore, a

line scan parallel to the reaction front was performed and the profile thus obtained is shown in Fig. 31 (with normalization) and in Fig. 33 (without normalization). A much smoother profile curve was obtained. In Fig. 33, it can be seen that there are two layers: from left to right, the unreacted core, the transition layer and the alumina layer. The thickness of the transition layer or alumina layer varies from sample to sample and is a function of reaction time and temperature. The profile is basically similar to that for the alumino-silicate system (Figs. 20 & 22). However, in this case calcia is bonded to silica and therefore a new compound is present in the transition layer. The profiles of Figs. 32 and 33 indicate that calcia is not decreased in the transition layer but disappears together with the silica leaving an outer alumina layer.

As the calcia is not expected to react with hydrogen according to the thermodynamics data, it should be left behind as a residue. Its absence in the outer layer suggests that at some SiO_2/Al_2O_3 ratio calcia reacts with water vapor which is formed as a reaction product. At higher SiO_2/Al_2O_3 ratios calcia is stabilized by the structure. Further study is needed to ascertain the mechanism. The composition normalized profile obtained from a normally mounted S-glass sample (instead of vacuum mounted) is shown in Fig. 34. A comparison between Figs. 32 and 34 shows that a smearing of the sample occurred in its preparation since the profile is smoother in the latter. The general features of the profile, however, are the same.

5) Sintering of the Surface Layer

The addition of Al_2O_3 and CaO to the silica glass decreased the reaction rate, but did not stop the reaction. As the silica is etched away, alumina is left behind as a residue layer. However, the alumina

layer remains porous and does not halt the reaction. If this alumina residue could be sintered into a dense layer, it may protect the interior from further reaction. The as-reacted samples were heated at 1600°C for 4 hours. In the alumino-silicate system the sintered alumina layer cracked into pieces due to the differences in the expansion coefficients of the two layers which also caused poor adherence between the different layers. In the $CaO-Al_2O_3-SiO_2$ system homogenization and mullite formation occurred before the alumina sintered. Rod-like mullite grains were found growing out of the surface (Fig. 35). The EDAX picture confirms the mullite composition. The rod shaped mullite crystal also suggests the presence of a liquid phase which is as expected (Fig. 23). As the mullite is not completely corrosion resistant, this surface layer will not be able to protect the sample from further reaction.

IV. Reaction Between Mullite and Hydrogen Gas

Mullite is the only stable alumino-silicate compound (Fig. 14). The stoichiometric composition ($3Al_2O_3-2SiO_2$) is 72 wt% Al_2O_3 and 28 wt% SiO_2. The corrosion behavior of mullite and the glassy phase is of special interest. Mullite samples of a composition of about 73 wt% Al_2O_3 were used. No variations in composition or preparation processing were tried to evaluate the effect on the reaction rate since preliminary tests indicated that mullite did react with hydrogen gas. It was thus not expected that a small change in the composition would affect the reaction rate significantly.

As-sintered mullite without any other treatment was used for the corrosion test. The surface morphologies of the as-sintered and reacted samples are shown in Fig. 36. The reacted sample was polished to 0.25

micron before reaction. No evidence is observed in Fig. 36 that the grain boundaries are etched at a higher rate. When the grain boundaries react at a higher rate than the grains themself, the grains will stand out as in the reaction with hydrofluoric acid solution (Fig. 37). Figure 36 shows that the grains react with hydrogen gas. After decomposition and loss of silica, alumina is left behind as α-alumina crystals. The profile of the reacted mullite sample is shown in Fig. 38 (composition normalized) and Fig. 39 (without normalization). As the silica concentration is negligibly small, the composition normalized curve conceals the actual fluctuation in the alumina layer which is shown in Fig. 39. This fluctuation undoubtedly is due to the porous nature of the layer. It can be seen in Fig. 38 that there is no transition layer in the reacted mullite sample. The silica concentration drops to zero within a few microns of the unreacted core. The alumina data without normalization show a slight increase in alumina with distance from the reaction interface indicating a slight contraction. This contraction can be associated with the occurrence of some sintering.

Photographs of a polished cross-section of the reacted mullite are shown in Fig. 40. Figure 40A shows the overall cross-section. In the higher magnification photos the smoother surface on the left is the unreacted mullite and the porous surface on the right is alumina left by the decomposition of mullite. At the highest magnification (Fig. 40D), the reaction front is flat within a few microns (Fig. 40D) suggesting that the reaction rate at the grain boundaries is not significantly faster than in the grain. This behavior justifies the decision that no variation in composition was necessary for the hydrogen corrosion study. Cracks are seen to go through the reaction interface. In the reacted alumino-

silicate glass sample, on the other hand, cracks follow the interface. Figure 41A shows two pieces of reacted L glass (30 wt% Al_2O_3). The unreacted core, the transition layer and the alumina layer are separated in the right sample (arrows). The adherence seems to be better on the left sample. However, magnified photos (Fig. 41 B, C and D) of the portion inside the square in Fig. 41 A reveal cracks between unreacted core and the transition layer as indicated by the bright strips on the sample due to the charging effect. The alumina layer was not visible in these photos (Fig. 41 B, C and D). The poor adherence of the unreacted core and the transition layer is due to the mismatch in the expansion coefficient. In the mullite case, the interfacial bonding is strong enough to withstand the stress caused by the difference in expansion coefficients, resulting in good adherence.

The reaction rates of the mullite with hydrogen gas at different temperatures were obtained by plotting the weight loss per unit surface area vs. reaction time (Fig. 42). The slope of the curve obtained by least squares fitting gives the reaction rate at the indicated temperature. The activation energy can be obtained by plotting the logarithm of these reaction rates versus the reciprocal of temperature (Fig. 17). It is interesting to note that the apparent activation energies for L glass (70 wt% Al_2O_3) and mullite are close, 86 and 93 Kcal/mole. However, as their concentration profiles are so different, no apparent correlation can be found.

Mullite appears to be a potential candidate for a corrosion resistant material as it can withstand the high temperature necessary for sintering the porous surface layer and it has good interfacial bonding between the unreacted core and the surface reaction product layer.

Sintering of the alumina layer on the reacted mullite sample was attempted. The sintered samples at 1550°C, 1600°C, 1650°C and 1700°C are shown in Fig. 43. From the photos, it can be seen that the porous alumina layer was sintered at 1600°C. Unfortunately, cracks occur in the alumina layer. It is not clear whether they were formed during sintering or cooling. A picture of a crack is shown in Fig. 44. If cracking occurs during the cooling process, then combined reaction and sintering without cooling could possibly still be used to make a corrosion resistant material.

V. Reaction Between Silicate Glasses and HF Acid Solution

1) Surface Morphology

As mentioned previously, the as-cut glass has a rough surface. This surface layer which is full of microcracks has a much larger surface area and hence a higher reaction rate. A large experimental fluctuation for specimens prepared this way is thus inevitable. Several methods, including annealing, polishing and chemical treatments, were tried to remove this rough surface layer and thus reduce the empirical fluctuation. It was found that the simplest way to remove it was to treat the glass with HF acid solution which results in the reacted glass sample having a uniform surface morphology. The reacted glass has a similar morphology after 2, 4 and 6 hours of reaction with HF acid solution as shown in Fig. 46. The depth of the cusps can be estimated by taking two pictures at different tilting angles and using a stereoscope. In Fig. 47, the depth of the cusps was estimated as 10 to 20 microns and the diameter as 50 to 100 microns. The true surface area can be calculated from these figures and is only 4% higher than the projected flat surface area. Furthermore, because of the invariance of the surface morphology, the surface area

remains fairly constant. The contrast between glasses reacted with HF acid solution and hydrogen gas is very great and is due to the different reaction mechanisms. The latter reaction can not be diffusion controlled as the existent holes could grow deeper and deeper (Fig. 8).

2. Diffusion Controlled Reaction Rate

On the other hand, the surface morphology of the silicate glasses after reaction with HF acid solution suggests that the reaction is diffusion controlled. For a diffusion controlled mechanism, the formation of deep holes is inhibited. As a hole grows deeper, the diffusion distance between the bottom of the hole and the constant concentration front will increase. Therefore, the concentration gradient decreases, and the diffusion and the reaction rates decrease.

The reaction rate at the ridge will be higher than that at the bottom and the hole can not grow deeper. Therefore, a fairly constant surface morphology will be maintained as is the case for the reaction between silicate glass and HF acid solution. There are other pieces of evidence for the rate being diffusion controlled. It was found that without agitation the reaction rate at the bottom of the container was lower due to the precipitation of a silica gel formed during the reaction. A platinum wire hanger was used to prevent the samples from being surrounded by the silica gel. Also, a shaker was used to provide agitation to keep the product away from the surface of the sample. Different oscillation speeds between 20 cycles to 200 cycles per minute were used to reveal the relationship between the reaction rate and agitation. It was found that the reaction rate monotonically increased with oscillation speed without leveling off at the maximum speed of the shaker. This

behavior was again in strong contrast with the reaction between silica glass and hydrogen gas (Fig. 7).

The effect of concentration of the HF solution was first studied at a fixed oscillation speed of 120 cycles per minute. In each experiment, a small piece of silica glass and adequate HF acid solution were used so that the HF concentration remained practically unchanged. The reaction time was also limited so that the shrinkage of the glass sample could be neglected. The observed relationship is shown in Fig. 48. The reaction rate was found to be linear with HF concentration when the total HF concentration was low. In the more concentrated solutions, the reaction rate was greatly accelerated. This increase in the reaction rate at higher concentrations is explained on the basis of the formation of considerably more active bifluoride ions.[14]

The temperature dependence of the reaction rate remained the same (Fig. 49). A unique activation energy of 5.3 Kcal/mole was observed with HF acid solution concentrations ranging from 3 to 24 M. This low value of activation energy also suggests a diffusion controlled mechanism. The same activation energy combined with an accelerated rate in the more concentrated solutions can be explained by the more active bifluoride ion causing a higher equilibrium product concentration while diffusion remains the slowest step.

A possible reaction mechanism is suggested as follows. It has been reported[15] that a silica gel film of thickness 2 to 4 micron is formed on a silica glass surface in the acid. Further reaction of HF and this silica gel is responsible for the weight loss of silica. Therefore, the reaction is assumed to consist of two stages

(i) Protonizing the surface

$$SiO_3^{-2} + 2H^+ \rightleftharpoons H_2SiO_3$$

(ii) Reaction of protonized surface with HF

$$H_2SiO_3 + 4HF \rightleftharpoons SiF_4 + 3H_2O$$

A possible mechanism for the first stage is the attachment of the proton to a non-bridging oxygen. The next step is the attachment of nuclephilic groups (F^-) on a coordination basis, which causes the reconstruction of electron orbitals of Si-O-H bonds. The results of such a reconstruction are the weakening of the silicon oxygen bond and the release of a silico-hydrofluoric group into the solution which later dissociates to give a total or net reaction of $SiO_2 + 4HF \rightarrow SiF_4 + 2H_2O$

4. Reactions Between Silicate Glasses and HF Acid Solution

Eight different kinds of glasses were used (Fig. 4). The densities of these glasses (in gm/cm^3) are listed below

K glass = 2.31	L glass = 2.42	
N glass = 2.30	O glass = 2.38	P glass = 2.61
Q glass = 2.32	R glass = 2.38	S glass = 2.52

All the reaction rates were measured using a 6M hydrofluoric acid solution and at a fixed oscillation speed of 120 cycles per minute. Under the same reaction conditions, the observed reaction rate can be used to evaluate the comparative corrosion resistance of each material against HF acid solution attack.

Generally speaking, the addition of either Al_2O_3 or CaO to the silica does not increase the corrosion resistance against HF acid solution as they do against hydrogen gas. On the contrary, the reaction rate is increased. With alumina alone (K glass: 20 wt% Al_2O_3, and L glass: 30 wt% Al_2O_3), the silicate glasses have only slightly higher reaction rates (Fig. 50). As mentioned before, the as-quenched alumino-silicate glasses are phase separated and contain a certain amount of mullite. The reported corrosion resistance series[9] against HF acid solution attack is : Mullite >> silica glass > alumino-silicate glass. As the mullite formed in the quenching process is very small (less than 0.1 micron) and separated, no continuous structure can be formed. When the silica glass matrix is etched away, the mullite or alumina will just slough off and therefore increase the observed reaction rate.

In the $CaO-Al_2O_3-SiO_2$ ternary glasses, the reaction rates were much higher as shown in Fig. 51. Glasses N, O and P all contain 2 wt% of CaO. Calcium oxide is very reactive towards acids and increases the reaction rate in an acid. The difference in the reaction rates between these glasses with different alumina contents is larger than those glasses without lime (Figs. 51 and 50). This can be explained as the addition of lime allows tetrahedral coordination of most of the aluminum ions and reduces the tendency toward phase separation during formation of the glass. Since the high alumina glass has the highest reaction rate, a combination of lime and alumina decreases the corrosion resistance to HF acid solution.

For glasses containing about the same amount of alumina, the reaction rate increases with increasing calcium oxide content (Fig. 52). This may be attributed partly to the stabilization of more aluminum ions so as to

form more alumina-rich silicate glass, and partly to the fact that lime is a glass modifier and reacts with the acid solution much more readily. The reaction rate of P glass (2 wt% CaO, 39 wt% Al_2O_3), is much higher than expected. P glass also has the highest density among the glasses. This higher reaction rate may be due to its higher density. As a comparison alumina does not react with HF acid solution and the rate of reaction of mullite with HF acid solution is two orders lower than the glasses.

The phase separation shows no effect on the surface morphology of the reacted silicate glasses. The surface morphology looks exactly the same as that of the silica glass (Fig. 46). In all cases, no residue was found to remain on the sample surface. Apparently, the reaction of silicate glasses with HF acid solution is different from that with hydrogen gas. There is no analogy and empirical relative corrosion resistance between these two different reaction patterns.

SUMMARY AND CONCLUSIONS

The corrosion of silicate materials by hydrogen gas and HF acid solution was investigated by the gravimetric method. The reaction of silicate glasses with HF acid solution is found to be diffusion controlled as evidenced by the invariance of the reacted glass surface morphology, the monotonously increasing reaction rate with increased agitation and typical low activation energies (<10 Kcal/mole). The corrosion resistance to the HF acid solution decreases with the addition of either alumina or lime. This decrease in corrosion resistance is due to the increased phase separation in the silicate glasses. A reaction mechanism for the silica glass and HF acid solution was postulated. The reaction is assumed to consist of two steps: hydration of silica glass surface and reaction between hydrated silica and HF.

In the reaction with the hydrogen gas, the rate is kinetically controlled. A strong contrast is found between these two reaction patterns (with hydrogen gas and HF acid solution). No empirical resistivity correlation was found.

The loss of pure silica glass in the hydrogen atmosphere in the temperature range of 1200°C to 1400°C is due to a reaction with hydrogen gas and not a decomposition as a result of the low partial pressure of oxygen. The devitrification of silica glass in the hydrogen gas is due to a reaction with the sodium vapor originating from sodium oxide in the alumina tube. A drilling phenomenon was observed on the reacted silica glass. Redeposition of cristobalite on silica glass was also observed. Both phenomena are attributed to the temperature profile in the glass due to its transparency. The reaction mechanism of silica glass with hydrogen

gas was studied. The desorption of reaction product was deduced as probably the slowest step.

The addition of alumina and/or calcia to the silica glass decreases the reaction rate with the hydrogen gas. This effect can be explained on the basis of the formation of tetrahedrally bonded aluminum ions and thus the increased activity of the material. The silicate glasses are all phase separated and not homogeneous materials. The reaction rate is different for different phases. As the mullite had the slowest reaction rate, a transition layer was formed. An alumina residue was left behind after reaction with hydrogen gas in all cases. Electron microprobe analysis indicated that the glasses had an additional transition layer. The probe data further showed that the residue layers are porous and therefore do not stop the reaction. The weight loss per unit area is linear with reaction time, indicating that the surface residue layer is not a barrier to the mass transport and that the reaction is kinetically controlled.

Apparent activation energies of ~90 Kcal/mole are obtained for alumino silicate materials. The activation energy for the glass with the addition of 5 wt% CaO is ~68 Kcal/mole. The reactions of the glasses are complex due to the presence of intermediate layer (silicate glasses) or the surface roughening and redeposition effects (silica glass). No correlation between the apparent activation energies is feasible.

Efforts were made to sinter the porous alumina layer into a dense, protective layer. In the alumino silicate glasses, the sintered alumina layer cracked into pieces as a result of mismatch in the expansion coefficients. For the silicate glasses with lime, homogenization and

mullitization occurred before alumina sintered. Mullite is the material with the most potential. It can withstand the high temperature necessary for the sintering of the surface residue layer and good adherence exists between the unreacted mullite and the surface layer.

ACKNOWLEDGMENTS

I wish to express my sincere appreciation to Professor Joseph A. Pask for his continuous guidance and encouragement in this research work. He gives excellent advice and provides every opportunity to inspire his students toward independent thinking. His kindness and consideration has made my graduate study the most satisfying experience. I also want to thank Professor A. W. Searcy for many helpful discussions.

Special thanks are expressed to Sylvia Johnson for editing and Gay Brazil for typing the thesis. Acknowledgments are extended to my colleagues and friends, especially Robert Langston, David Wang, Vic Draper, Donald Huang and Mike Sacks for many enlightening discussions.

Further thanks are extended to the support staff, especially Richard Lindberg, Glenn Baum and Gloria Pelatowski for their assistance.

Finally, I would like to thank my wife, Christina Tso, for her constant encouragement and support.

This work was supported by the National Science Foundation and by the Division of Materials Sciences, Office of Basic Energy Sciences, U.S. Department of Energy under contract No. W-7405-Eng-48.

REFERENCES

1. Mark W. Zemansky, Heat and Thermodynamics, fifth edition, P. 612, McGraw-Hill Book Company.

2. A. S. Friedmann and L. Haar, J. Chem. Phys. 22, 2051 (1949); "Selected Values of Chemical Thermodynamic Properties," National Bureau of Standards, Circular 500.

3. R. B. Bird, W. E. Stewart and E. N. Lightfoot, Transport Phenomena, Part III, John Wiley & Sons, Inc., 1960.

   J. R. Welty, C. E. Wicks and R. E. Wilson, Fundamentals of Momentum, Heat and Mass Transfer, Chapter 24-30; John Wiley and Sons, Inc., 1969.

4. H. Schlichting, Boundary Layer Theory, Pergamon Press, New York (1955).

5. Aveyard and Haydon, An Introduction to the Principles of Surface Chemistry, P. 155, Cambridge Chemistry Texts, 1973.

6. C. Kittel, Introduction to Solid State Physics, 4th edition, P. 224, John Wiley and Sons, Inc., 1971.

7. W. D. Kingery, "Heat Conductivity Process in Glass," J. Am. Ceram. Soc., 44, No. 7, P. 302-304 (1961).

8. R. Gordon, "A Review of Radiant Heat Transfer in Glass," J. Am. Ceram. Soc., Vol. 44, No. 7, P. 305-312 (1961).

9. J. F. MacDowell and G. H. Beall, "Immiscibility and Crystallization in Al_2O_3-SiO_2 Glasses," J. Am. Ceram. Soc., Vol. 52, No. 1, P. 17-25 (1969).

10. W. D. Kingery, H. K. Bowen and D. R. Uhlmann, Introduction to Ceramics, 2nd edition, P. 350, John Wiley and Sons, Inc. 1976.

11. R. F. Davis, I. A. Aksay and J. A. Pask, "Decomposition of Mullite," J. Am. Ceram. Soc., Vol. 44, No. 2, 1972.

12. K. Schwerdtfeger, "The Rate of Silica Reduction in Reducing Gases at 1500°C," Transactions of the Metallurgical Soc. of AIME, Vol. 236, P. 1152-1156, August 1966.

13. V. Ya Darydov, A. V. Kiselev and S. A. Kiselev, "Infrared Spectroscopy of the Surface and Intraskeletal Hydroxyl Group of Silica," Kolloidn. Zh. (Russ) 41(2), 227-32, 1979.

14. W. G. Palmer, "The Action of Aqueous Hydrofluoric Acid on Silica," J. of Chemical Society, Part 2, P. 1657-1665, 1930.

J. S. Judge, "A Study of the Dissolution of SiO_2 in Acidic Fluoride Solutions," J. of the Electrochemical Soc., P. 1772-1775, 1971.

15. A. I. Avgnstinnik, et al., Industrial Laboratory (Russ), Vol. 2 P. 192 (1973).

FIGURE CAPTIONS

Fig. 1. Schematic of the hydrogen furnace.

Fig. 2. Cross-sectional schematic of the furnace tube.

Fig. 3. Temperature profile inside the furnace tube.

Fig. 4. Silicate glass compositions.

Fig. 5. Microstructures of the mullite sample used in this study. The sample was polished to 0.25 micron and etched with 30M HF acid solution for 10 minutes.

Fig. 6. Calibration curve for the hydrogen gas flow rate.

Fig. 7. Reaction rate between silica and hydrogen gas versus the flow rate of hydrogen gas.

Fig. 8. Surface morphology of silica glass after reaction with hydrogen gas at 1300°C. Pictures A and F show how the surface morphology varies with increasing reaction time.

Fig. 9. Deposition of cristobalite on the surface of silica glass.

Fig. 10. Weight loss of pure silica glass per unit area versus reaction time.

Fig. 11. Temperature dependence of the total reaction rate for pure silica glass.

Fig. 12. Pressure dependence of the total reaction rate for pure silica glass. Dilution with helium and argon have different effects.

Fig. 13. Schematic of the actual furnace tube system.

Fig. 14. Phase diagram of the alumina-silica system.

Fig. 15. X-ray diffraction curves for L glass (30 wt% Al_2O_3, 70 wt% SiO_2) showing crystallization after heat treatment.

Fig. 16. Surface morphology of L glass after reaction with hydrogen gas.

Fig. 17. Temperature dependence of total reaction rate of L glass (30 wt% Al_2O_3, 70 wt% SiO_2), S glass (5 wt% CaO, 38 wt% Al_2O_3 and 57 wt% SiO_2) and mullite (73 wt% Al_2O_3, 27 wt% SiO_2). The activation energies for mullite, L glass and S glass are 92.5, 85.7 and 67.8 Kcal/mole, respectively.

Fig. 18. Weight loss per unit surface area versus time at 1400°C for pure silica glass, L glass, S glass and mullite. The curve is linear with time. The surface residue layer does not decrease reaction rate indicating kinetically controlled rate.

Fig. 19. Structures of alumino silicate compound with aluminum ion bonded tetrahedrally.

Fig. 20. Normalized concentration profile for L glass (30 wt% Al_2O_3, 70 wt% SiO_2) after reaction with hydrogen gas.

Fig. 21. Density profile for L glass (provided by probe analysis).

Fig. 22. Concentration profile of L glass without normalization. The low readings around 110 micron are the result of a hole in the sample.

Fig. 23. Phase diagram of $CaO-Al_2O_3-SiO_2$ ternary system.

Fig. 24. Phase diagram of $CaO-SiO_2$ system showing the immisibility gap.

Fig. 25. X-ray diffraction curves for R glass (4.8 wt% CaO, 28.6 wt% Al_2O_3, 66.6 wt% SiO_2) showing crystallization after heat treatments.

Fig. 26. Surface morphology of Q glass (5 wt% CaO, 19 wt% Al_2O_3, 76 wt% SiO_2) after reaction with hydrogen gas at 1250°C.

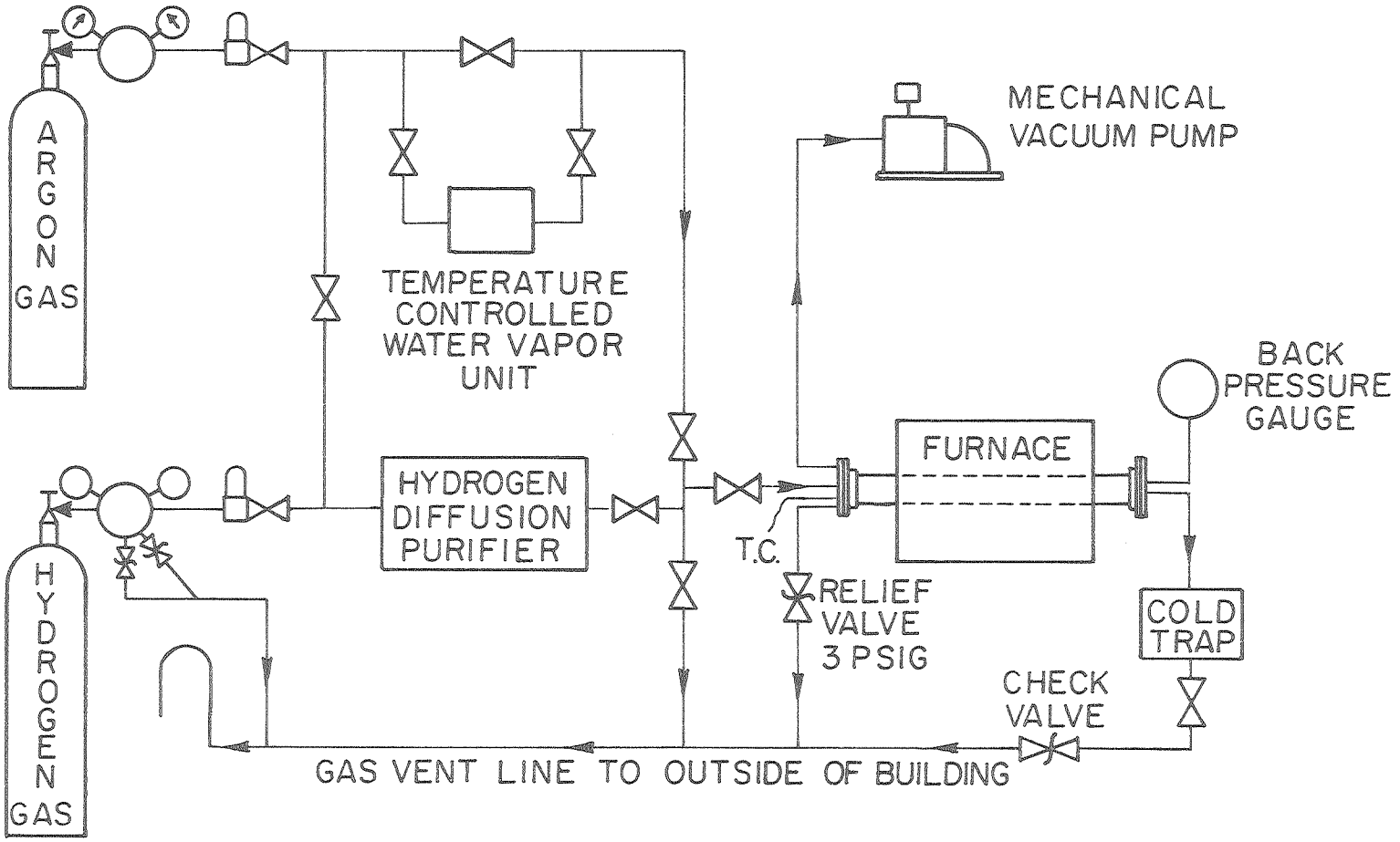
ARGON GAS
HYDROGEN GAS
TEMPERATURE CONTROLLED WATER VAPOR UNIT
HYDROGEN DIFFUSION PURIFIER
MECHANICAL VACUUM PUMP
BACK PRESSURE GAUGE
FURNACE
T.C.
RELIEF VALVE 3 PSIG
COLD TRAP
CHECK VALVE
GAS VENT LINE TO OUTSIDE OF BUILDING
XBL777-5872

Fig. 1

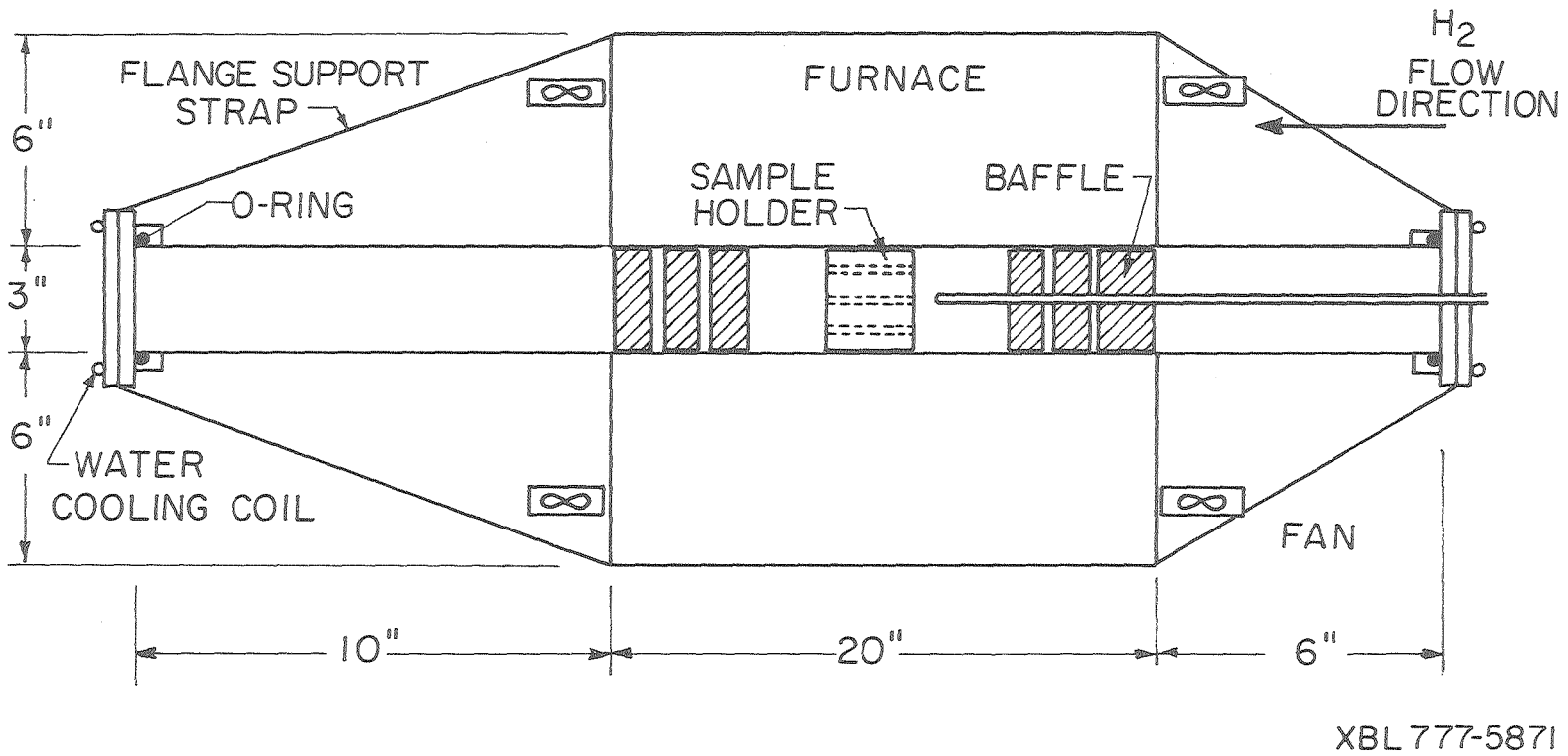
FLANGE SUPPORT STRAP
FURNACE
H_2 FLOW DIRECTION
6"
O-RING
SAMPLE HOLDER
BAFFLE
3"
6"
WATER COOLING COIL
FAN
10"
20"
6"
XBL 777-5871

Fig. 2

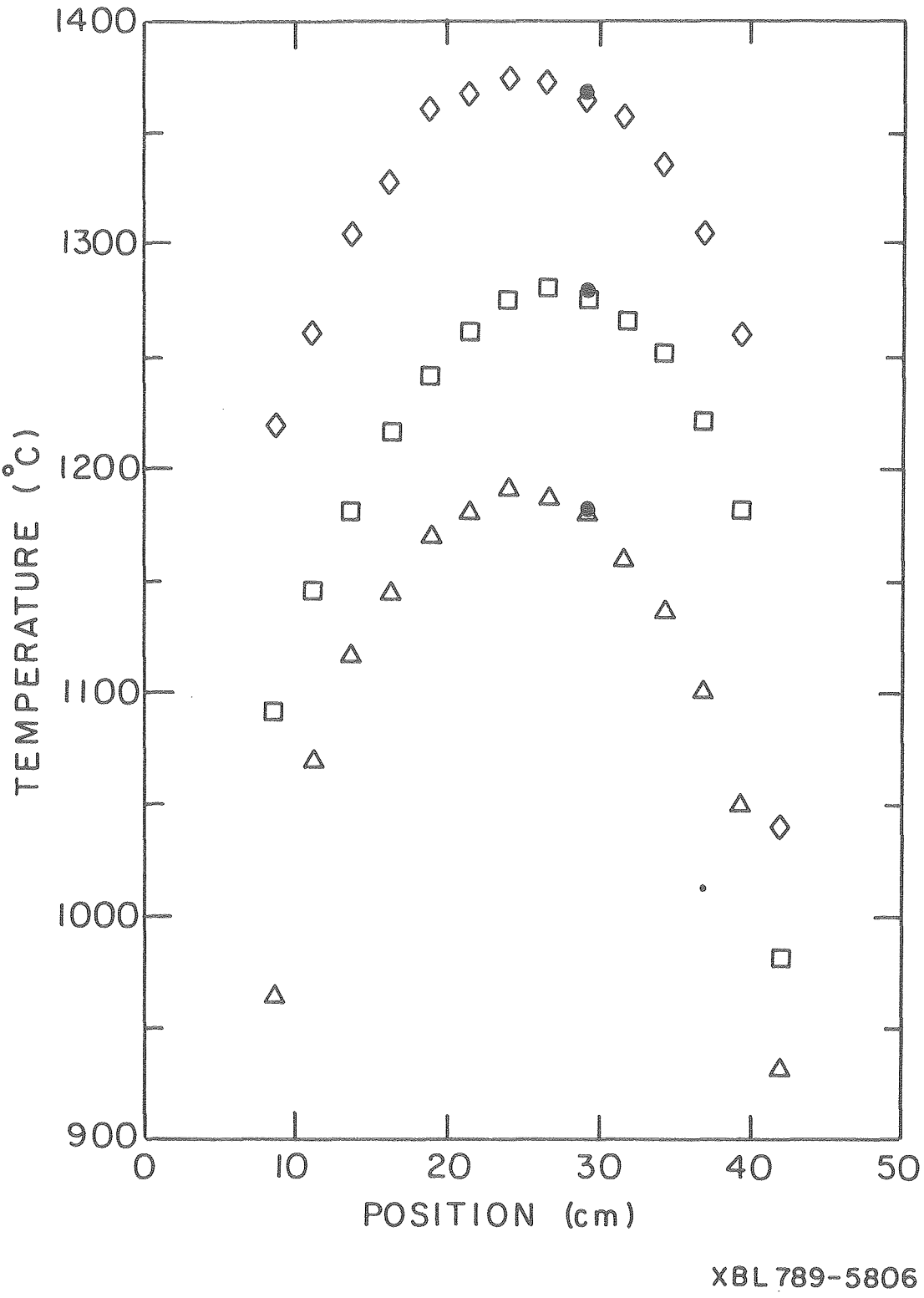
1400
1300
1200
1100
1000
900
TEMPERATURE (°C)
0
10
20
30
40
50
POSITION (cm)
XBL 789-5806

Fig. 3

	[WT. RATIO]			[MOLAR PERCENT]		
	SiO_2	Al_2O_3	CaO	SiO_2	Al_2O_3	CaO
SILICA GLASS	100	0	0	100	0	0
GLASS K	80	20	0	87.2	12.8	0
GLASS L	70	30	0	79.8	20.2	0
GLASS N	80	20	2	85.2	12.5	2.3
GLASS O	70	30	2	77.9	19.7	2.4
GLASS P	60	40	2	70.0	27.5	2.5
GLASS Q	80	20	5	82.4	12.1	5.5
GLASS R	70	30	5	75.3	19.0	5.7
GLASS S	60	40	5	67.5	26.5	6.0

Fig. 4

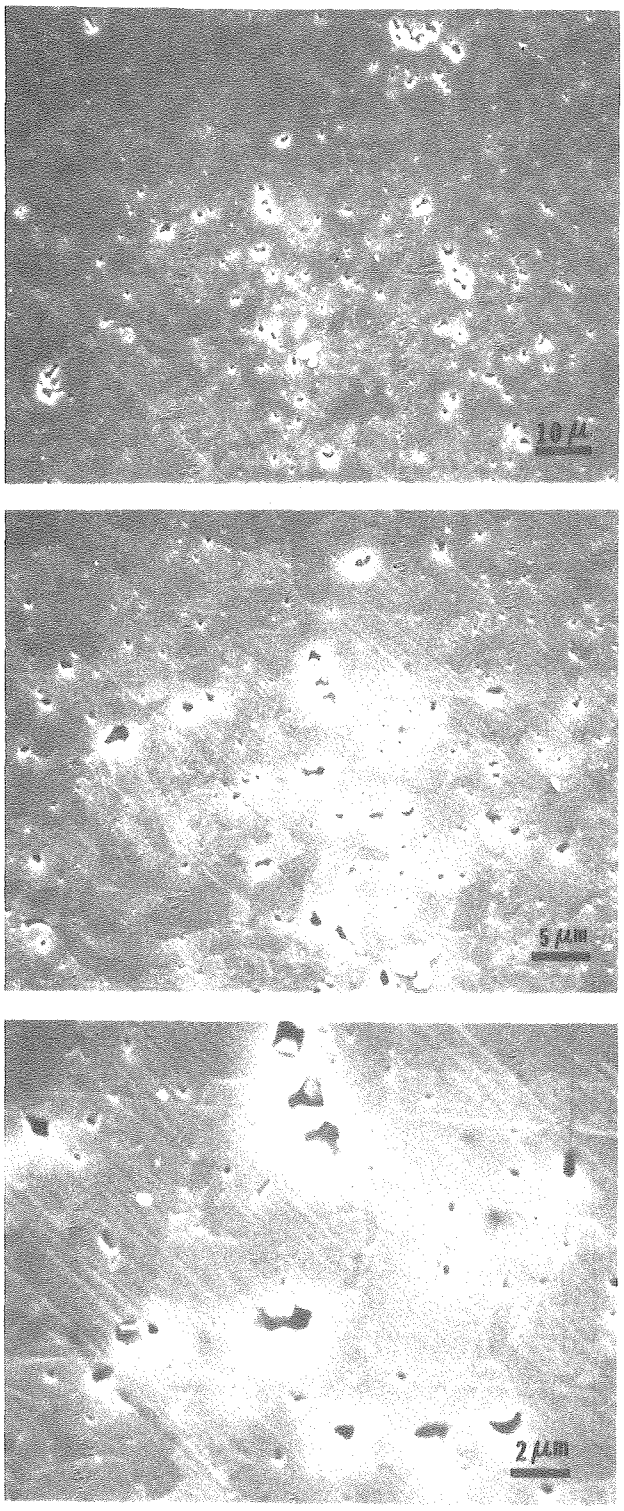

XBB799-11465

Fig. 5

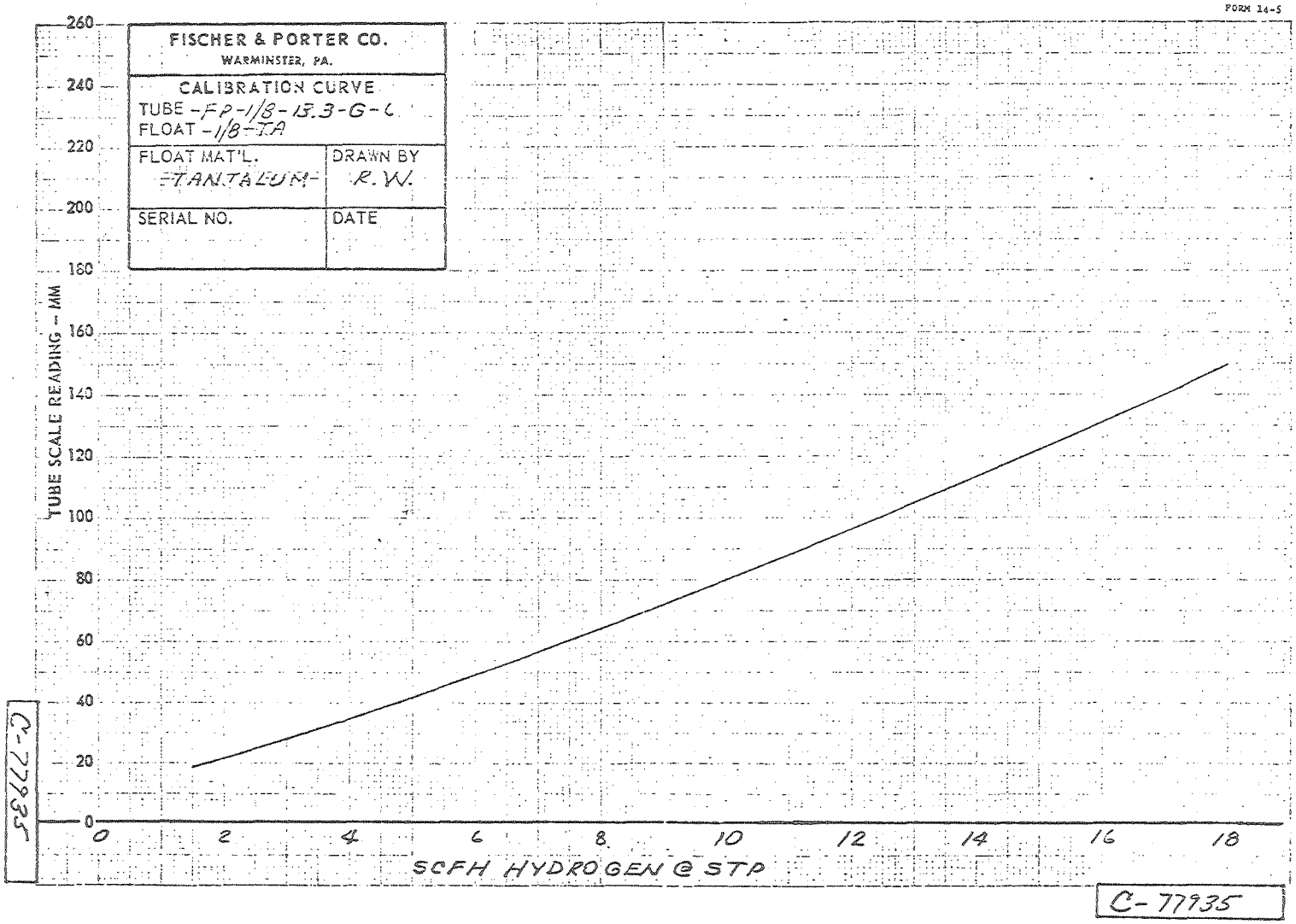
FORM 14-5
FISCHER & PORTER CO.
WARMINSTER, PA.
CALIBRATION CURVE
TUBE - FP-1/8-15.3-G-6
FLOAT - 1/8-TA
FLOAT MAT'L. - TANTALUM -
DRAWN BY - R.W.
SERIAL NO.
DATE
TUBE SCALE READING - MM
260
240
220
200
180
160
140
120
100
80
60
40
20
0
0
2
4
6
8
10
12
14
16
18
SCFH HYDROGEN @ STP
C-77935
C-77935

Fig. 6

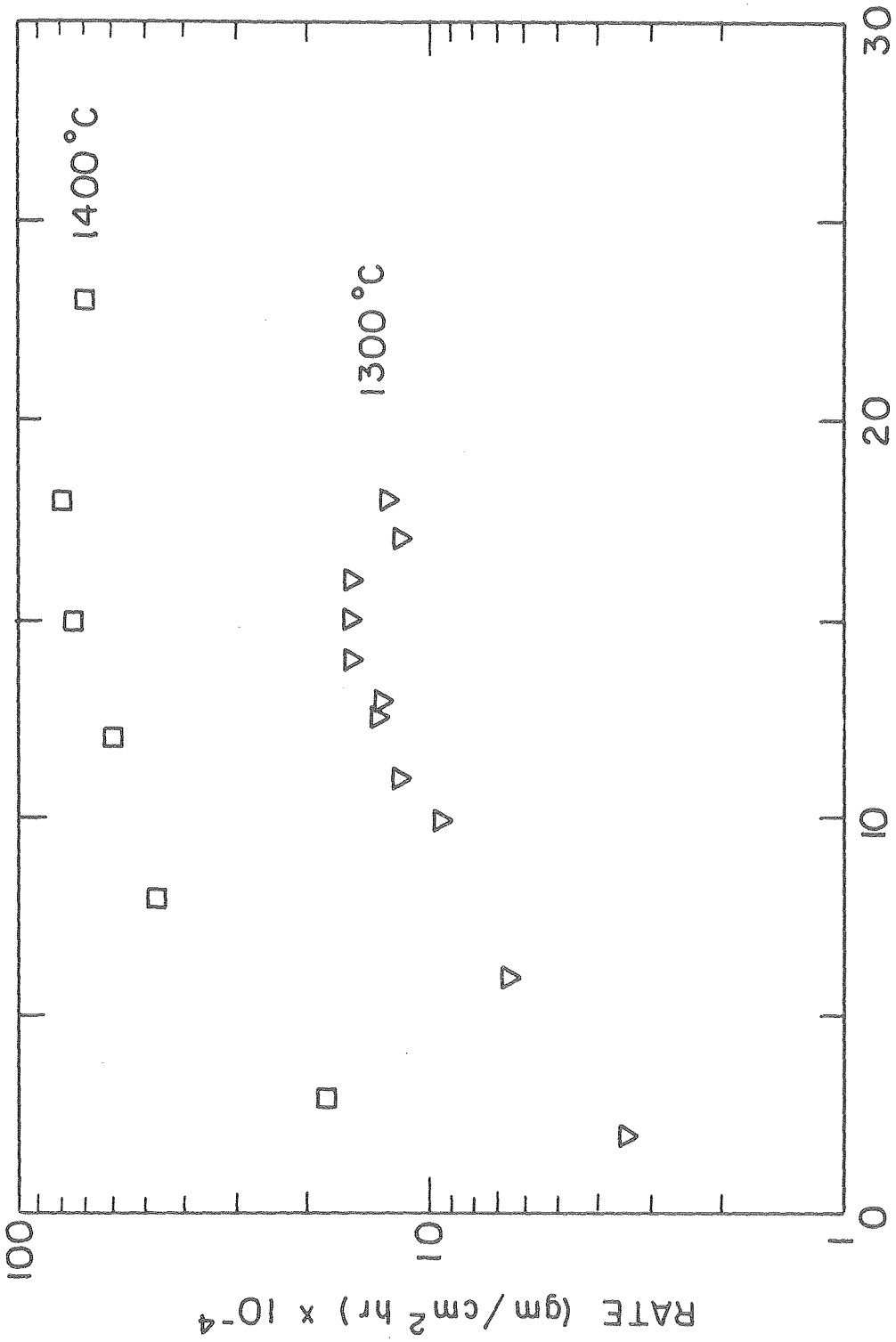

XBL 789-5807

Fig. 7

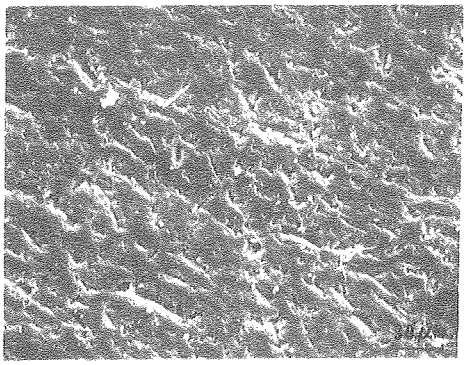

A

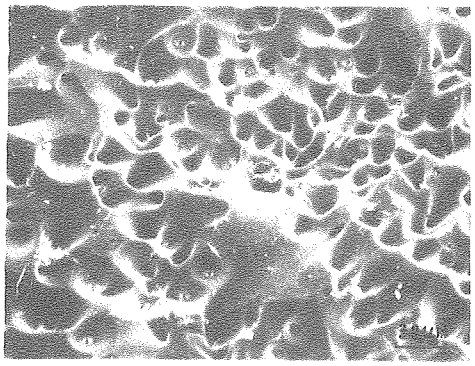

D

B

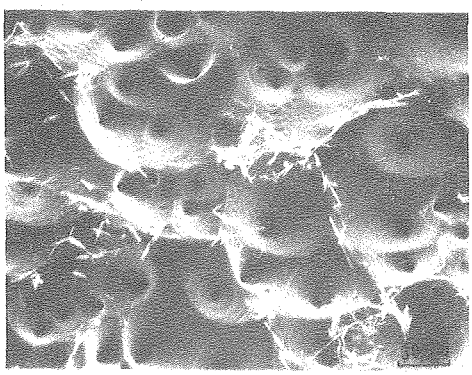

E

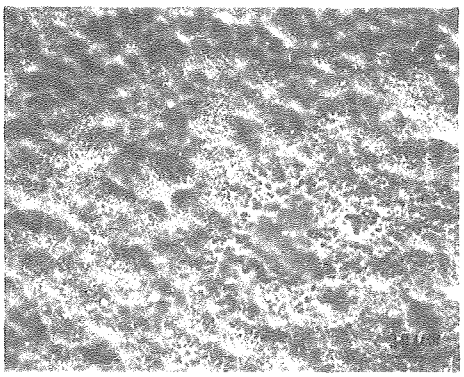

C

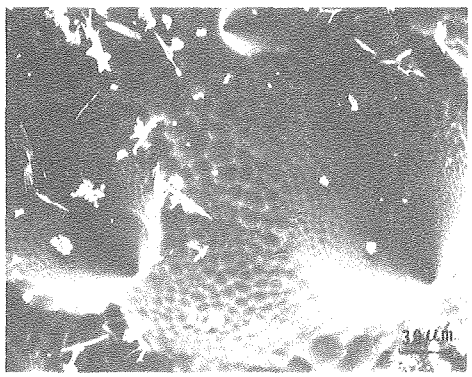

F

XBB780-14504

Fig. 8

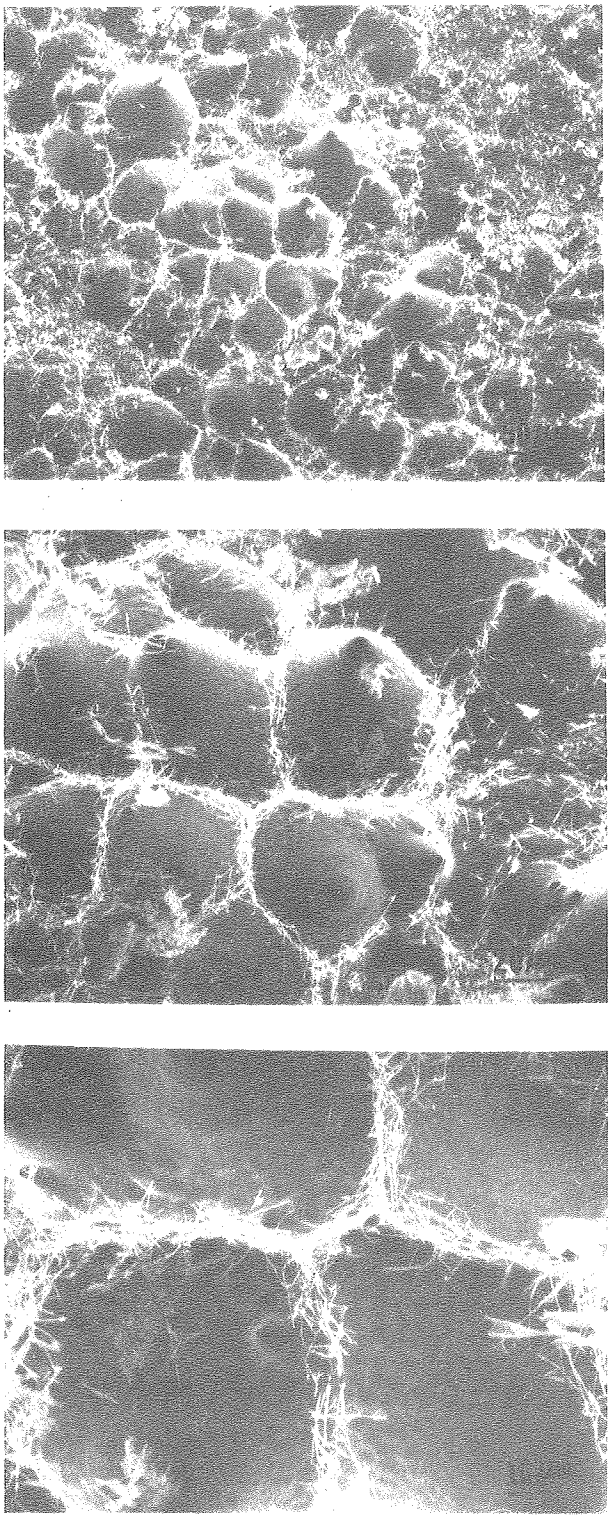

XBB780-14503

Fig. 9

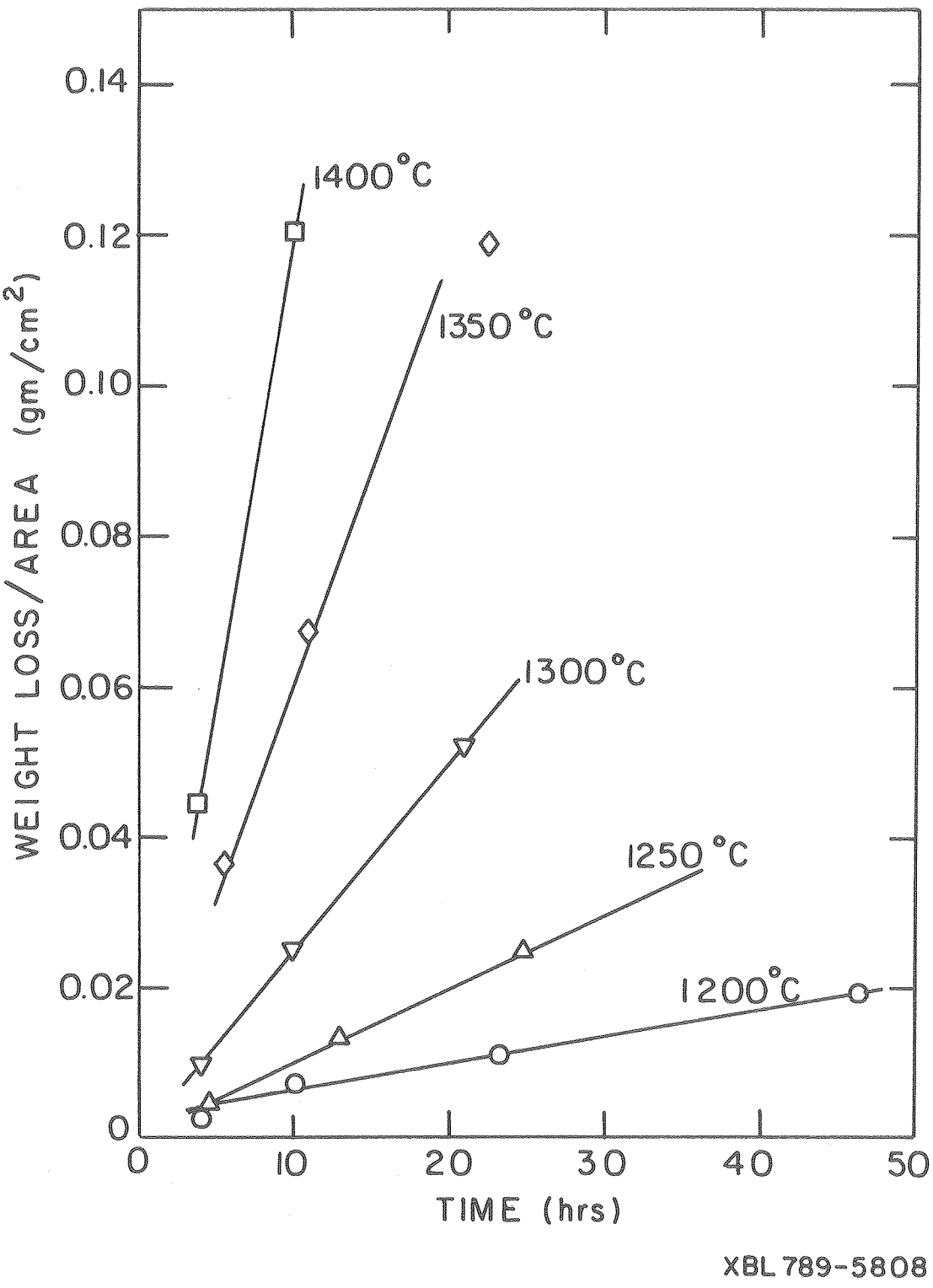
0.14
0.12
0.10
0.08
0.06
0.04
0.02
0
WEIGHT LOSS/AREA (gm/cm²)
1400°C
1350°C
1300°C
1250°C
1200°C
0
10
20
30
40
50
TIME (hrs)
XBL 789-5808

Fig. 10

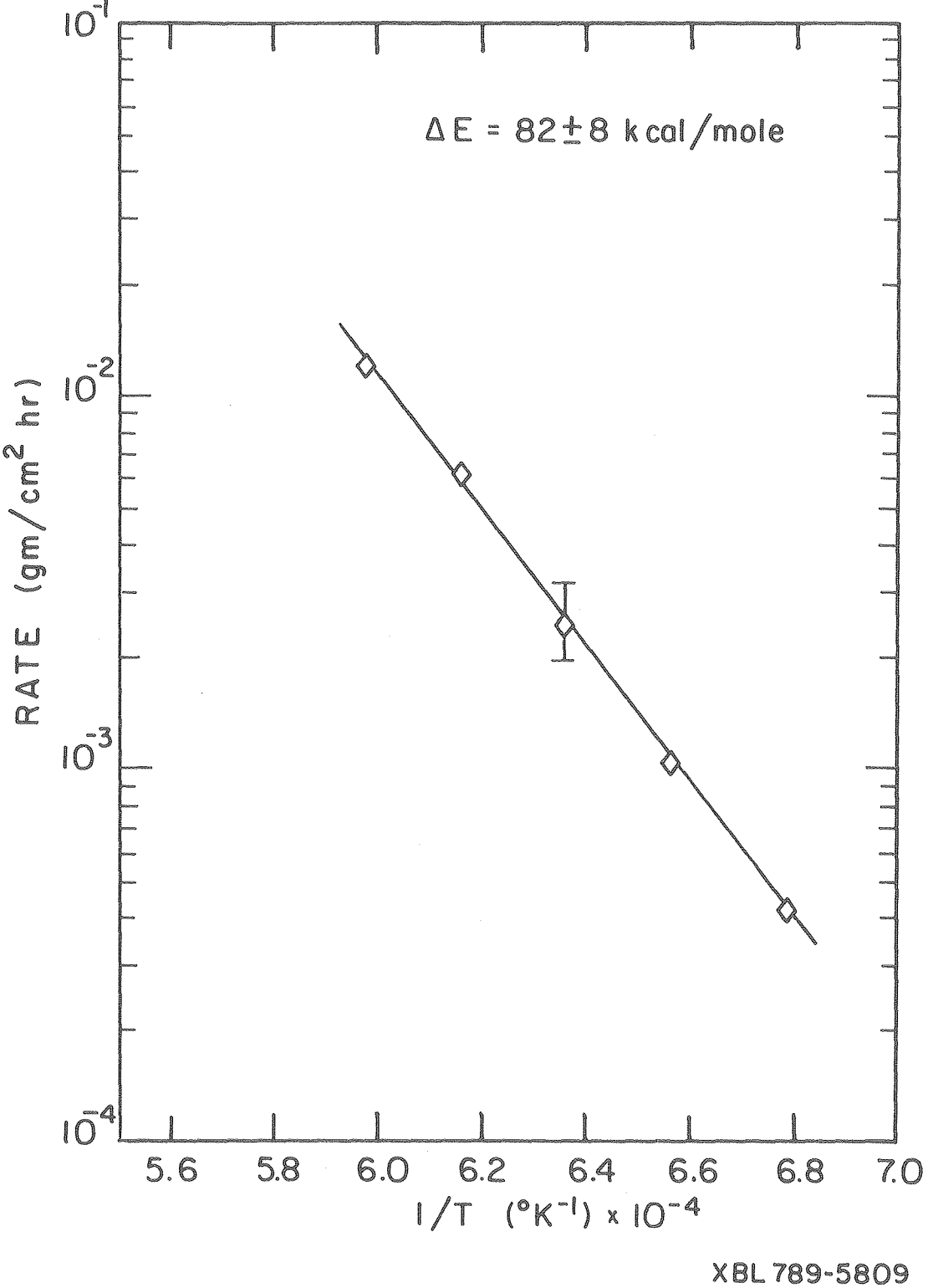
ΔE = 82 ± 8 kcal/mole
RATE (gm/cm² hr)
10⁻¹
10⁻²
10⁻³
10⁻⁴
5.6
5.8
6.0
6.2
6.4
6.6
6.8
7.0
1/T (°K⁻¹) x 10⁻⁴
XBL 789-5809

Fig. 11

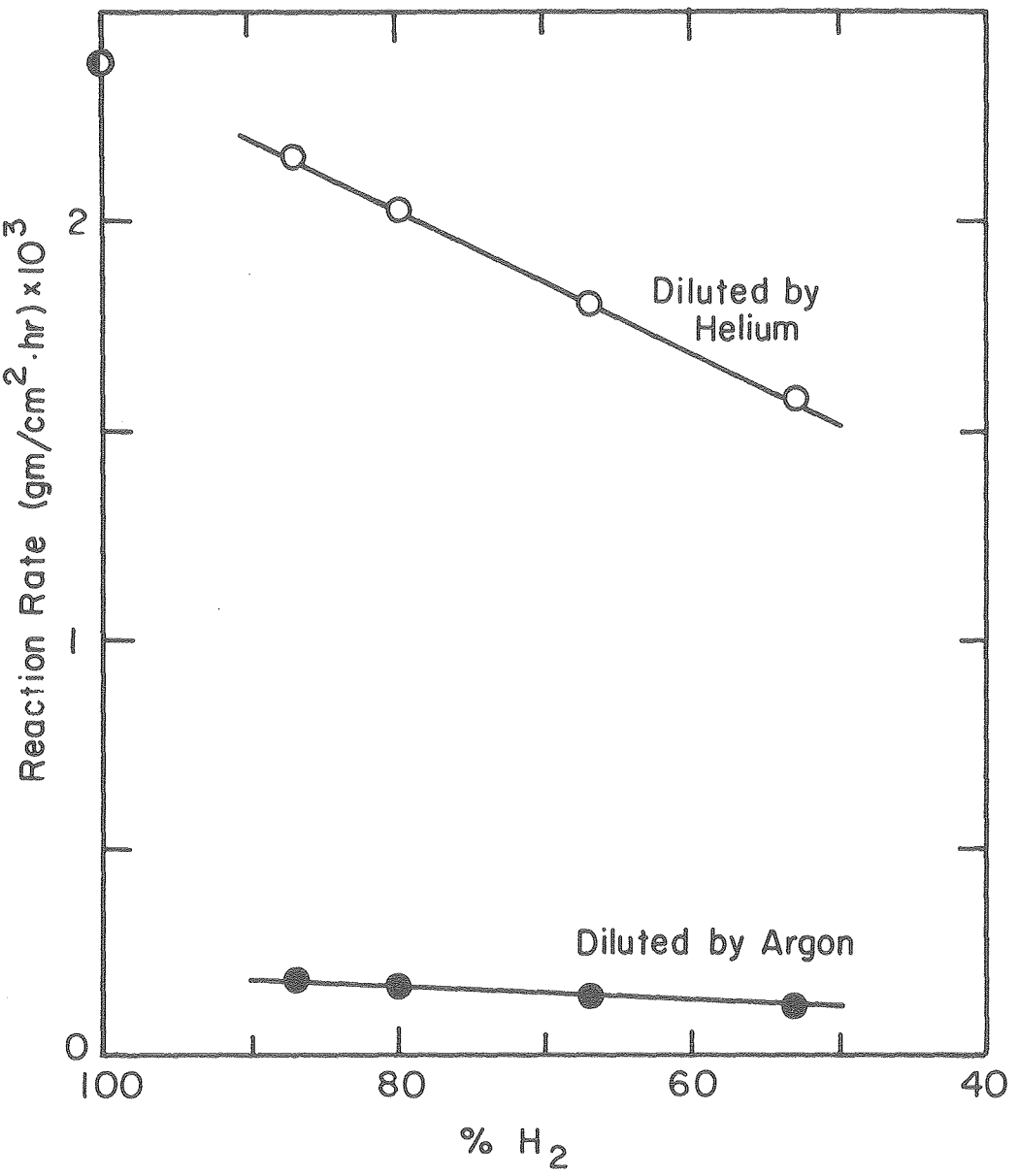
Reaction Rate (gm/cm^2·hr)×10^3
2
1
0
Diluted by Helium
Diluted by Argon
100
80
60
40
% H_2
XBL797-6549

Fig. 12

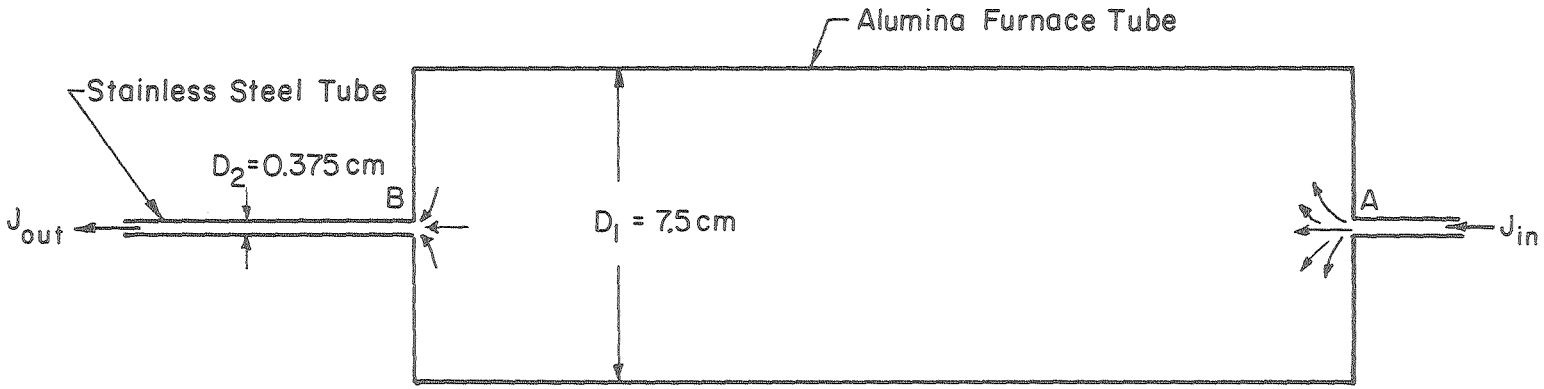

$$\frac{D_1}{D_2} = \frac{20}{1} \quad \therefore \quad \frac{A_1}{A_2} = \frac{400}{1}$$

XBL 797-6550

Fig. 13

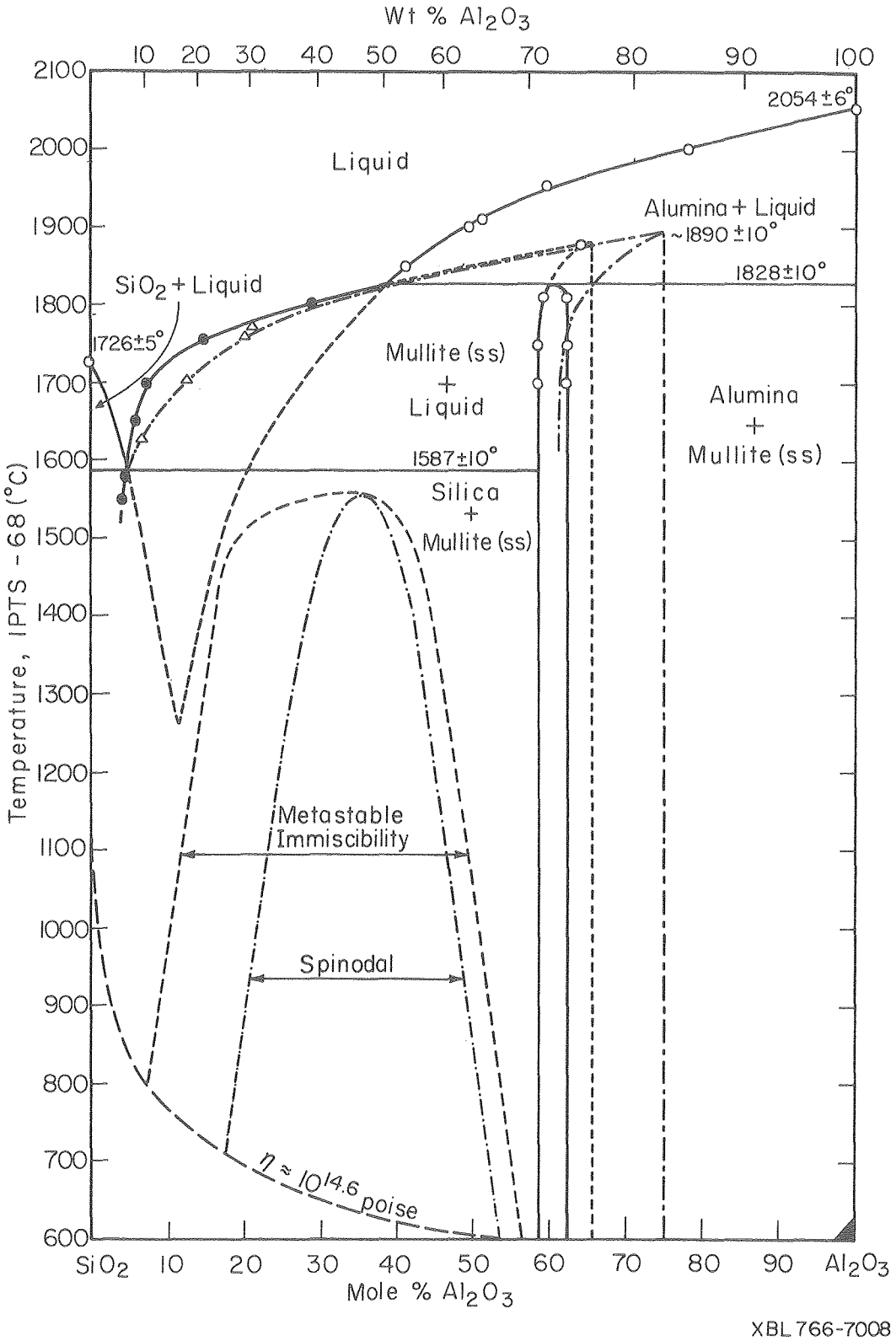

XBL 766-7008

Fig. 14

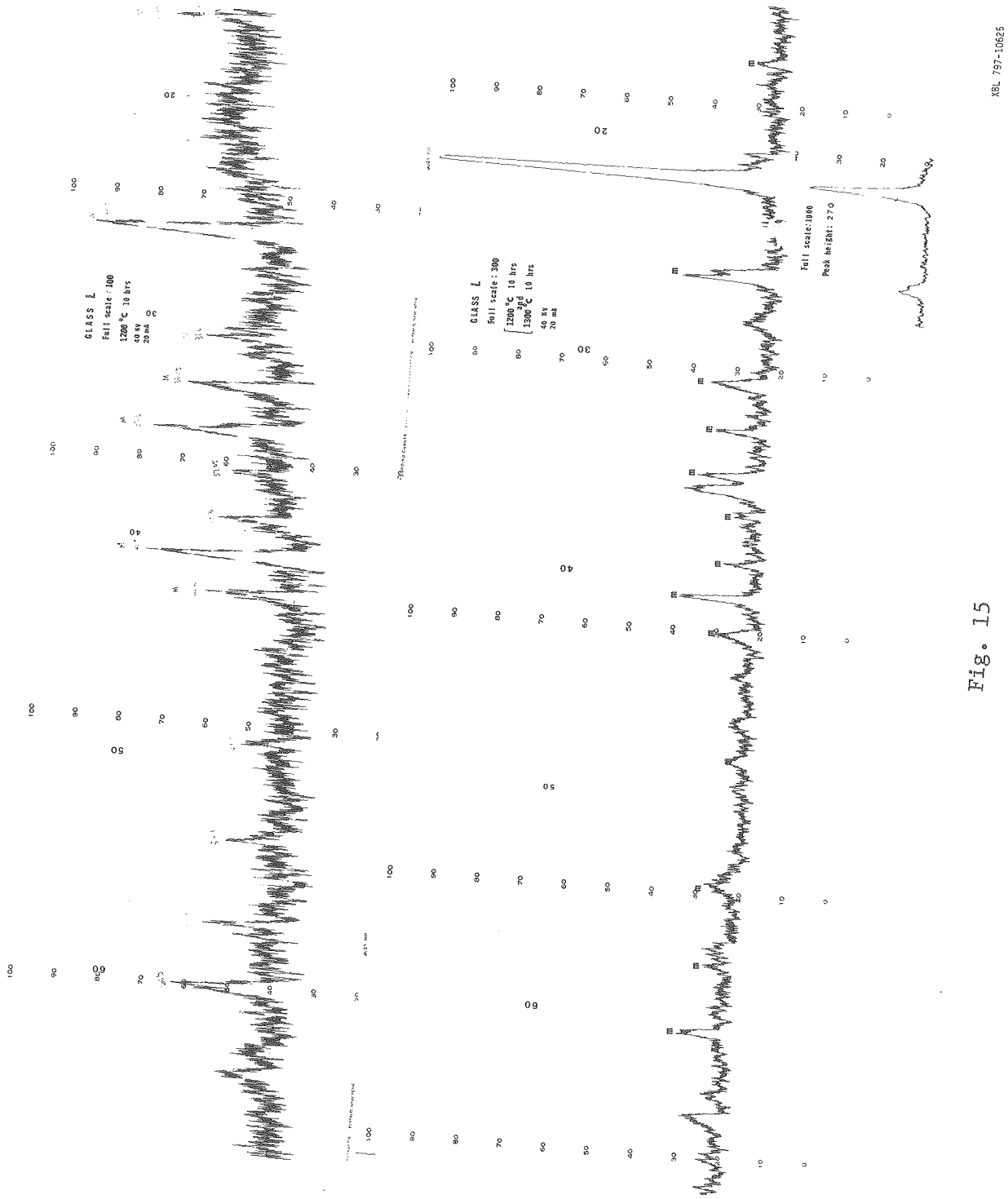
GLASS L
Full scale : 100
1200 °C 10 hrs
40 kV
20 mA
GLASS L
Full scale : 300
1200 °C 10 hrs
1300 °C 10 hrs
40 kV
20 mA
Full scale:1000
Peak height: 270
XBL 797-10625

Fig. 15

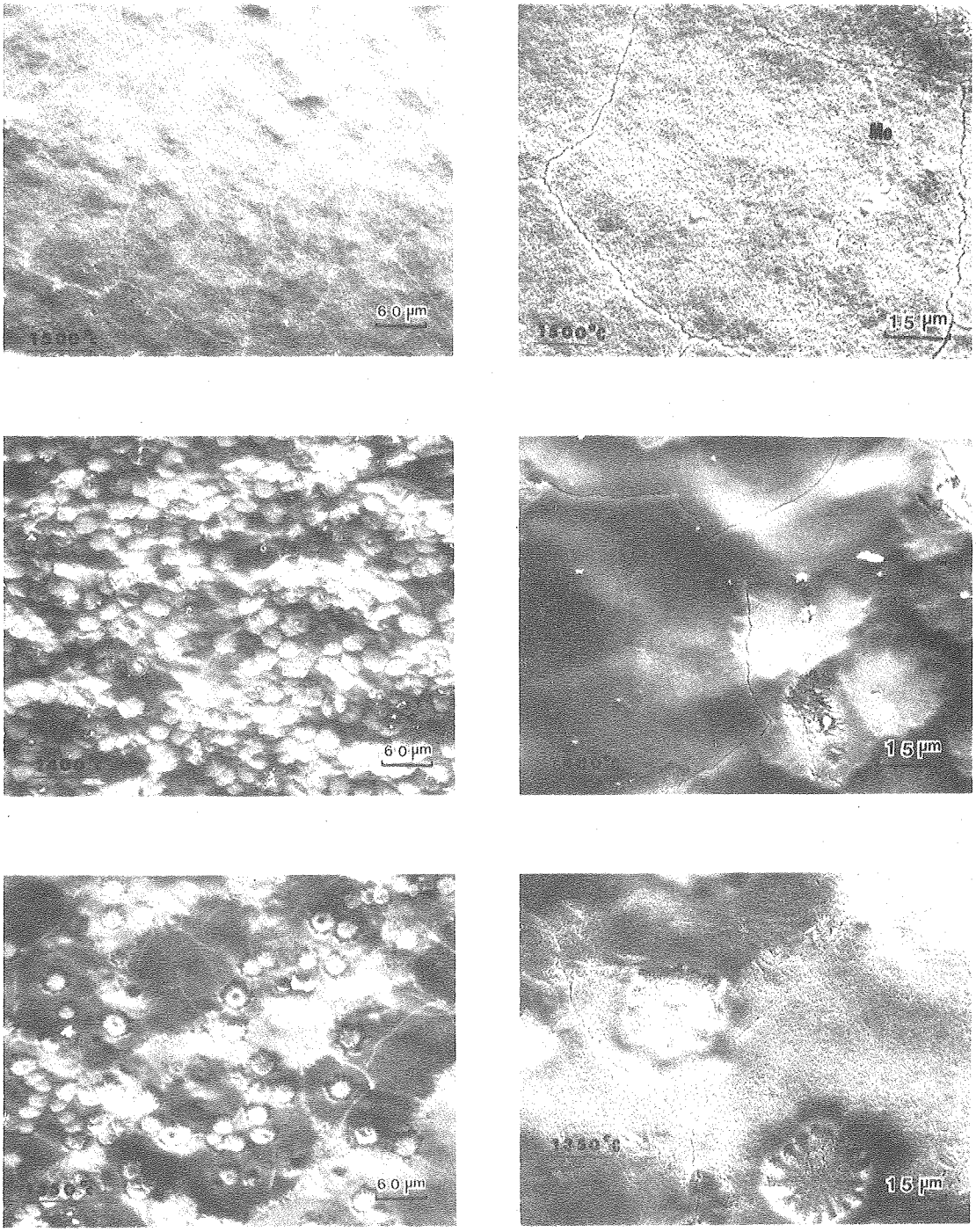

XBB794-5462

Fig. 16

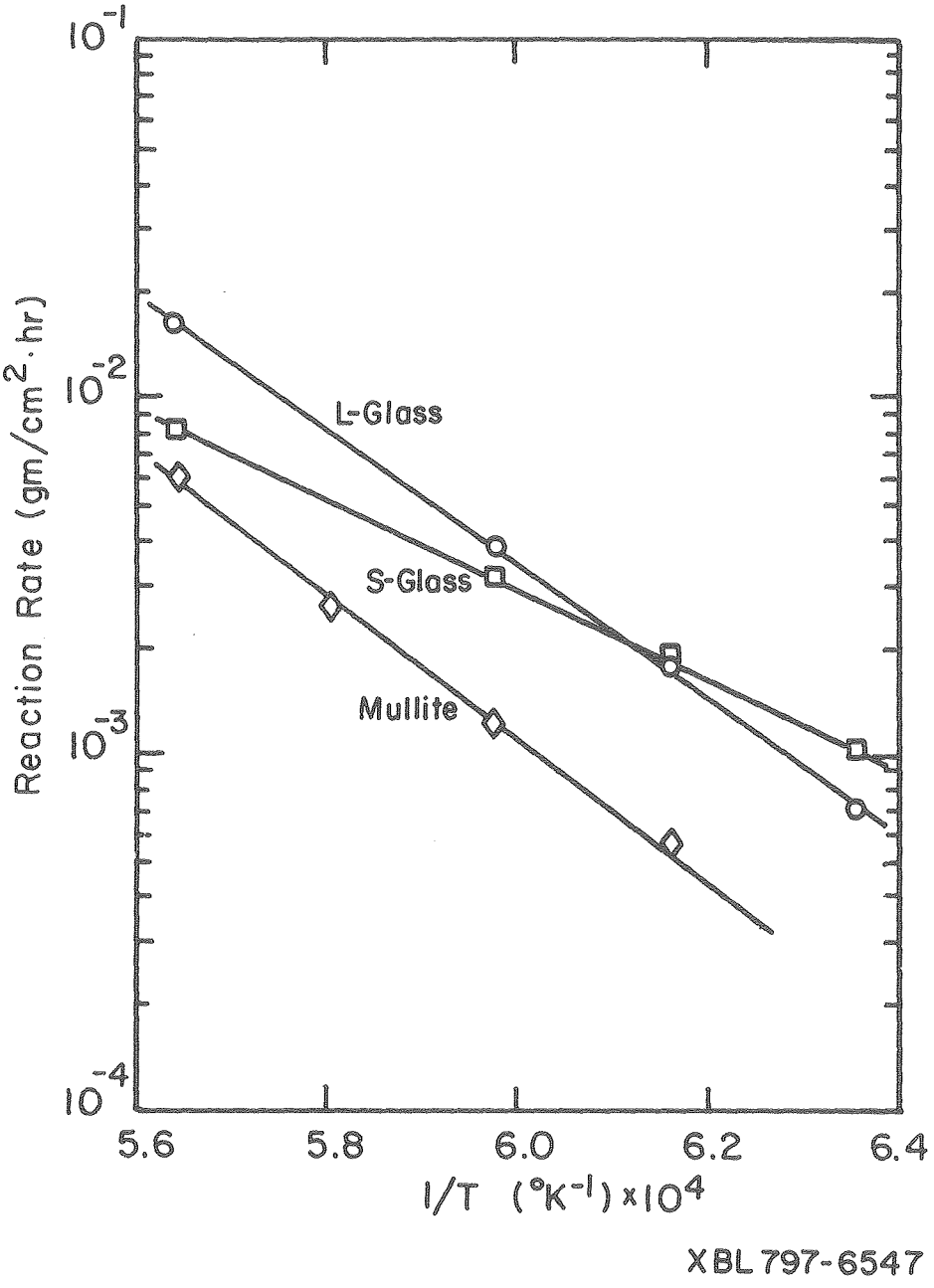
Reaction Rate (gm/cm^2·hr)
10^{-1}
10^{-2}
10^{-3}
10^{-4}
L-Glass
S-Glass
Mullite
5.6
5.8
6.0
6.2
6.4
1/T (°K^{-1}) x 10^4
XBL797-6547

Fig. 17

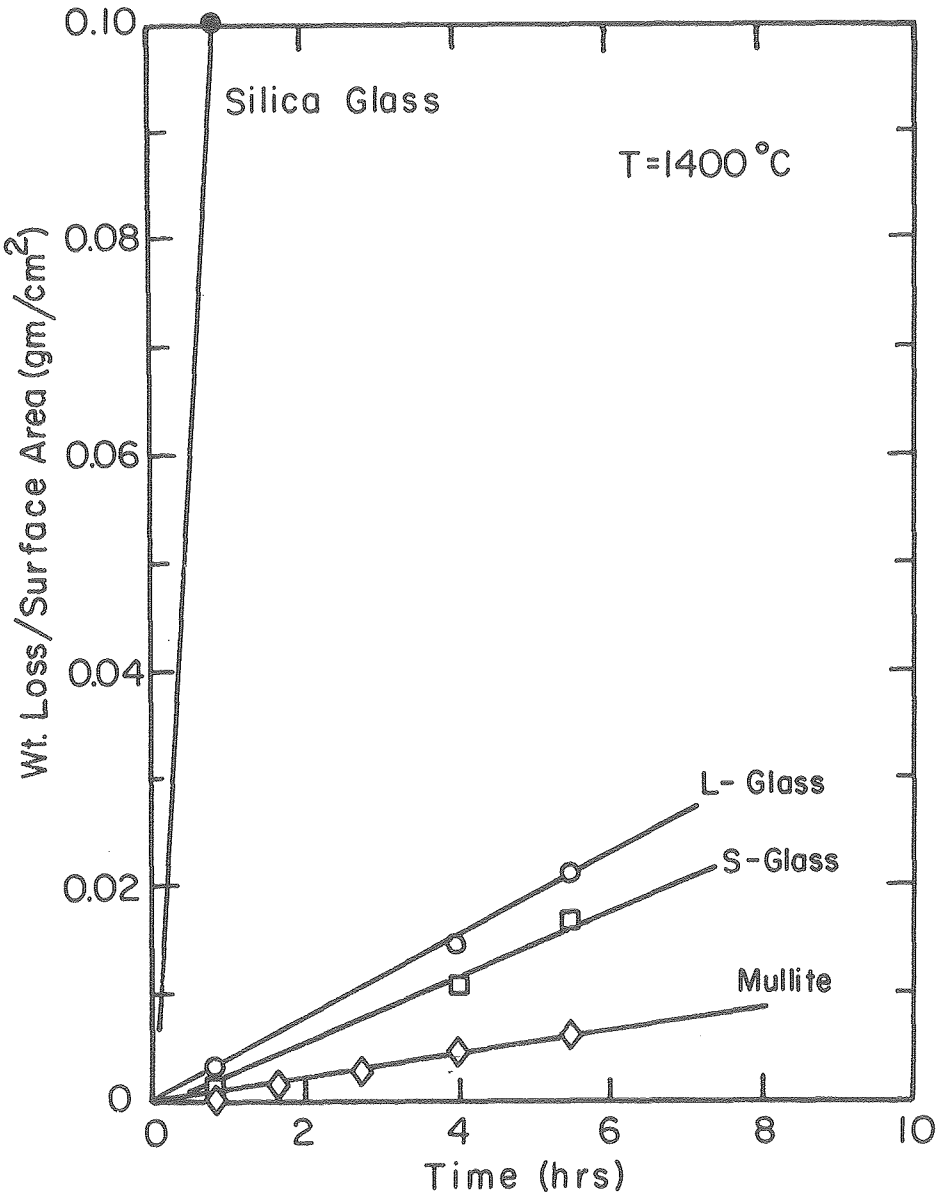
0.10
0.08
0.06
0.04
0.02
0
Wt. Loss/Surface Area (gm/cm²)
Silica Glass
T=1400 °C
L- Glass
S-Glass
Mullite
0
2
4
6
8
10
Time (hrs)
XBL 797-6546

Fig. 18

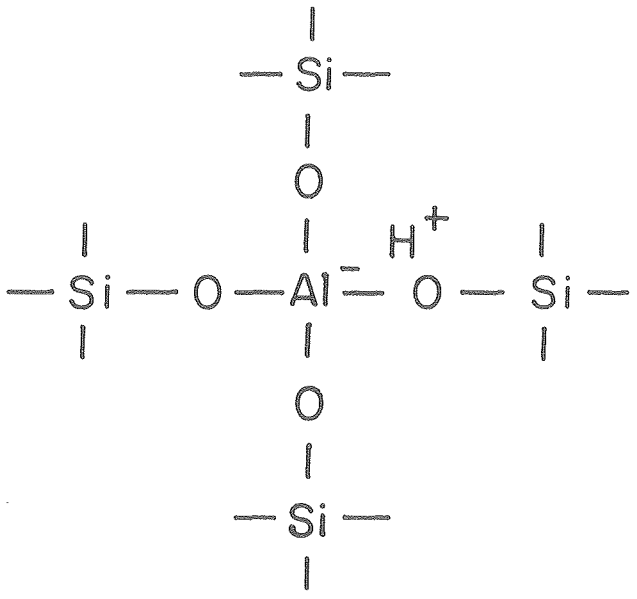

(a)

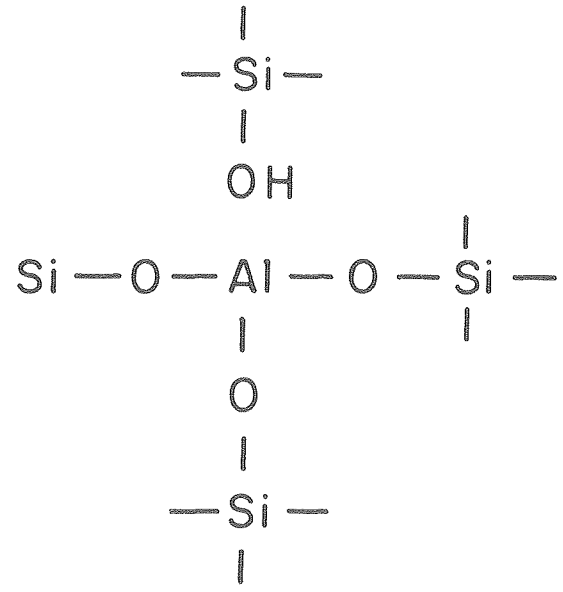

(b)

XBL799-6992

Fig. 19

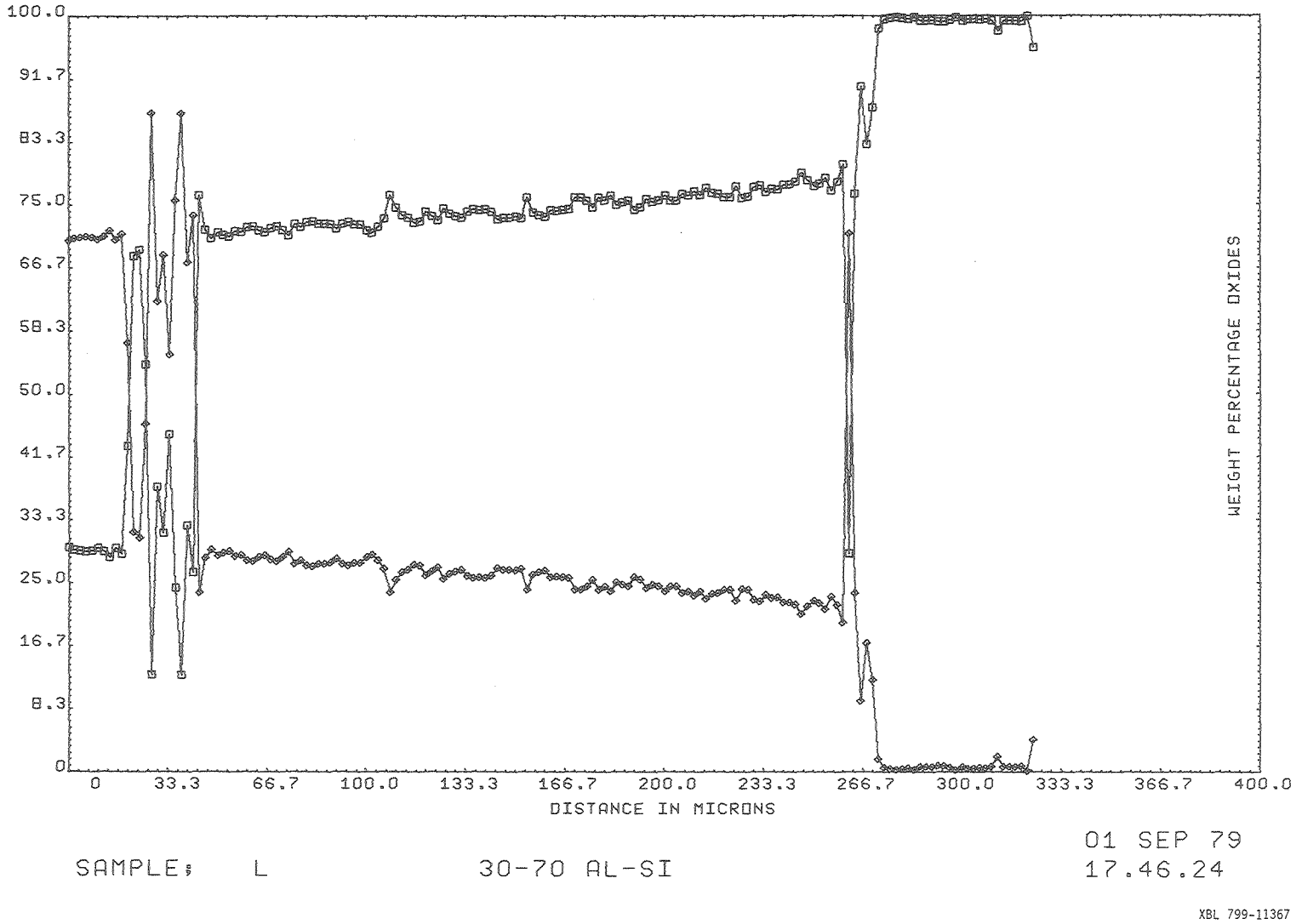
100.0
91.7
83.3
75.0
66.7
58.3
50.0
41.7
33.3
25.0
16.7
8.3
0
0
33.3
66.7
100.0
133.3
166.7
200.0
233.3
266.7
300.0
333.3
366.7
400.0
DISTANCE IN MICRONS
WEIGHT PERCENTAGE OXIDES
SAMPLE; L
30-70 AL-SI
01 SEP 79
17.46.24
XBL 799-11367

Fig. 20

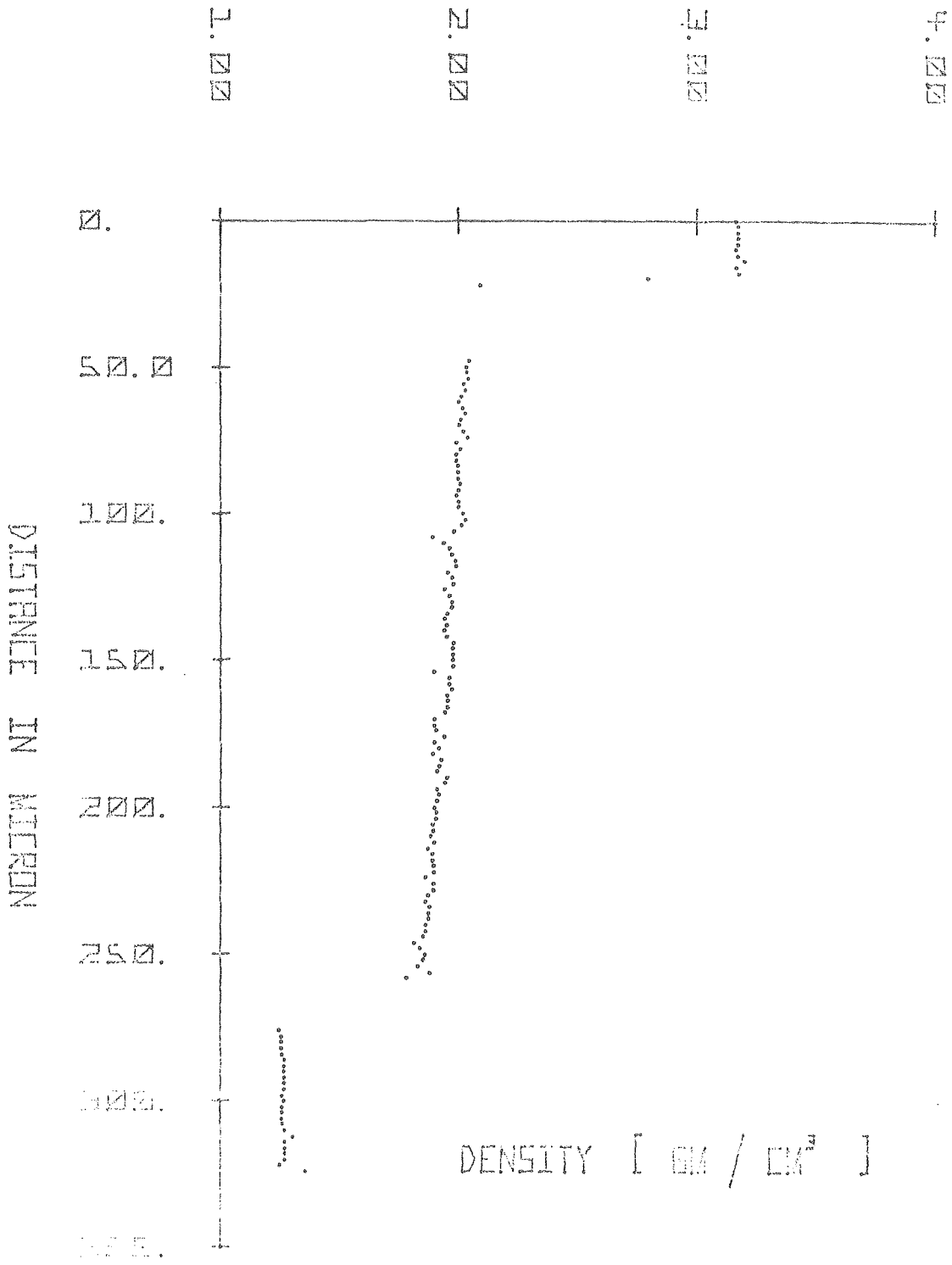

XBL 799-11361

Fig. 21

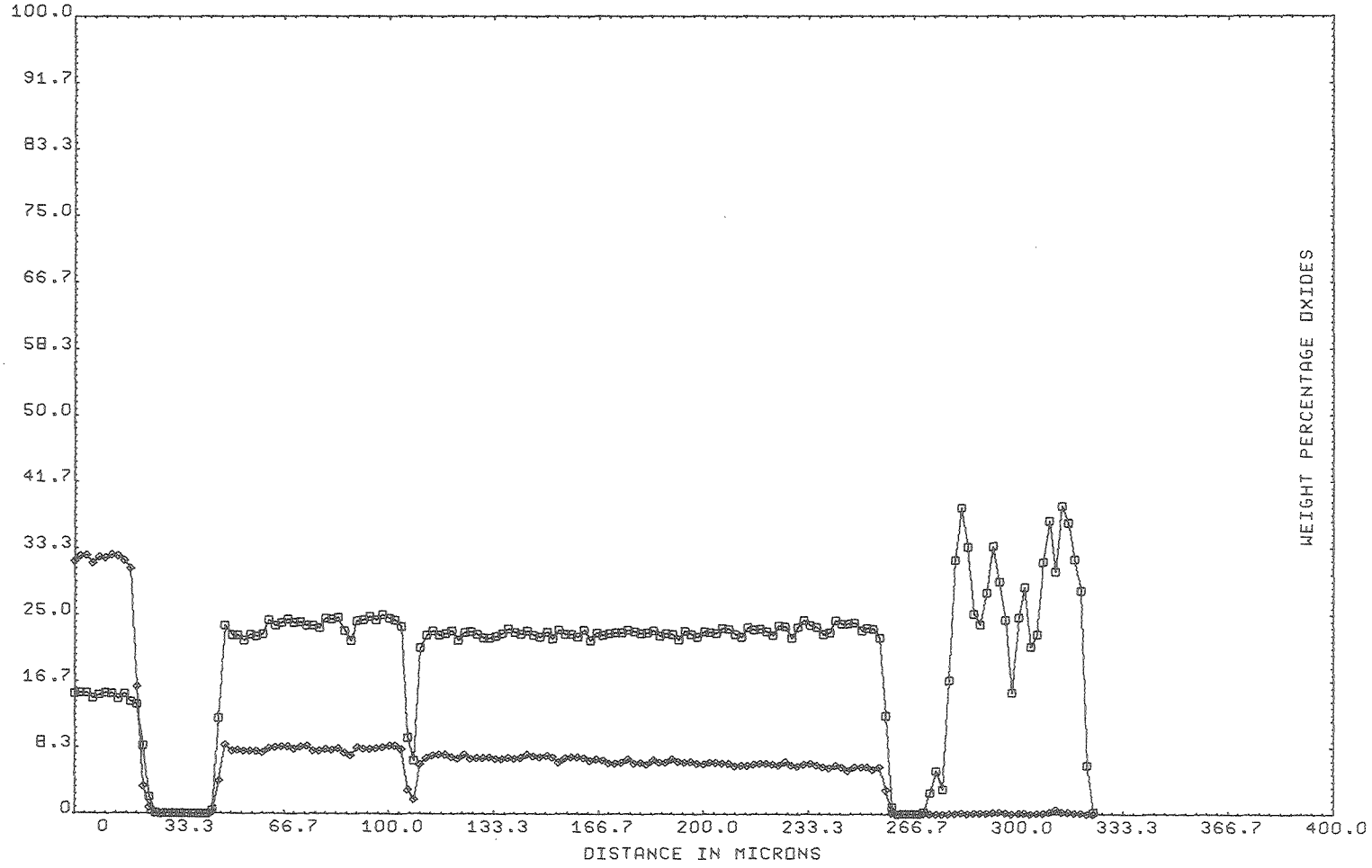
100.0
91.7
83.3
75.0
66.7
58.3
50.0
41.7
33.3
25.0
16.7
8.3
0
0
33.3
66.7
100.0
133.3
166.7
200.0
233.3
266.7
300.0
333.3
366.7
400.0
DISTANCE IN MICRONS
WEIGHT PERCENTAGE OXIDES
SAMPLE; L
30-70 AL-SI
01 SEP 79
23.12.15
XBL 799-11366

Fig. 22

$CaO-Al_2O_3-SiO_2$

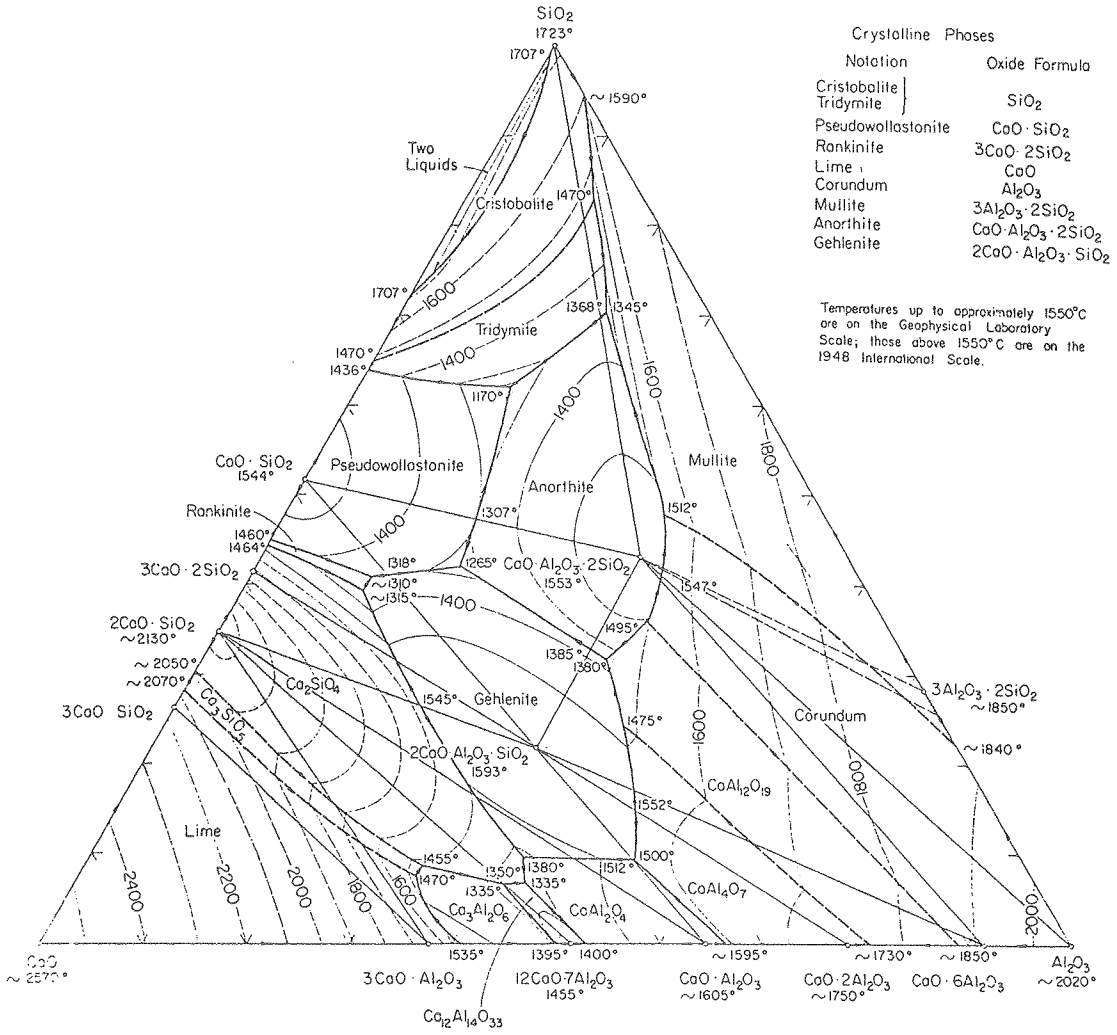

FIG. 630.—System $CaO-Al_2O_3-SiO_2$; composite.

E. F. Osborn and Arnulf Muan, revised and redrawn "Phase Equilibrium Diagrams of Oxide Systems," Plate 1, published by the American Ceramic Society and the Edward Orton, Jr., Ceramic Foundation, 1960.

Principal References

A. L. Day, E. S. Shepherd, and F. E. Wright, *Am. J. Sci.* (4th series), 22, 265–302 (1906).
J. H. Welch and W. Gutt, *J. Am. Ceram. Soc.*, 42, 11–15 (1959).
N. L. Bowen and J. W. Greig, *J. Am. Ceram. Soc.*, 7, 238–54 (1924); corrections, *ibid.*, 410.
N. A. Toropov and F. Ya. Galakhov, *Voprosy Petrograf. i Mineral., Akad. Nauk S.S.S.R.*, 2, 245–55 (1953).
G. A. Rankin and F. E. Wright, *Am. J. Sci.* (4th Series), 39, 1–79 (1915).
J. W. Greig, *Am. J. Sci.* (5th Series), 13, 1–44; 133–54 (1927).
N. F. Filonenko and I. V. Iavrov, *Zhur. Prik. Khim.*, 23, 1040–46 (1950); *J. Appl. Chem.* (*U.S.S.R.*), 23, 1105–12 (1950) (English translation).
S. Aramaki and Rustum Roy, *J. Am. Ceram. Soc.*, 42, 644–45 (1959).

Fig. 23

$CaO-SiO_2$

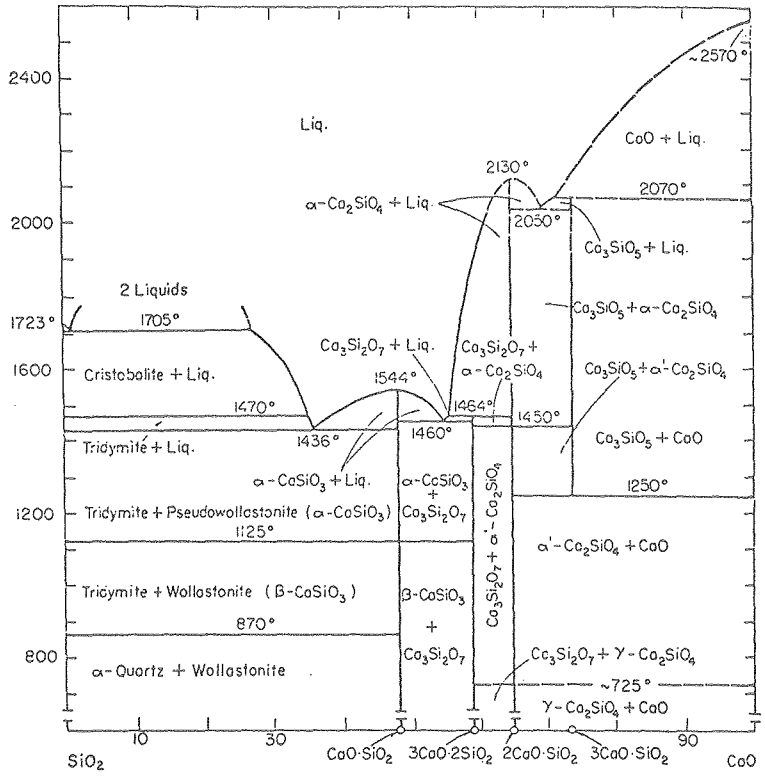

FIG. 237.—System $CaO-SiO_2$.

Bert Phillips and Arnulf Muan, *J. Am. Ceram. Soc.*, 42 [9] 414 (1959).

Based mainly on data of G. A. Rankin and F. E. Wright, *Am. J. Sci.* [4], 39, 5 (1915) and J. W. Greig, *Am. J. Sci.*, [5], 13, 1–44; [74] 133–54 (1927). Changes with respect to stability relations of tricalcium and dicalcium silicates based on data of D. M. Roy, *J. Am. Ceram. Soc.*, 41 [8] 293–99 (1958) and J. H. Welch and W. Gutt, *J. Am. Ceram. Soc.*, 42 [1] 11–15 (1959).

$CaO-SiO_2$

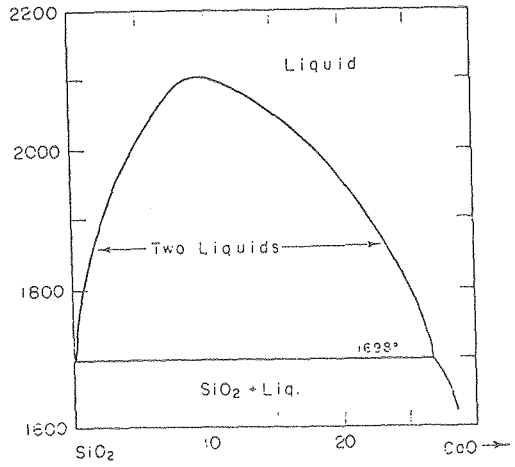

FIG. 2302.—System $CaO-SiO_2$ showing immiscibility dome.

Fig. 24

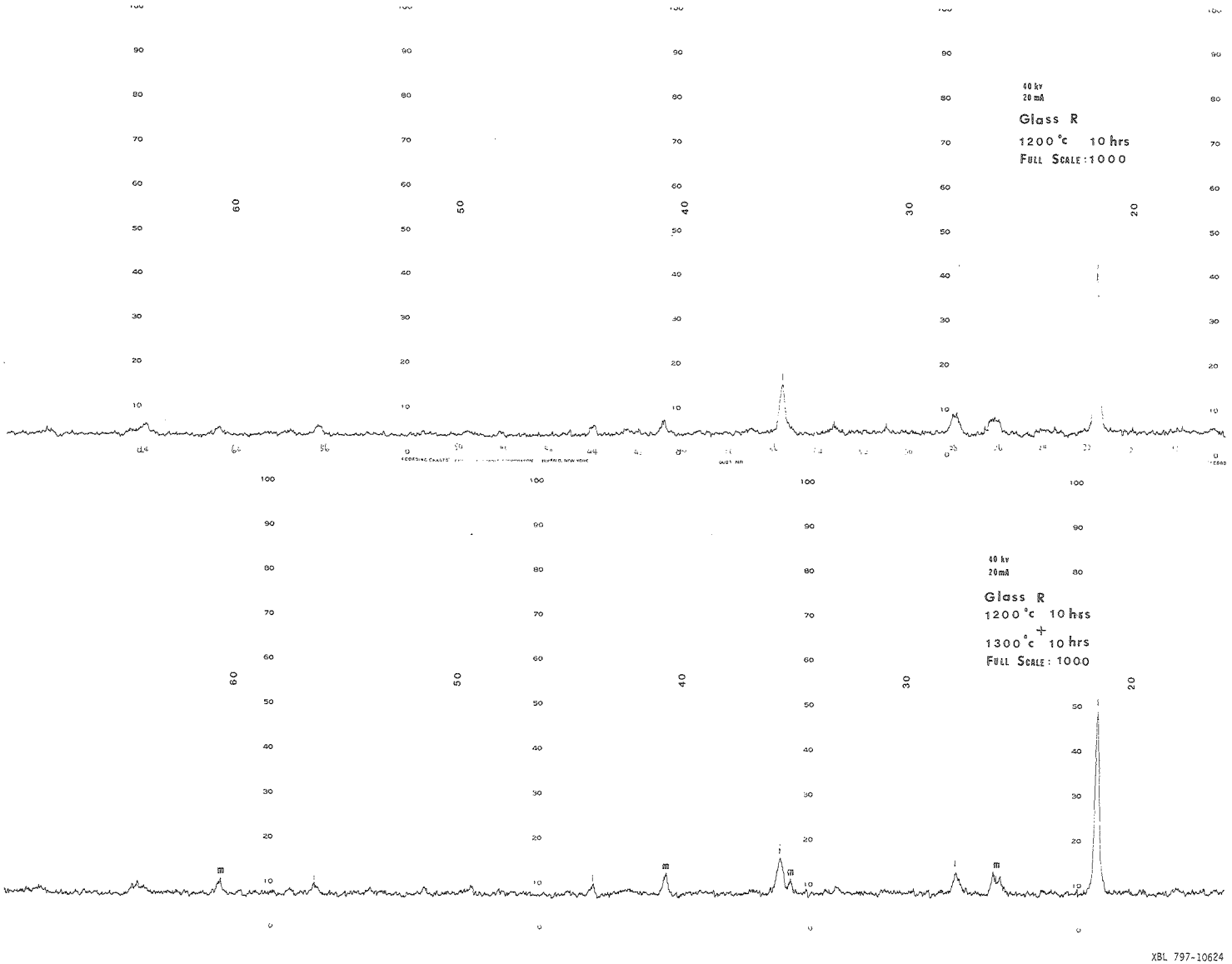
40 kv
20 mA
Glass R
1200 °c 10 hrs
Full Scale: 1000
40 kv
20mA
Glass R
1200 °c 10 hrs
+
1300 °c 10 hrs
Full Scale: 1000
XBL 797-10624

Fig. 25

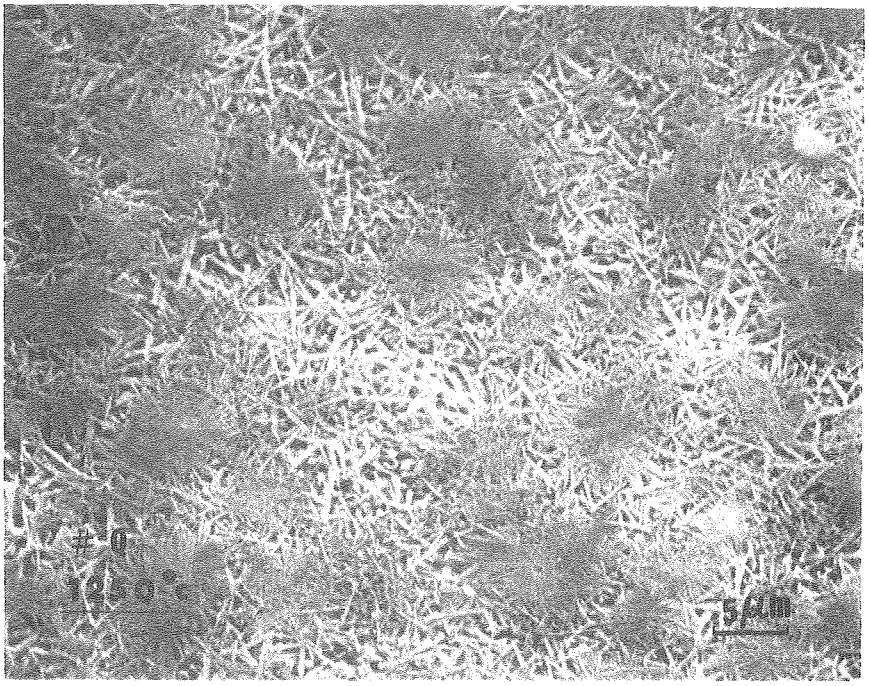

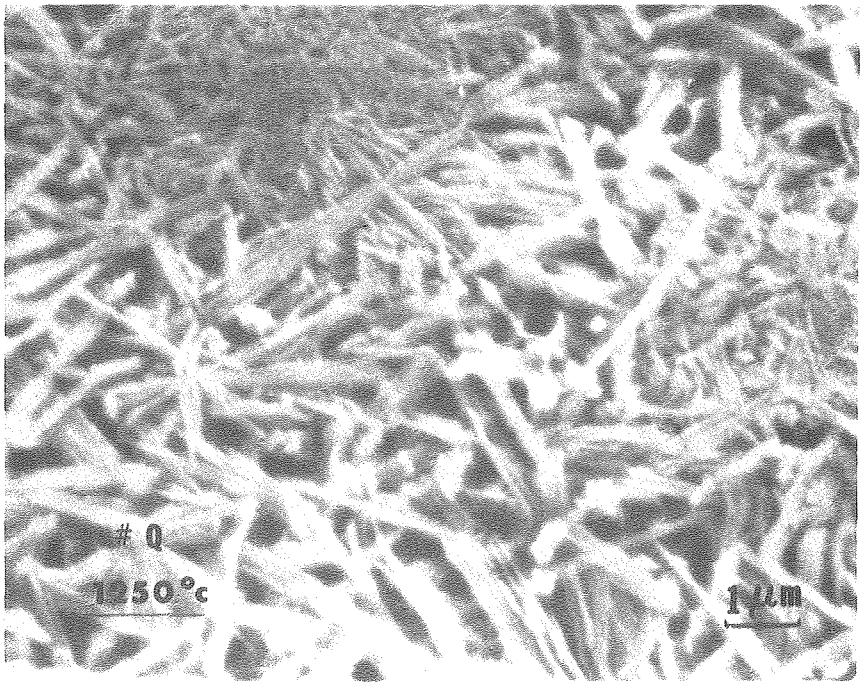

XBB794-5464

Fig. 26

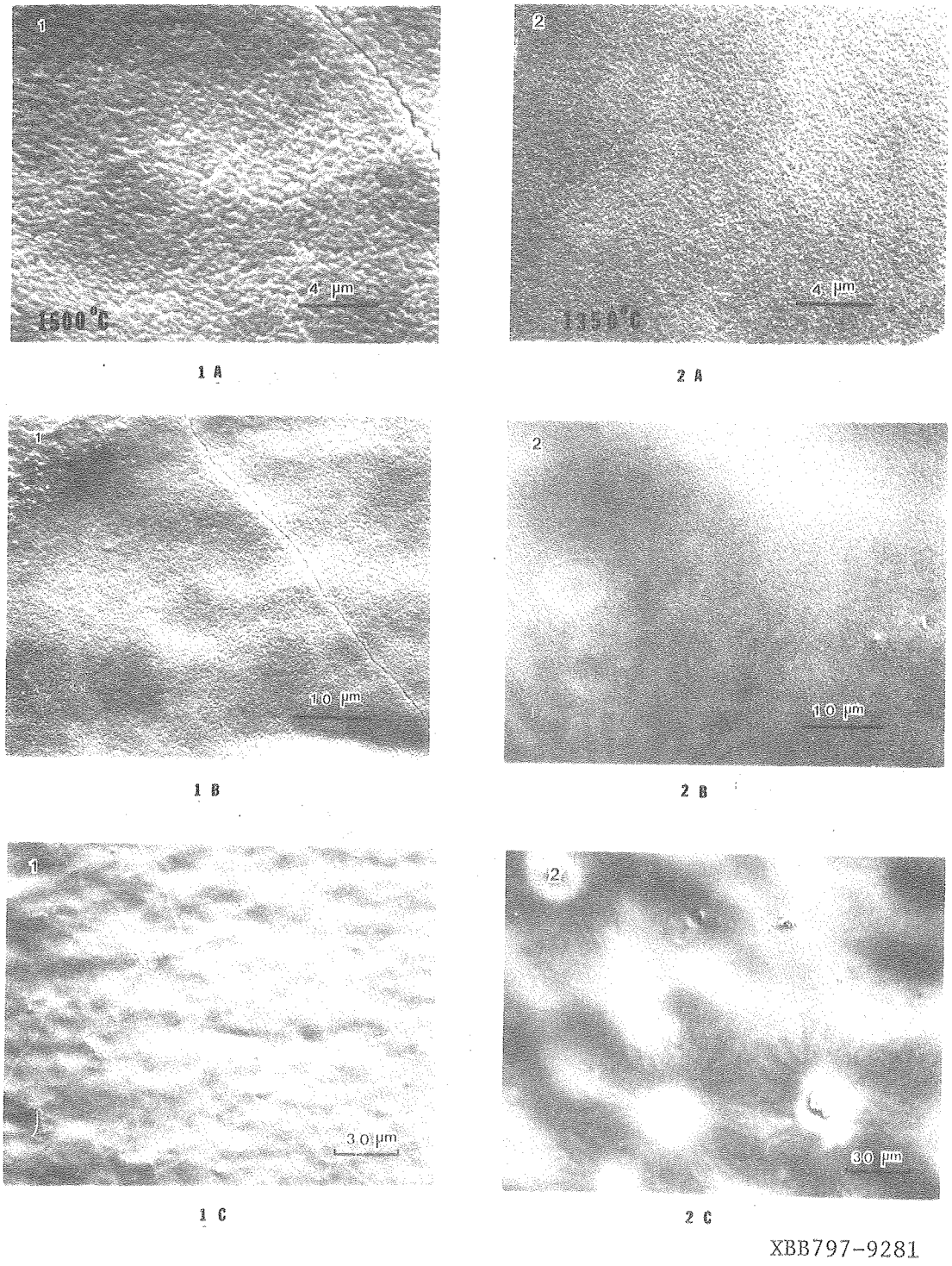

XBB797-9281

Fig. 27

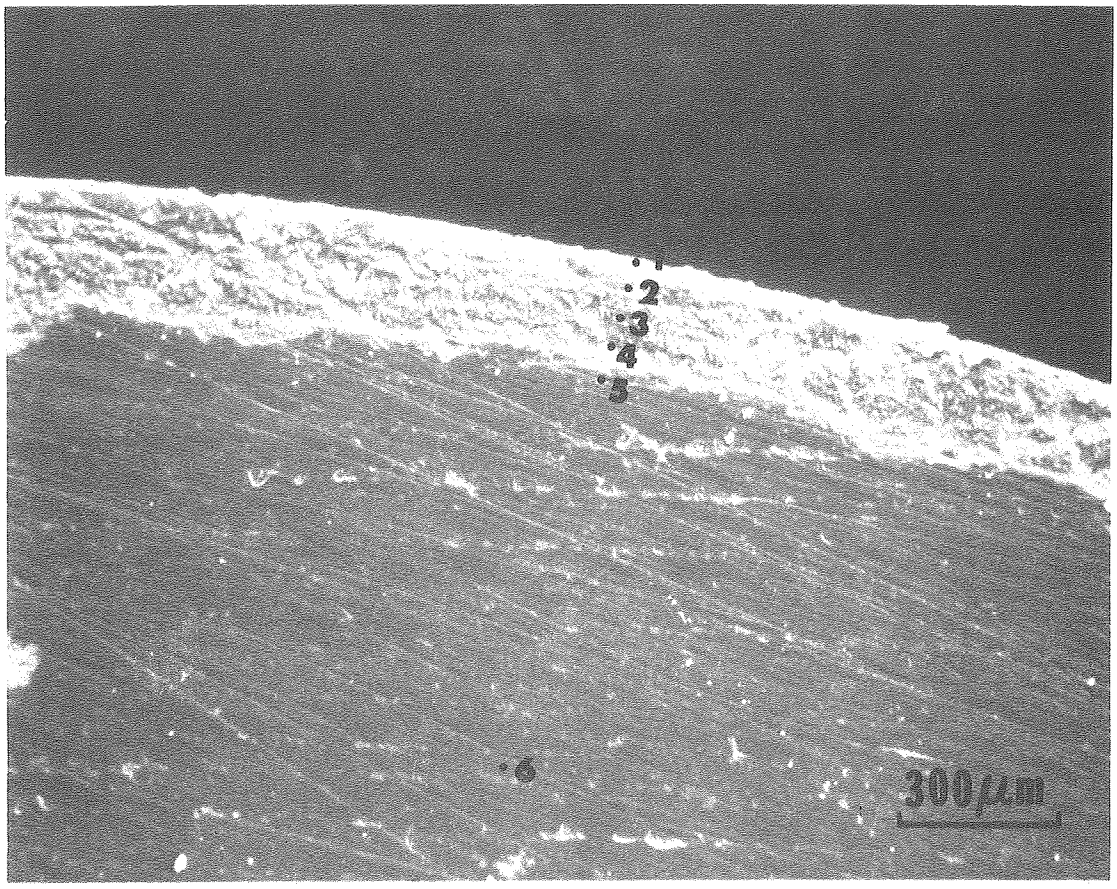

XBB789-10817

Fig. 28

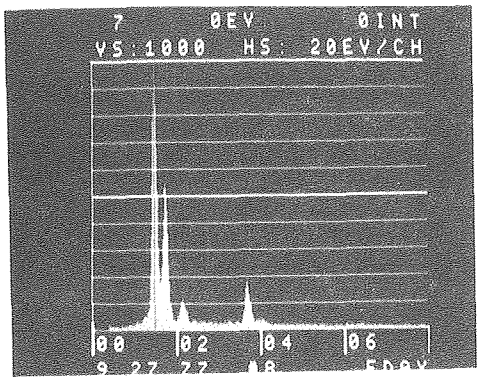

1

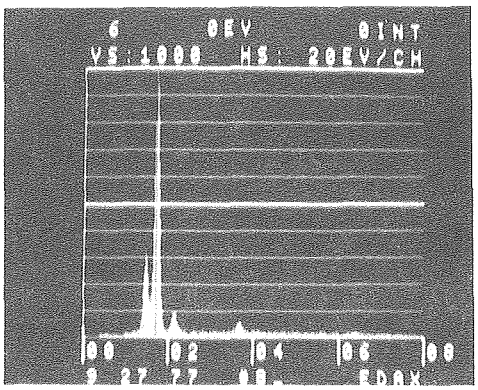

4

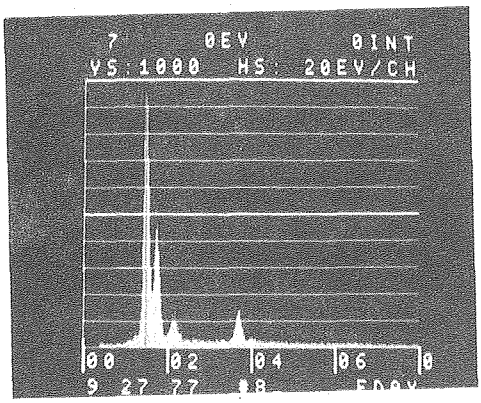

2

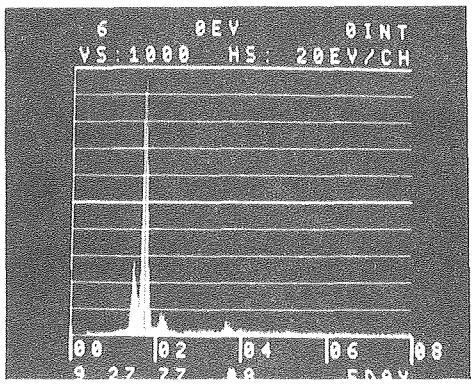

5

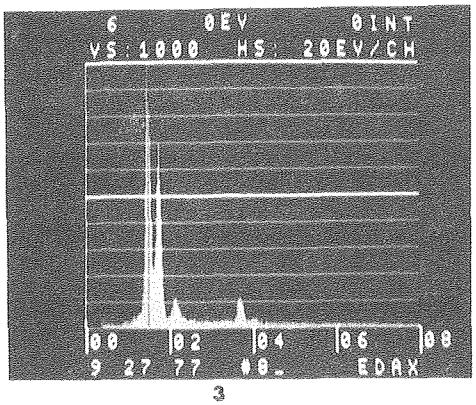

3

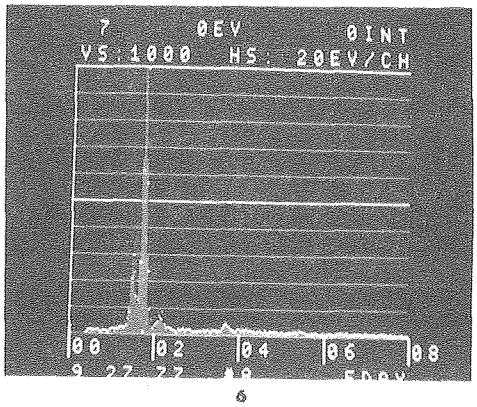

6

XBB789-10818

Fig. 29

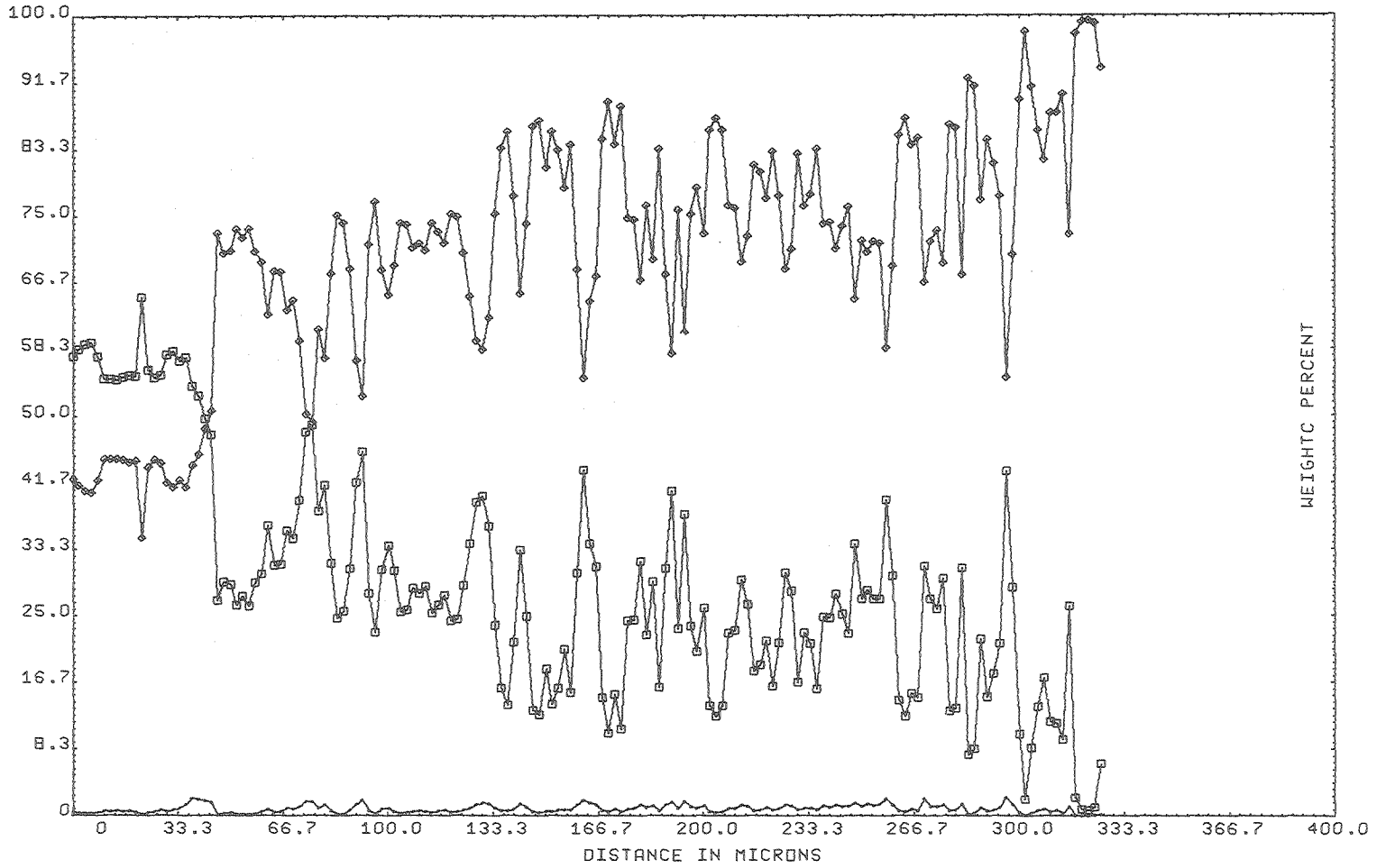
100.0
91.7
83.3
75.0
66.7
58.3
50.0
41.7
33.3
25.0
16.7
8.3
0
0
33.3
66.7
100.0
133.3
166.7
200.0
233.3
266.7
300.0
333.3
366.7
400.0
DISTANCE IN MICRONS
WEIGHTC PERCENT
SAMPLE: S
60-40-5 SI AL CA
01 SEP 79
23.00.46
XBL 799-11362

Fig. 30

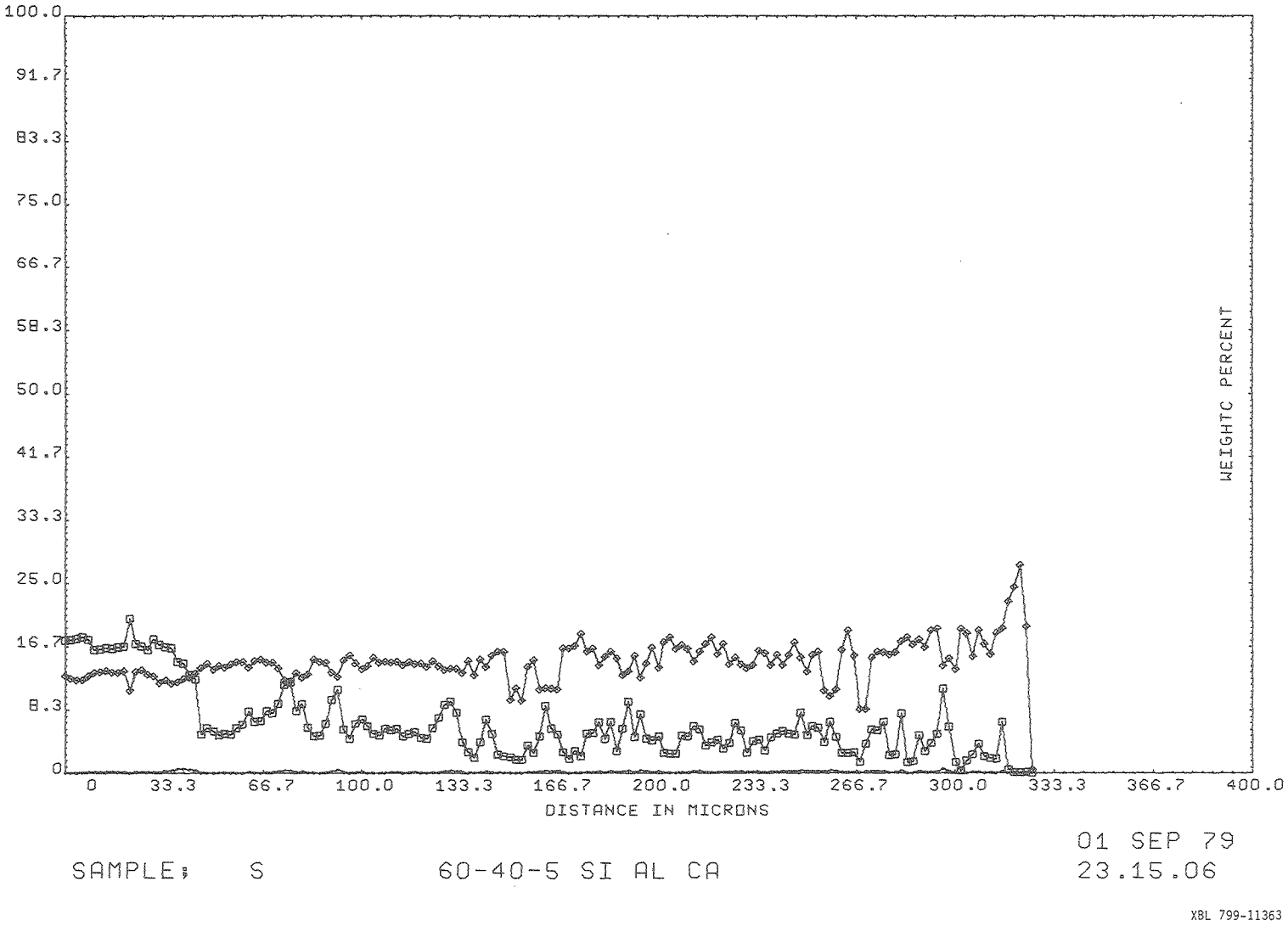
100.0
91.7
83.3
75.0
66.7
58.3
50.0
41.7
33.3
25.0
16.7
8.3
0
0
33.3
66.7
100.0
133.3
166.7
200.0
233.3
266.7
300.0
333.3
366.7
400.0
DISTANCE IN MICRONS
WEIGHTC PERCENT
SAMPLE: S 60-40-5 SI AL CA
01 SEP 79
23.15.06
XBL 799-11363

Fig. 31

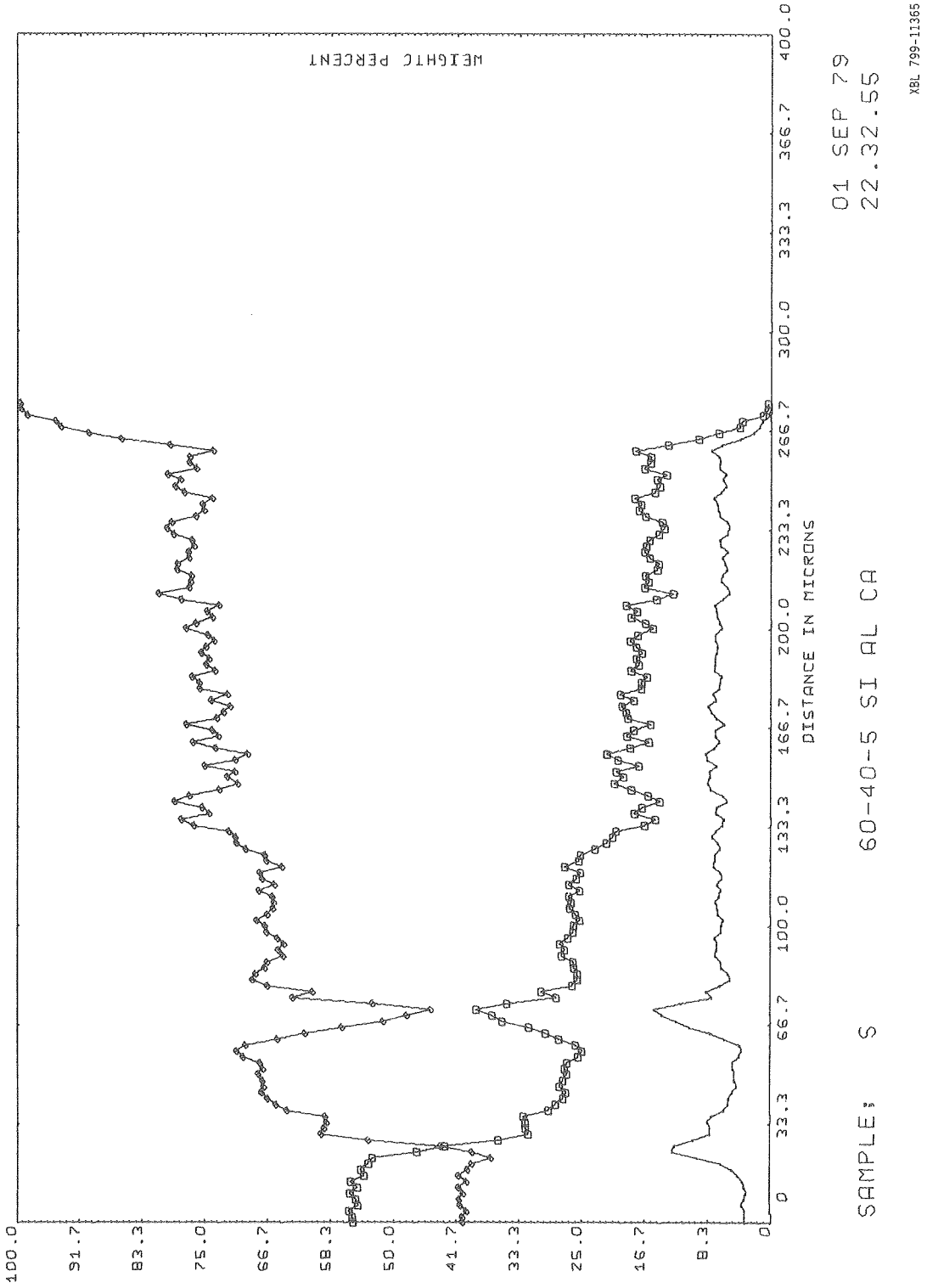
WEIGHTC PERCENT
100.0
91.7
83.3
75.0
66.7
58.3
50.0
41.7
33.3
25.0
16.7
8.3
0
0
33.3
66.7
100.0
133.3
166.7
200.0
233.3
266.7
300.0
333.3
366.7
400.0
DISTANCE IN MICRONS
SAMPLE: S 60-40-5 SI AL CA
01 SEP 79
22.32.55
XBL 799-11365

Fig. 32

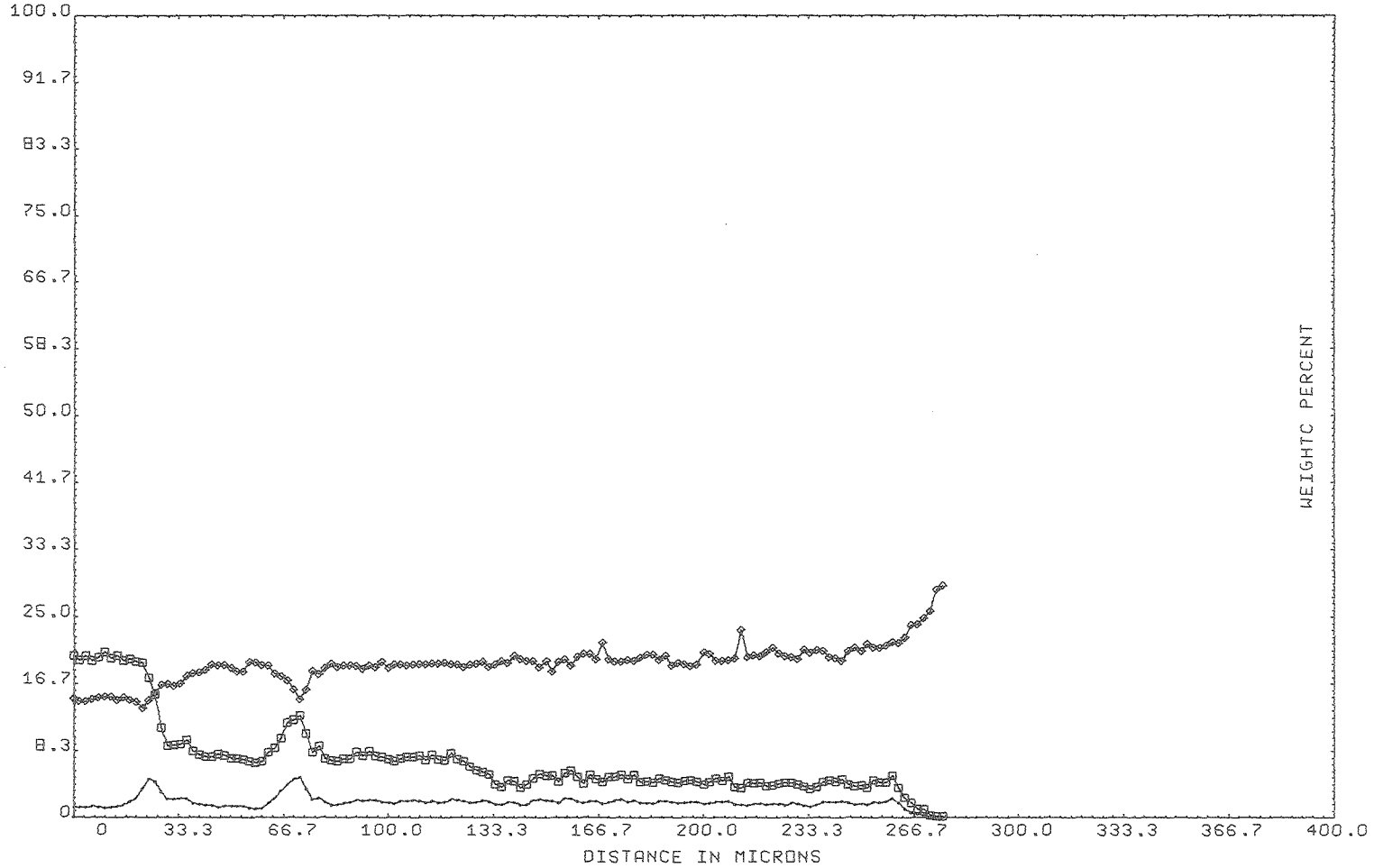
100.0
91.7
83.3
75.0
66.7
58.3
50.0
41.7
33.3
25.0
16.7
8.3
0
0
33.3
66.7
100.0
133.3
166.7
200.0
233.3
266.7
300.0
333.3
366.7
400.0
DISTANCE IN MICRONS
WEIGHTC PERCENT
SAMPLE: S
60-40-5 SI AL CA
01 SEP 79
23.05.34
XBL 799-11364

Fig. 33

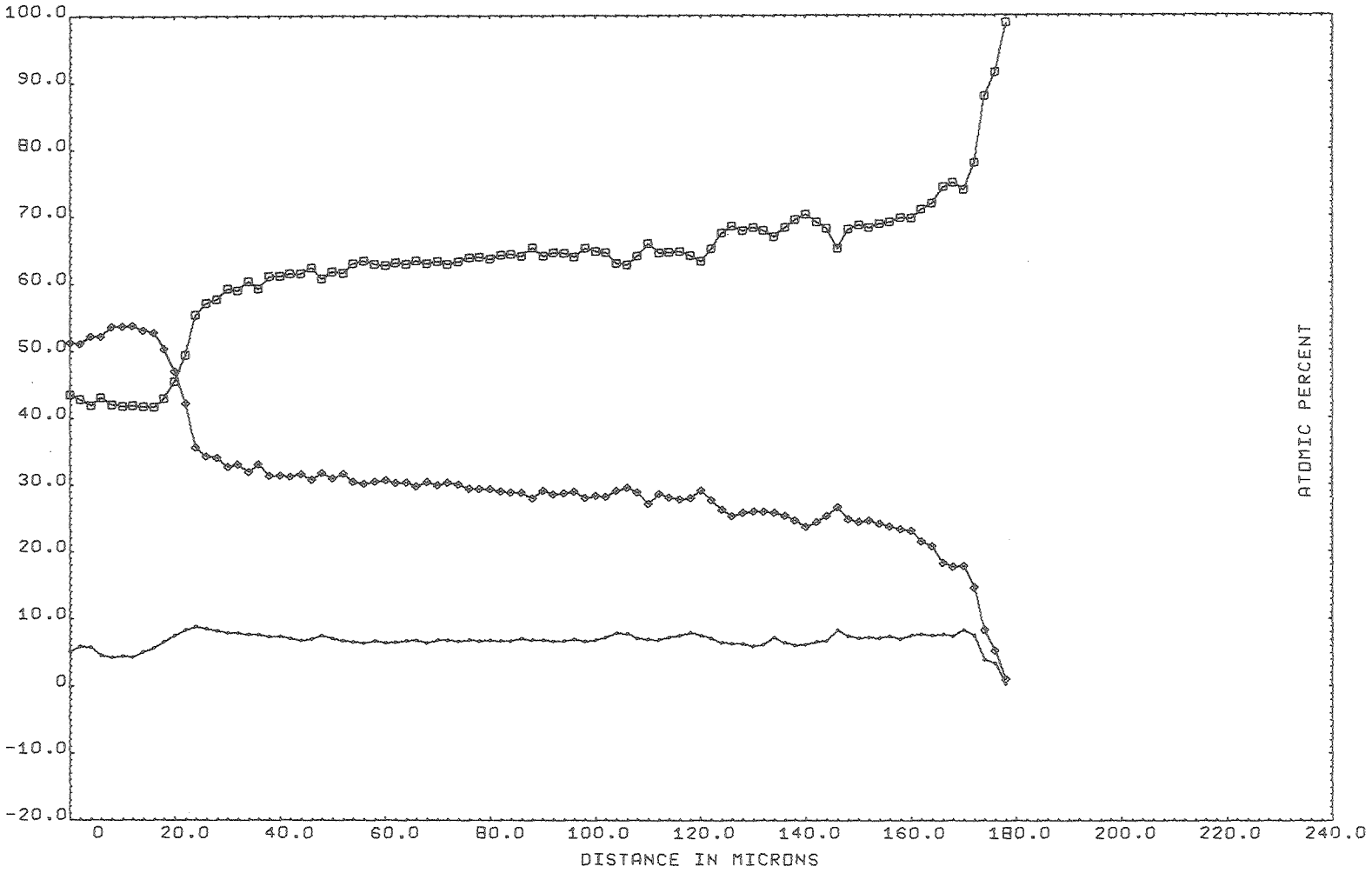
100.0
90.0
80.0
70.0
60.0
50.0
40.0
30.0
20.0
10.0
0
-10.0
-20.0
0
20.0
40.0
60.0
80.0
100.0
120.0
140.0
160.0
180.0
200.0
220.0
240.0
DISTANCE IN MICRONS
ATOMIC PERCENT
SAMPLE: S
60-40-5 AL SI CA
28 NOV 78
20.37.31
XBL 792-8436

Fig. 34

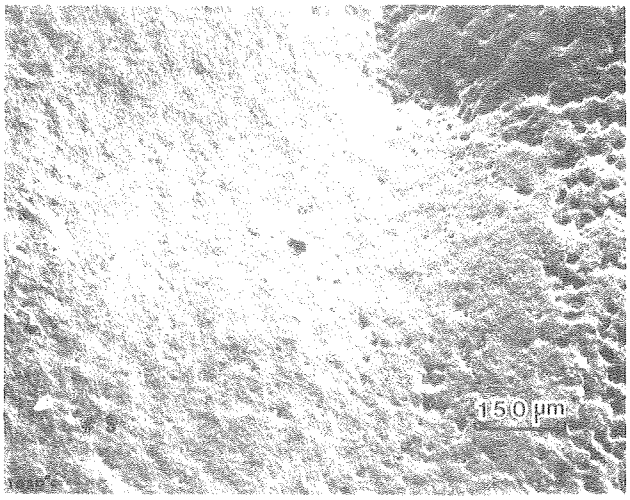

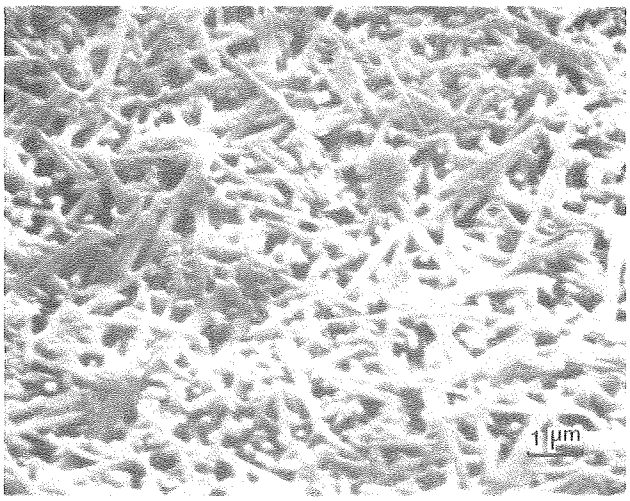

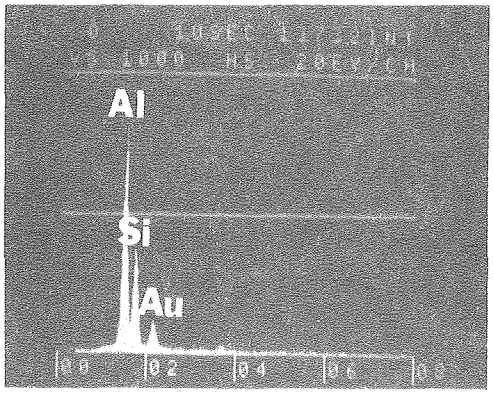

XBB794-5463

Fig. 35

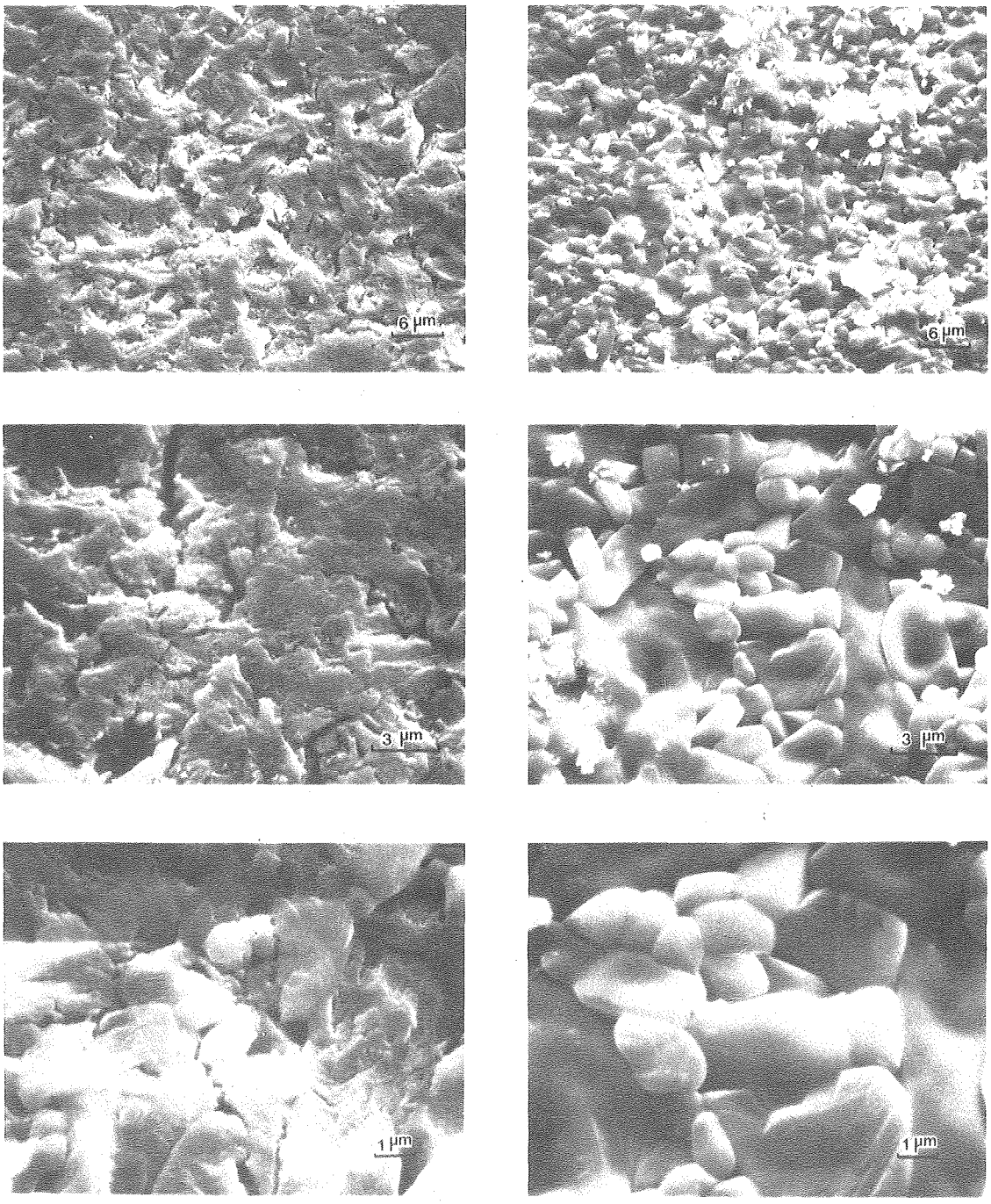

XBB794-5465

POLISHED AND THEN REACTED WITH H_2 AT 1400 °C

AS SINTERED

Fig. 36

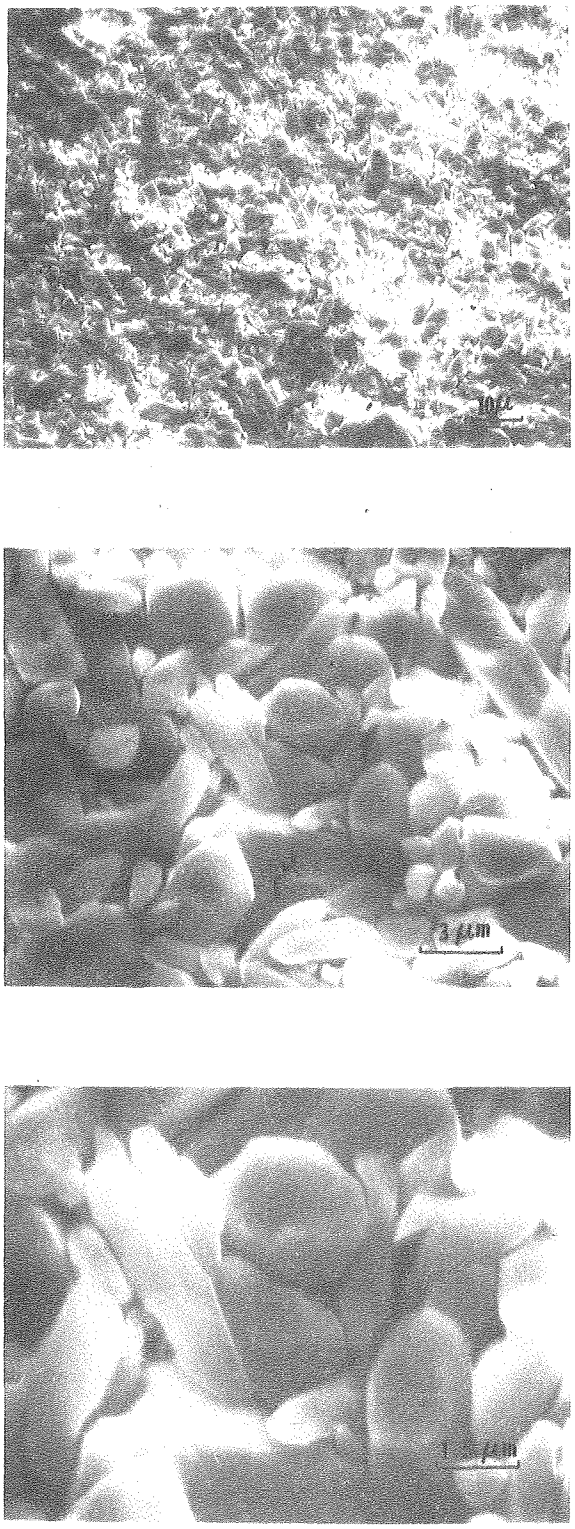

XBB797-8917

Fig. 37

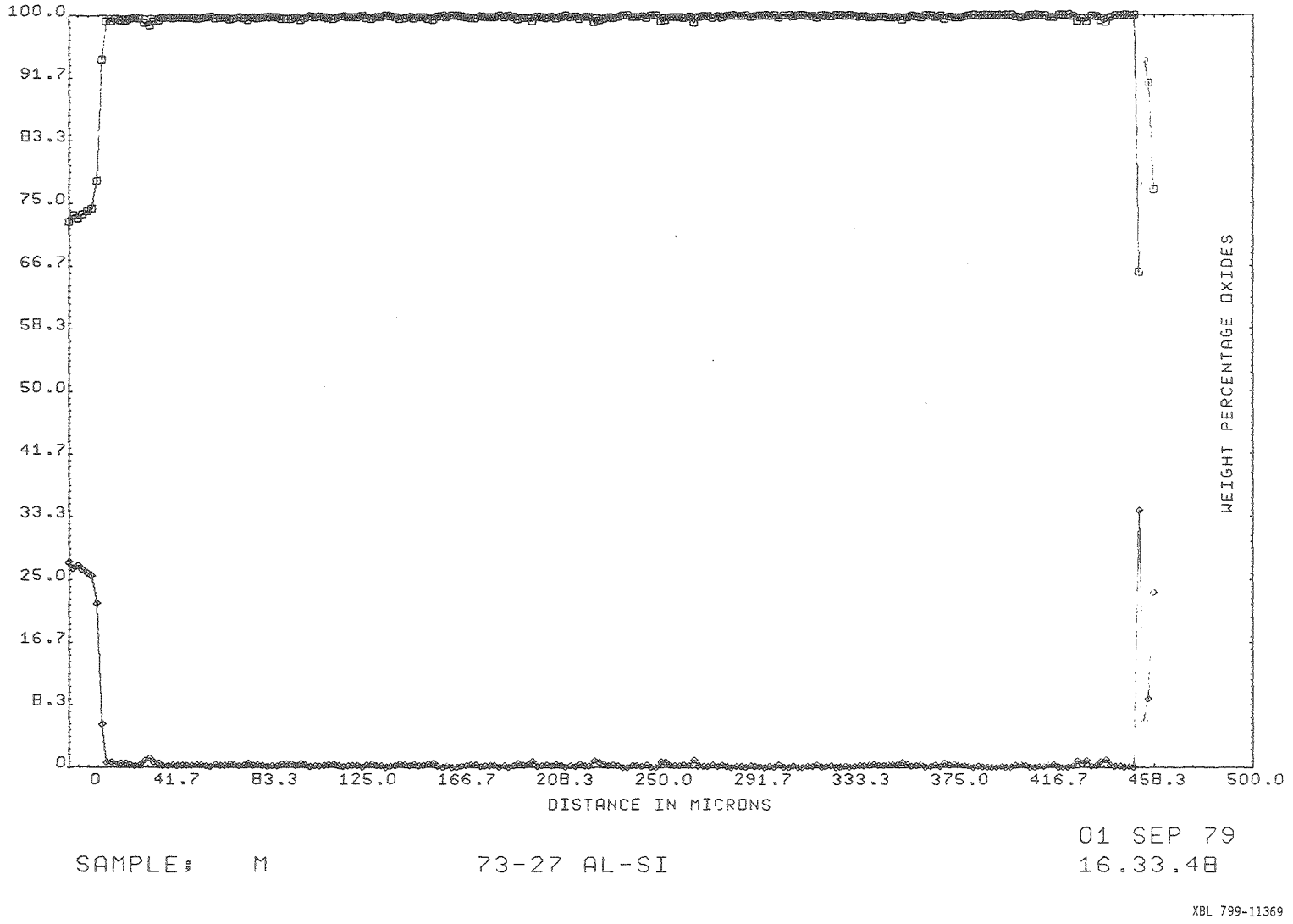
100.0
91.7
83.3
75.0
66.7
58.3
50.0
41.7
33.3
25.0
16.7
8.3
0
0
41.7
83.3
125.0
166.7
208.3
250.0
291.7
333.3
375.0
416.7
458.3
500.0
DISTANCE IN MICRONS
WEIGHT PERCENTAGE OXIDES
SAMPLE; M
73-27 AL-SI
01 SEP 79
16.33.48
XBL 799-11369

Fig. 38

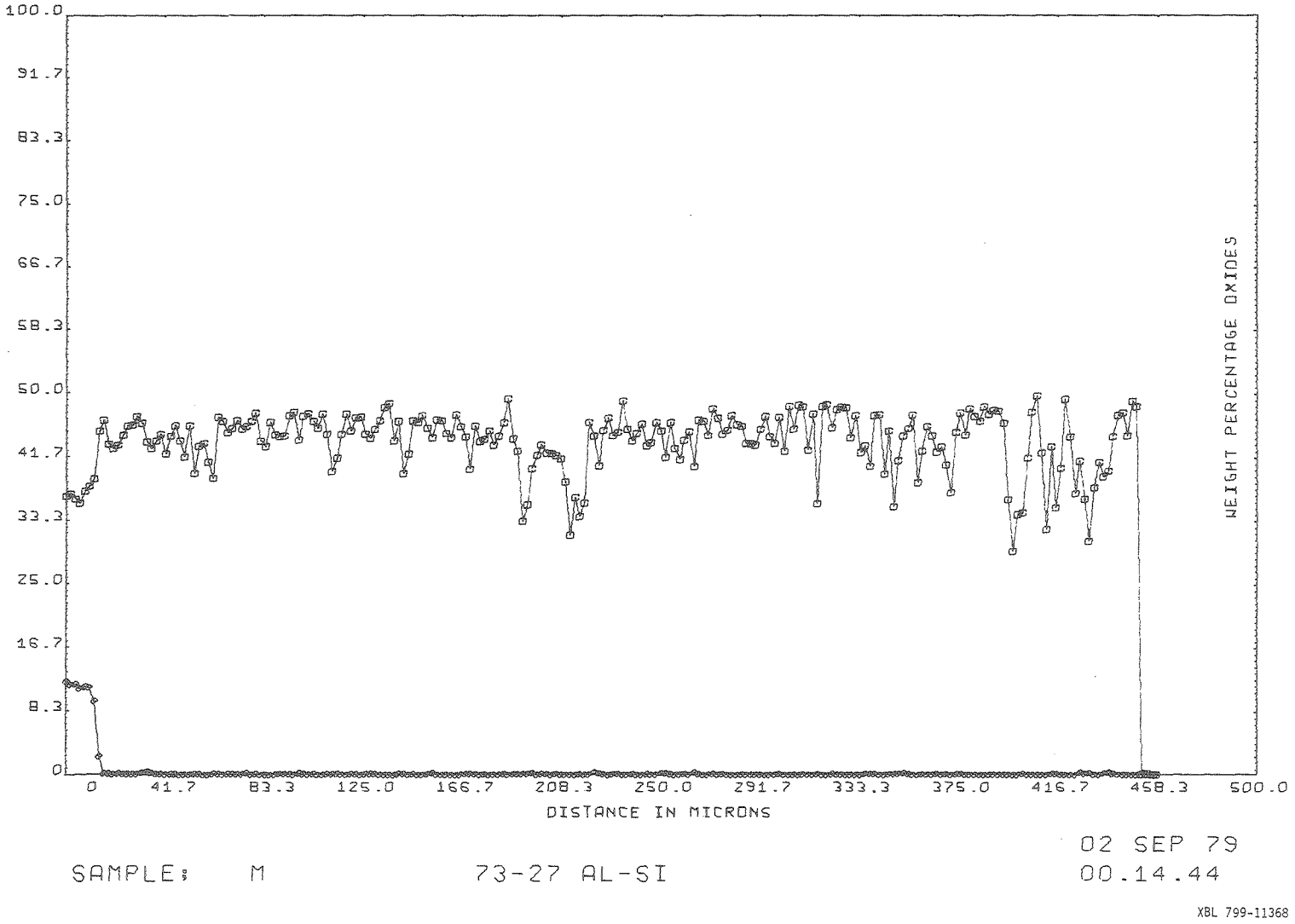
100.0
91.7
83.3
75.0
66.7
58.3
50.0
41.7
33.3
25.0
16.7
8.3
0
0
41.7
83.3
125.0
166.7
208.3
250.0
291.7
333.3
375.0
416.7
458.3
500.0
DISTANCE IN MICRONS
WEIGHT PERCENTAGE OXIDES
SAMPLE: M
73-27 AL-SI
02 SEP 79
00.14.44
XBL 799-11368

Fig. 39

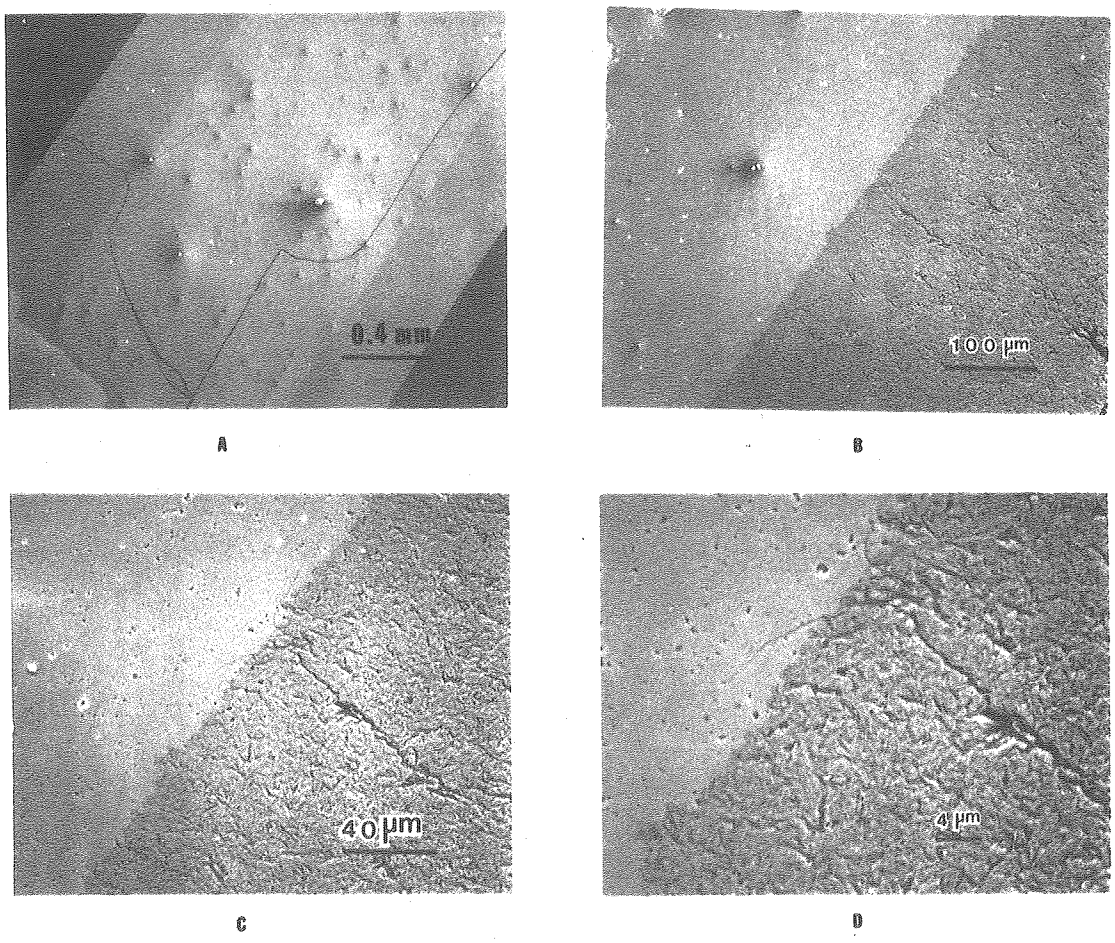

XBB797-9279

Fig. 40

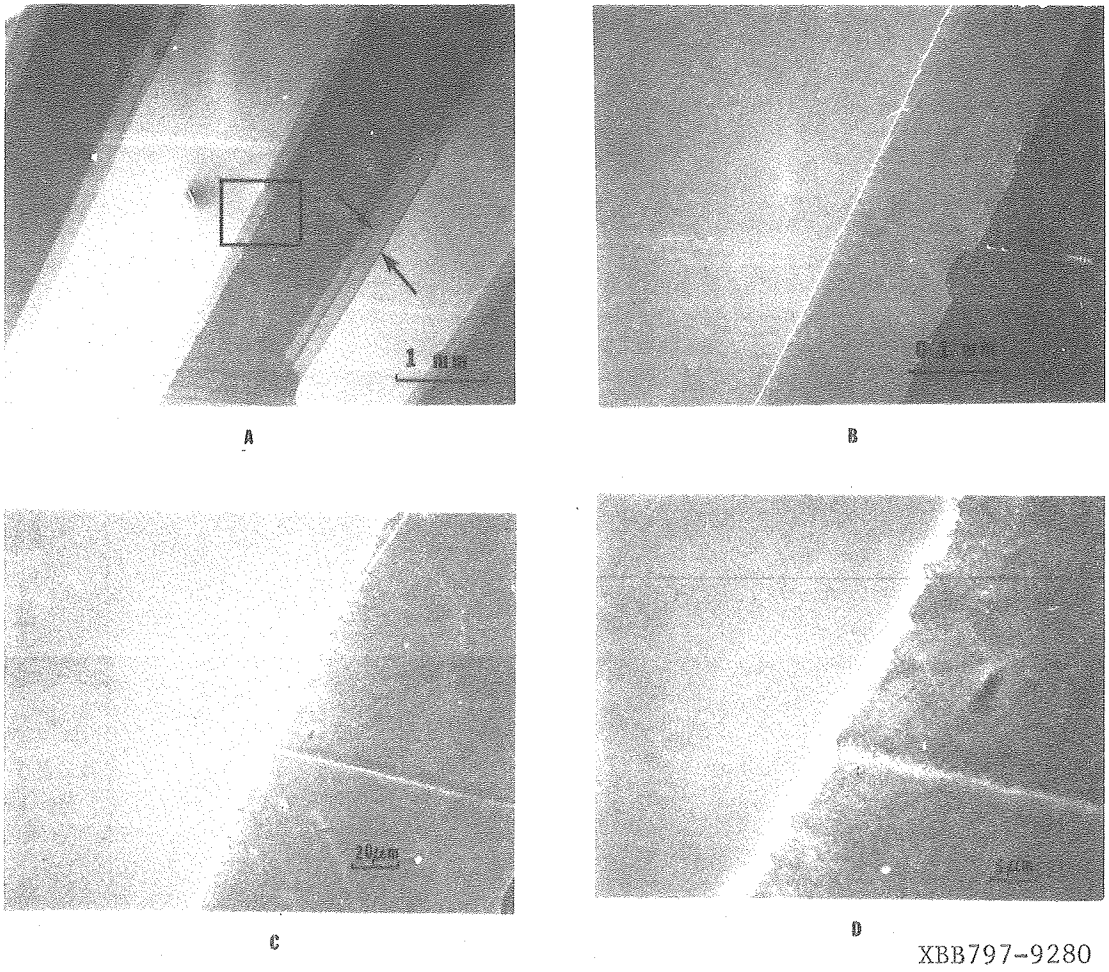

Fig. 41

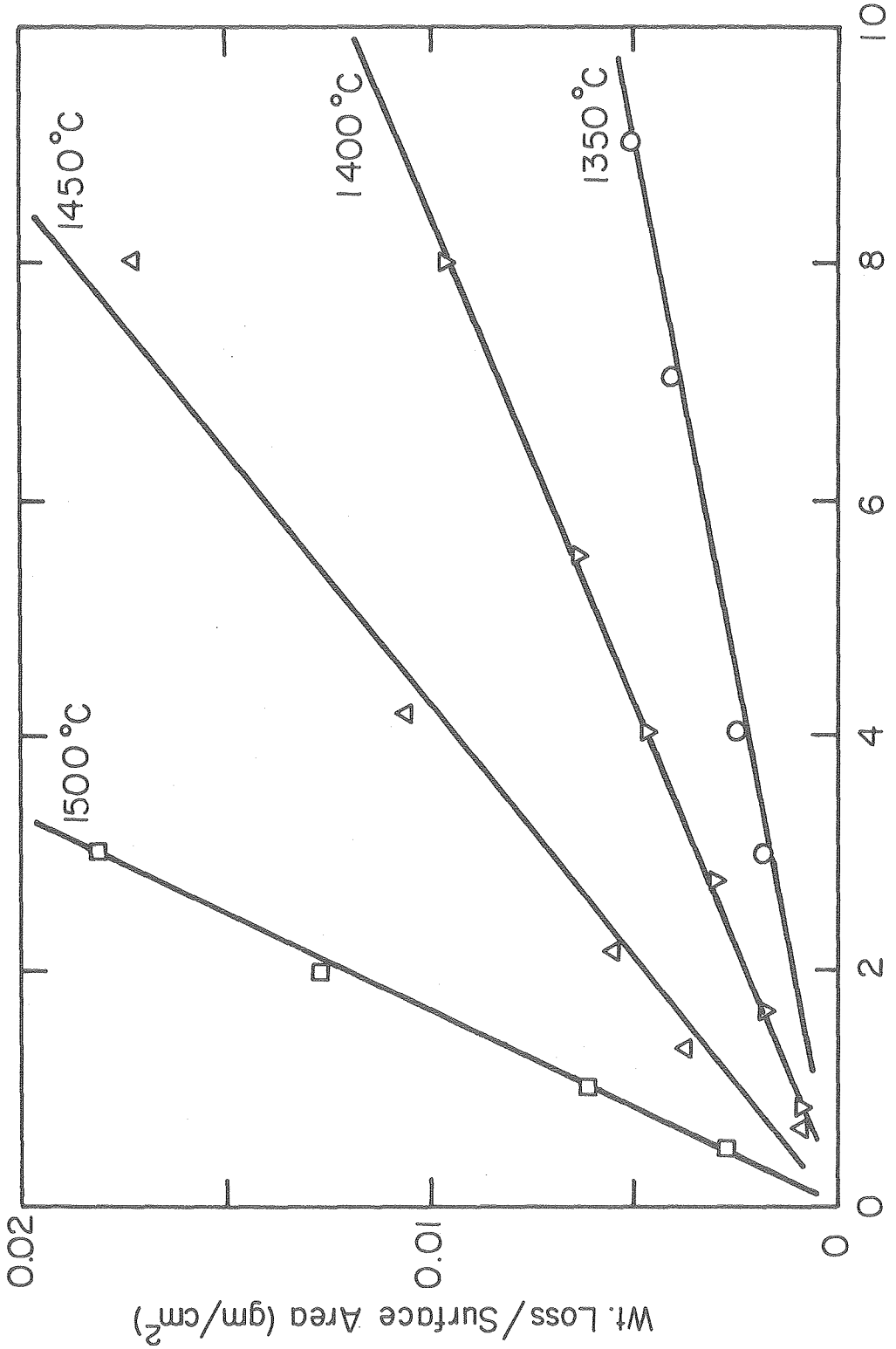

XBL797-6548

Fig. 42

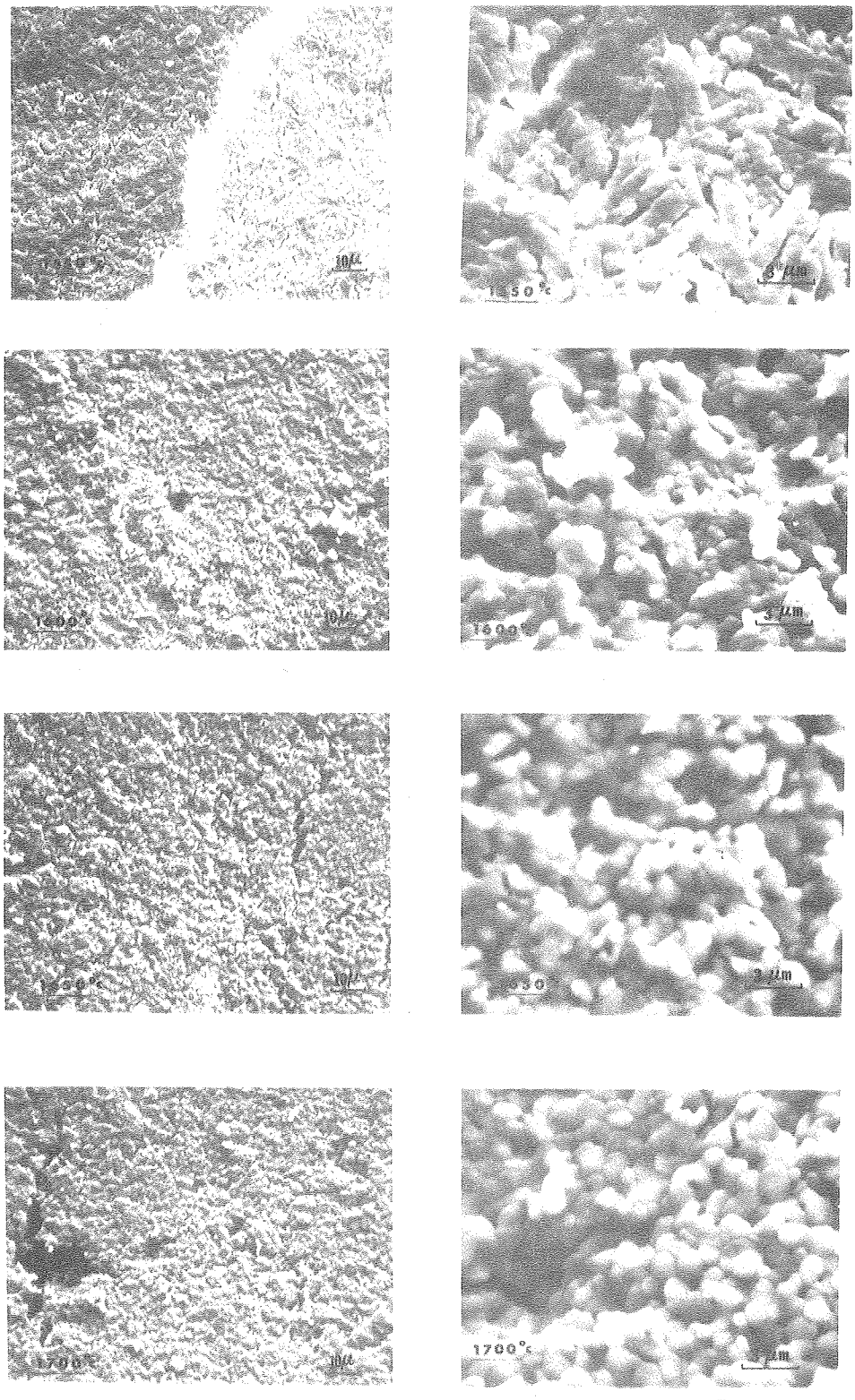

XBB797-8916

Fig. 43

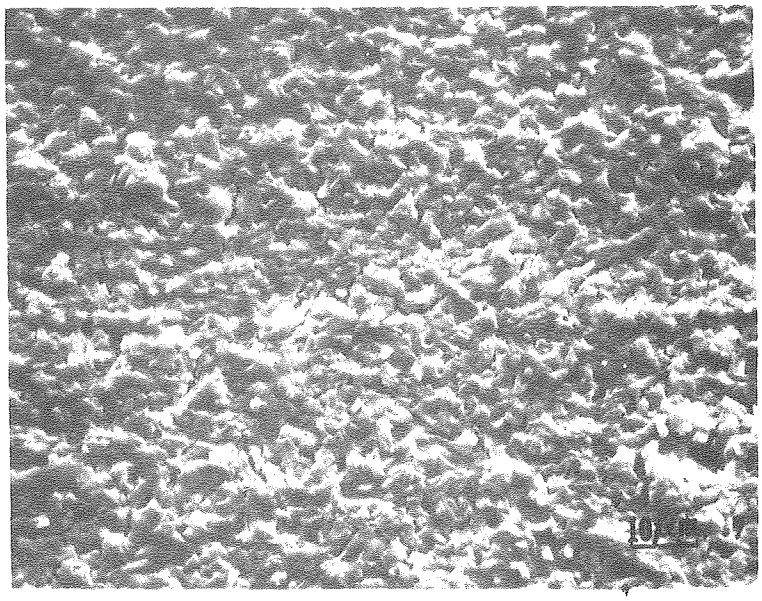

AS REACTED
1400°c

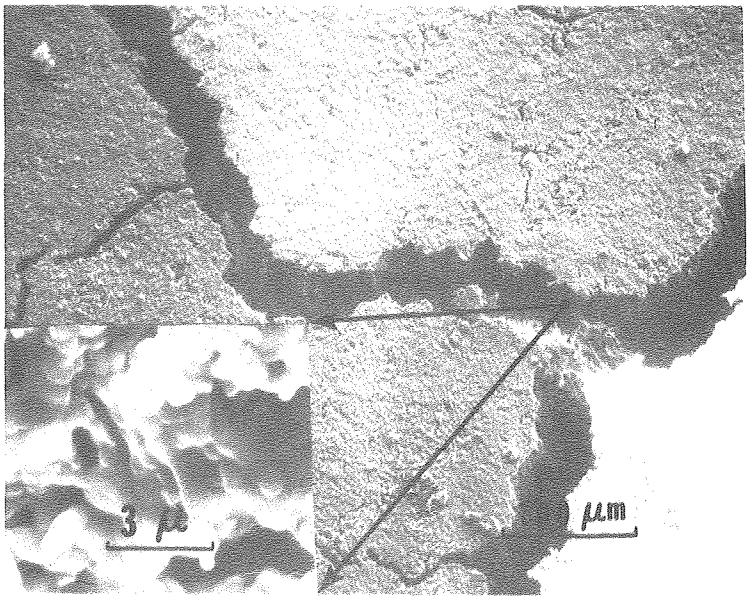

REACTED AND SINTERED
1400°c 1600°c

XBB797-8915

Fig. 44

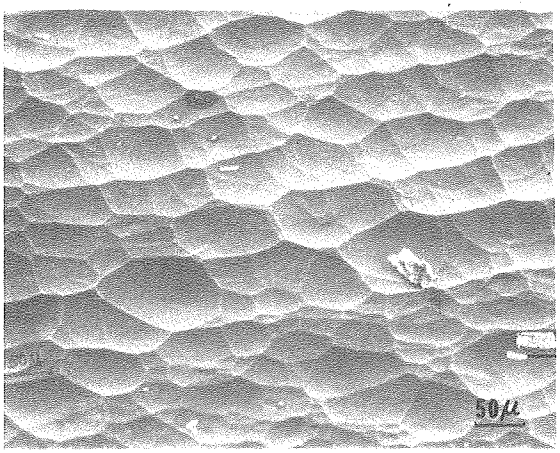

2 hr

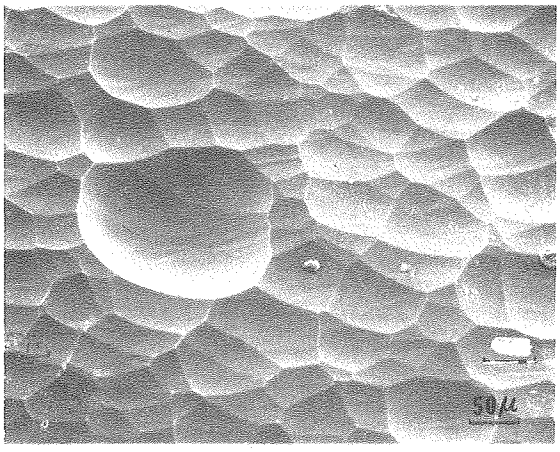

4 hr

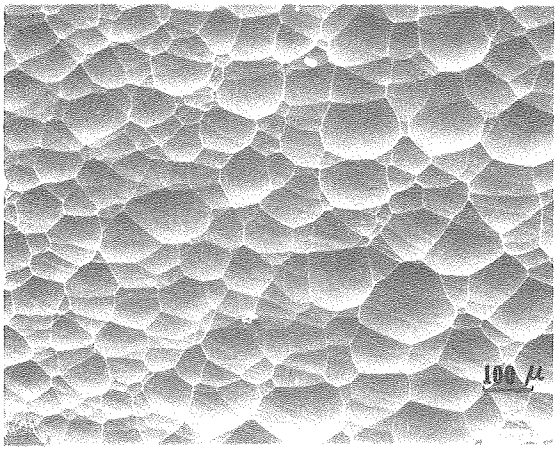

6 hr

XBB770-10487

Fig. 45

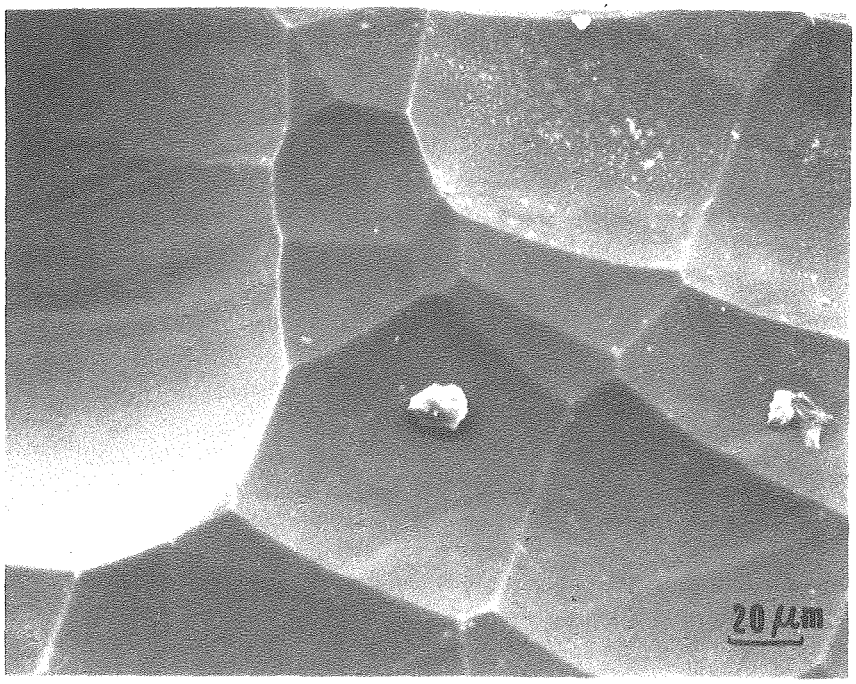

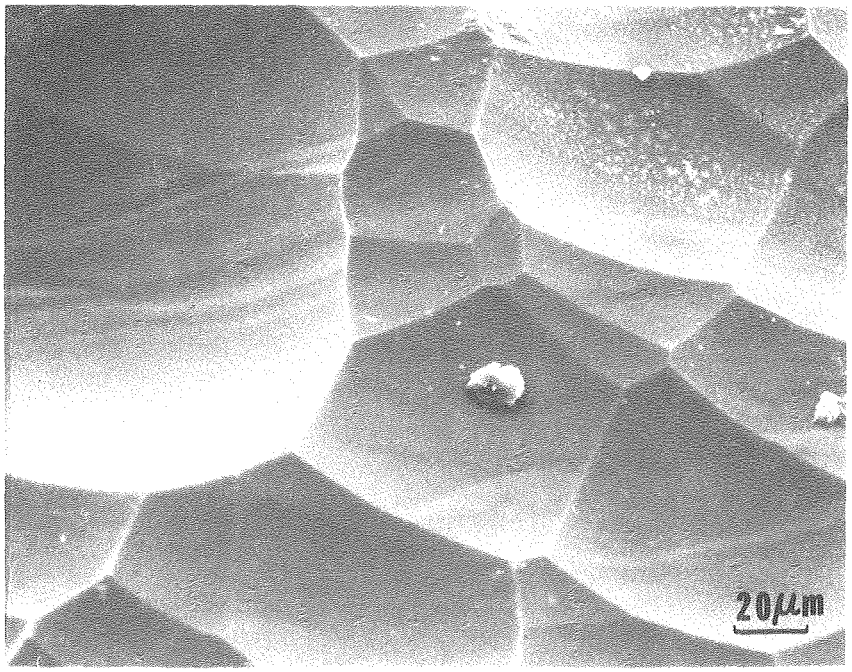

XBB780-10489

Fig. 46

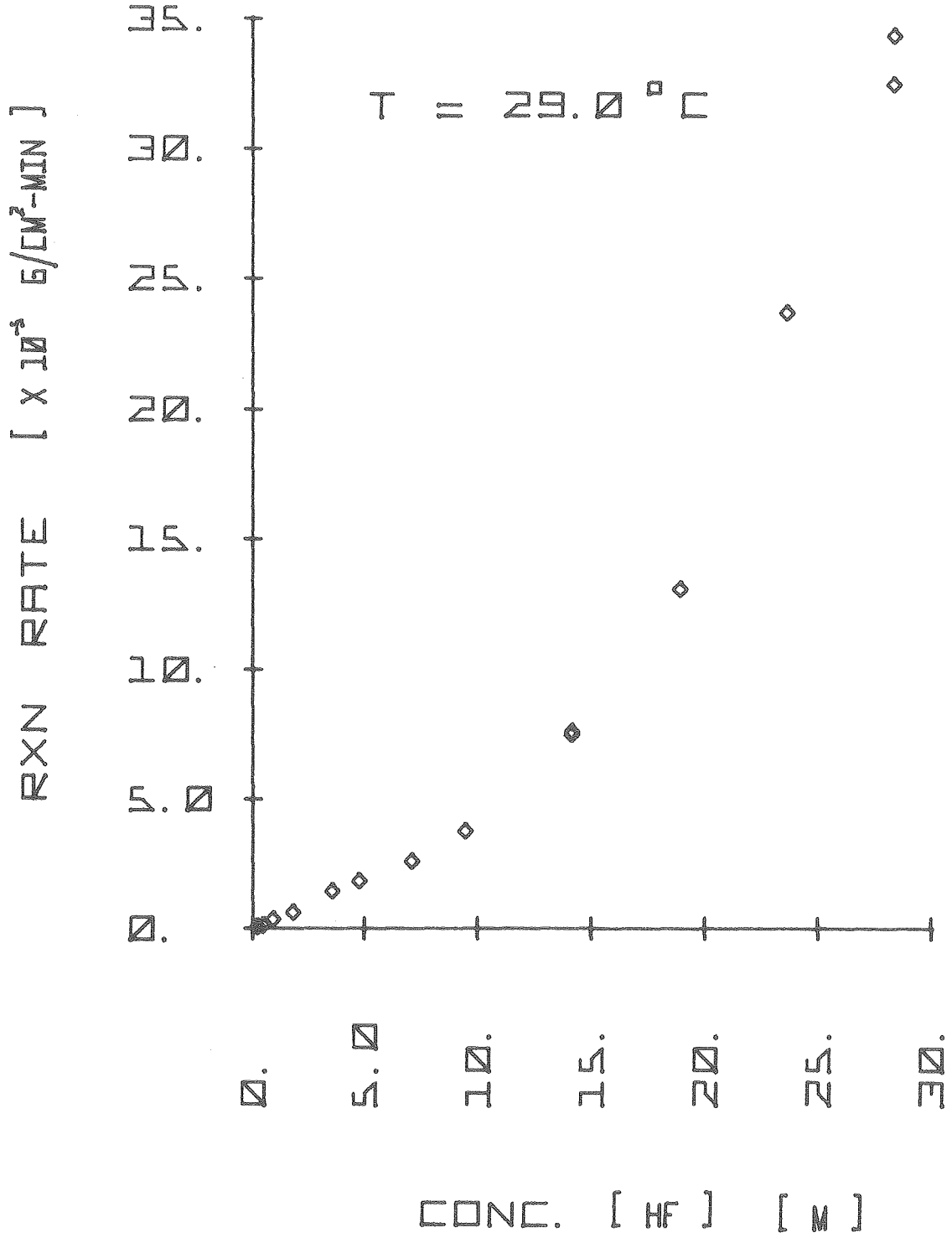
T = 29.0 °C
RXN RATE [x 10⁻³ G/CM²-MIN]
35.
30.
25.
20.
15.
10.
5.0
0.
0.
.50
1.0
1.5
2.0
2.5
3.0
CONC. [HF] [M]
XBL 7710-10329

Fig. 47

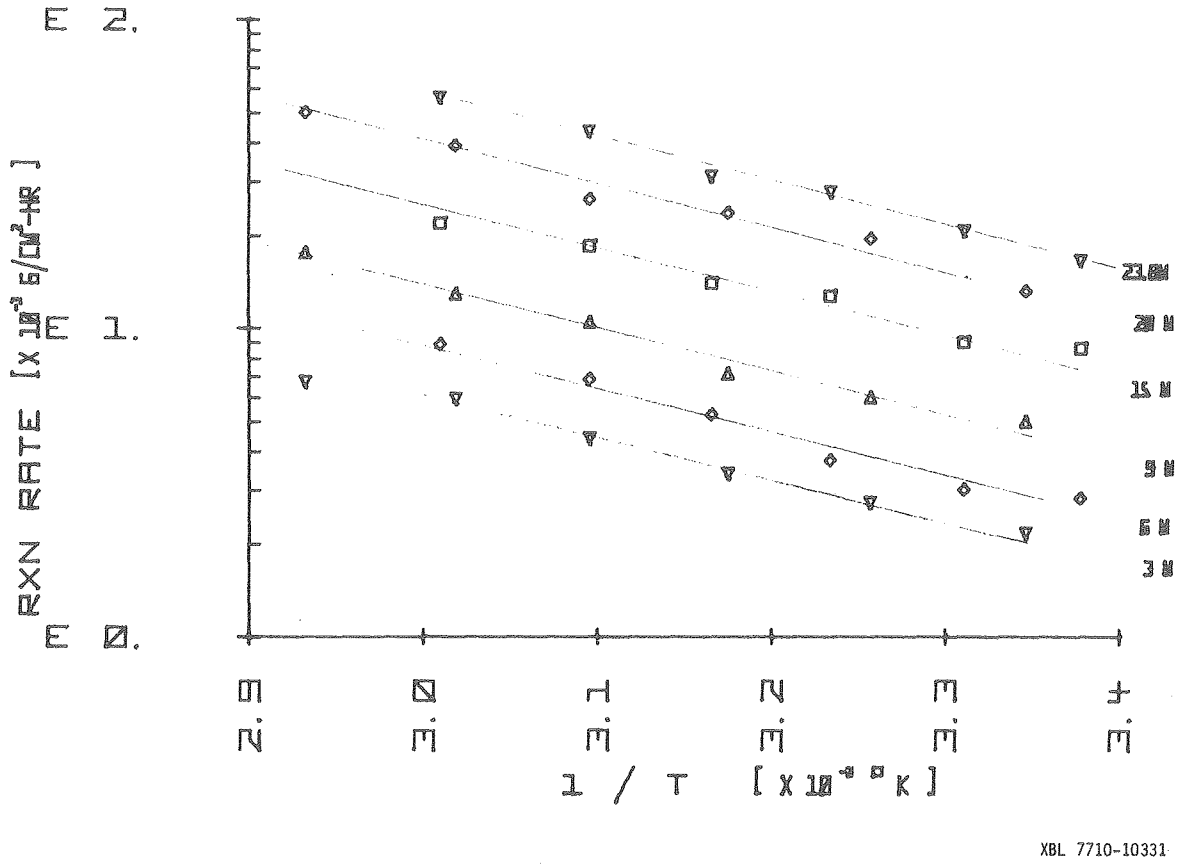

XBL 7710-10331

Fig. 48

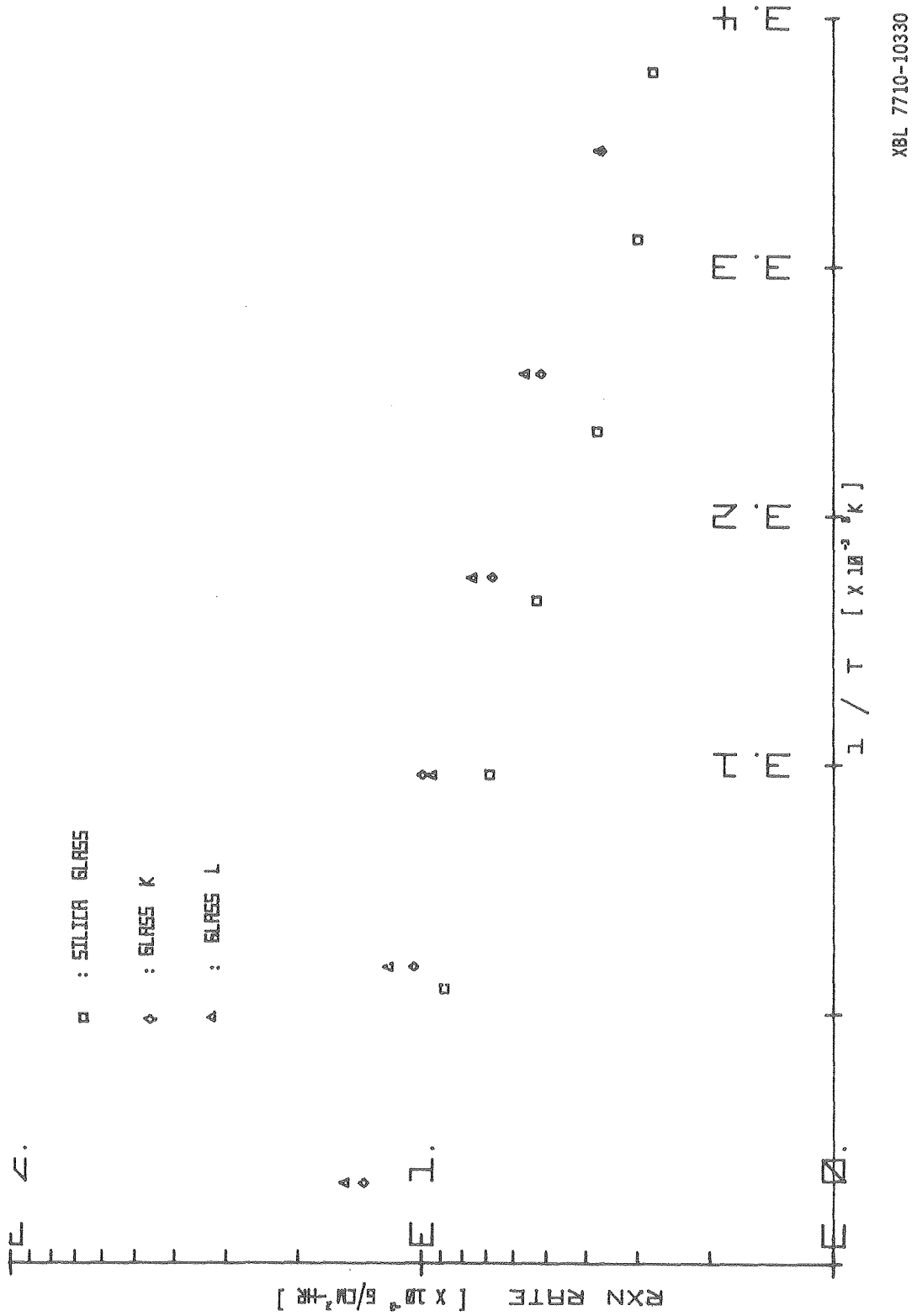
RXN RATE [x 10⁴ g/cm²-hr]
1 / T [x 10⁻³ °K]
: SILICA GLASS
: GLASS K
: GLASS L
XBL 7710-10330

Fig. 49

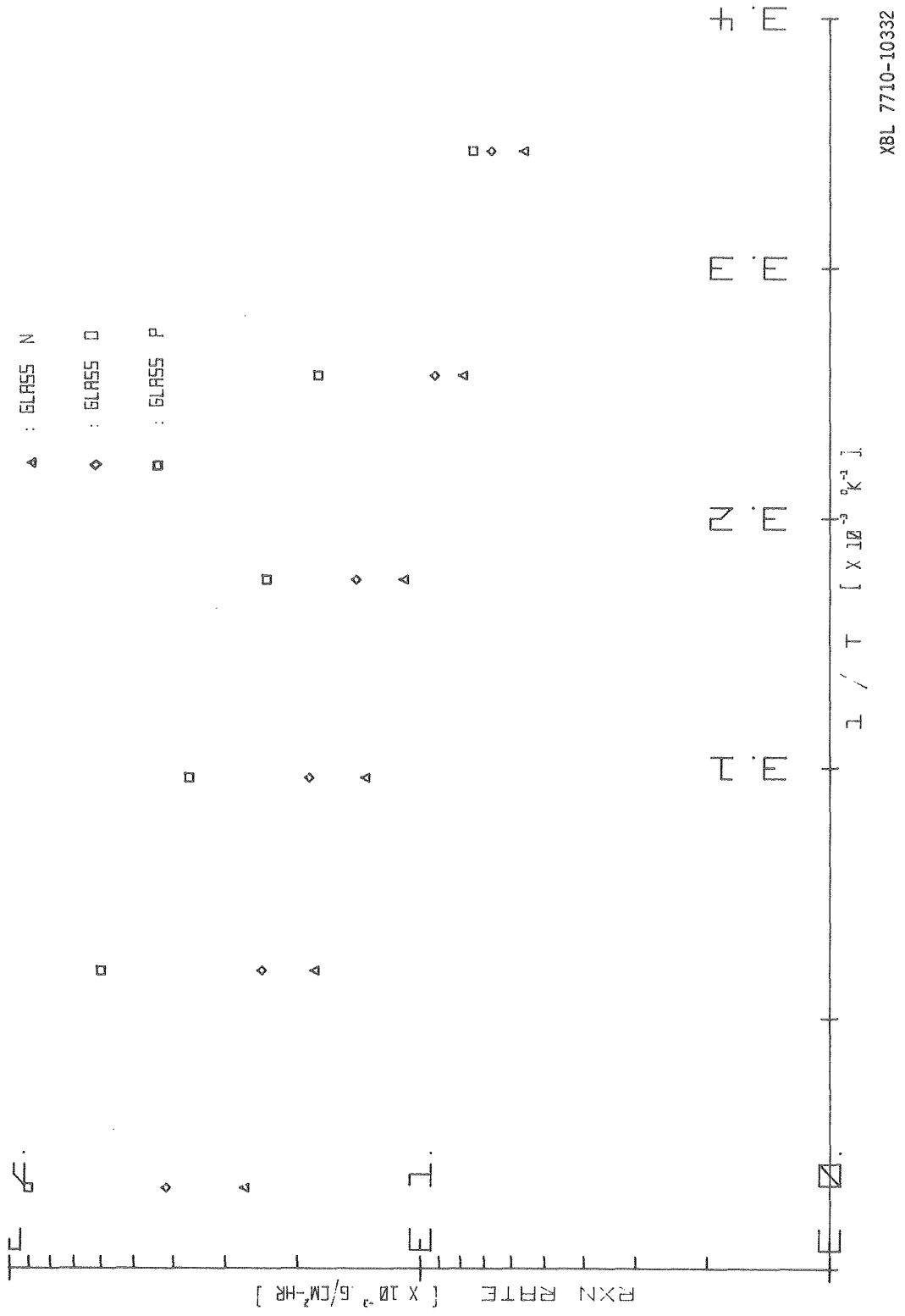
▲ : GLASS N
◇ : GLASS O
□ : GLASS P
RXN RATE [X 10⁻³ G/CM²-HR]
1 / T [X 10⁻³ °K⁻¹]
XBL 7710-10332

Fig. 50

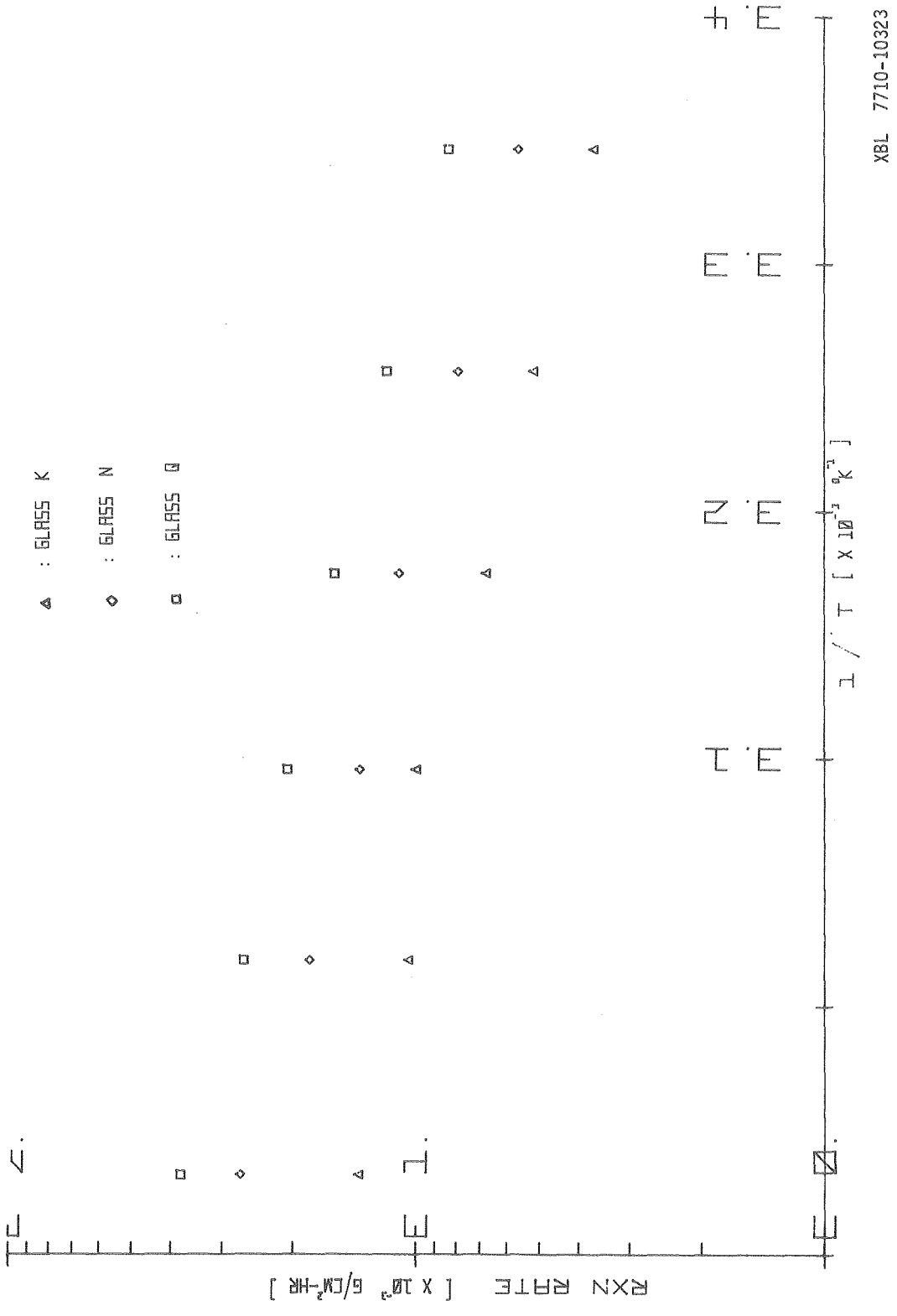
RXN RATE [X 10⁻³ G/CM²-HR]
1 / T [X 10⁻³ °K⁻¹]
▲ : GLASS K
◇ : GLASS N
□ : GLASS O
XBL 7710-10323

Fig. 51

TECHNICAL INFORMATION DEPARTMENT
LAWRENCE BERKELEY LABORATORY
UNIVERSITY OF CALIFORNIA
BERKELEY, CALIFORNIA 94720